Design of an Electrical Power System for the MARMOTSat Nanosatellite

by

Ben Kellman
BEng, University of Victoria, 2023

A Thesis Submitted in Partial Fulfillment of the
Requirements for the Degree of

MASTER OF APPLIED SCIENCE

in the Department of Electrical and Computer Engineering

We acknowledge and respect the Lək̓ʷəŋən (Songhees and Xʷsepsəm / Esquimalt) Peoples
on whose territory the university stands, and the Lək̓ʷəŋən and W̱SÁNEĆ Peoples
whose historical relationships with the land continue to this day.

Design of an Electrical Power System for the MARMOTSat Nanosatellite

by

Ben Kellman

BEng, University of Victoria, 2023

Supervisory Committee

Dr. Peter F. Driessen, Supervisor

Department of Electrical and Computer Engineering

Dr. Afzal Suleman, Supervisor

Department of Mechanical Engineering

Abstract

This thesis presents the design, implementation, and testing of the Electrical Power System (EPS) for MARMOTSat, a 3U CubeSat developed by the University of Victoria for deployment in a Sun-Synchronous Orbit (SSO) under the Canadian Space Agency's CUBICS program. MARMOTSat serves as a technology demonstrator and scientific platform, carrying the Modular CubeSat Radio (MCR), an open-source, ITAR-free software-defined radio intended for amateur radio experiments and ionospheric research. The EPS is responsible for generating, regulating, storing, and distributing power to all satellite subsystems.

A semi-centralized power architecture was developed, utilizing deployable solar arrays, lithium titanate (LTO) batteries, and maximum power point tracking (MPPT) to maximize energy generation. LTO batteries were chosen for their ability to charge at sub-zero temperatures, reducing thermal control complexity. The EPS design also incorporates subsystem level protection against radiation induced single event effects (SEE).

Extensive simulations and hardware testing validated the system's performance against power budgets and system requirements. The thesis also details the trade-offs made in power regulation and storage, as well as the design verification methodologies. MARMOTSat contributes to advancing Canadian expertise in small satellite power systems and provides a flight heritage platform for open-source space technologies, supporting broader academic and amateur radio communities.

Contents

List of Figures

List of Tables

Nomenclature

Acronyms

ADCS Attitude Determination and Control System

AM0 Air Mass 0 (typically in reference to solar irradiance in space or AM0)

BCR Battery Charge Regulator

C&DH Command and Data Handling

CCM Continuous Conduction Mode

CV Constant Voltage

DCM Discontinuous Conduction Mode

DoD Depth of Discharge

DSO Digital Storage Oscilloscope

DVB-S2 Digital Video Broadcasting - Satellite - Second Generation

EPS Electrical Power System

EXOpod CubeSat deployer system

FEP Fluorinated Ethylene Propylene

FPWM Forced Pulse Width Modulation

GNSS Global Navigation Satellite System

HF High Frequency

ITAR International Traffic in Arms Regulations

JPL Jet Propulsion Laboratory

LEO Low Earth Orbit

LEOPS Launch and Early Orbit Phase

LTAN Local Time of Ascending Node

MCR Modular CubeSat Radio

MCU Microcontroller Unit

MEMS Micro-Electro-Mechanical Systems

MLCC Multi-Layer Ceramic Capacitor

MPPT Maximum Power Point Tracking

OAP Orbit Average Power

ORCASat Optical Reference Calibration Satellite

PCDM Power Conditioning and Distribution Module

PFM Pulse Frequency Modulation

PMU Power Management Unit

PV Photovoltaic

QOD Quick Output Discharge

RBF Remove Before Flight

SEB Single Event Burnout

SEFI Single Event Functional Interrupt

SEGR Single Event Gate Rupture

SEL Single Event Latch-up

SET Single Event Transient

SEU Single Event Upset

SMPS Switched-Mode Power Supply

SoC State of Charge

SoH State of Health

SSO Sun Synchronous Orbit

STK (Ansys) Systems Tool Kit

TID Total Ionizing Dose

TT&C Telemetry, Tracking, and Control

UVic University of Victoria

VHF Very High Frequency

Symbols

β Solar beta angle

δ Declination of the real sun compared to the mean sun

η Efficiency

$\hat{h}$ The orbit normal vector

$\hat{n}$ Vector normal to a surface

$\hat{s}$ The sun vector

μ Earth's standard gravitational parameter

μ_M Sample mean

μ_P Population mean

Ω The right ascension of the ascending node

Ω_{LTAN} The local time of the ascending node in radians

Φ Eclipse angular duration

σ Standard deviation of the population

σ_M Standard deviation of the sample mean

θ	Angular position of the spacecraft in the orbital plane
ε	The difference between mean and apparent solar time in radians
A	Area
C	Electrical capacitance
D	Duty Cycle
f	Frequency
h	Orbital height
I	Electrical current
i	Orbit inclination
J	Current density
J_2	Earth's zonal harmonic coefficient
k_b	Boltzmann's constant
L	Electrical inductance
m	Diode ideality factor
N	Number of samples
N_{day}	Day of year
P	Electrical power
p_i	Probability of selecting the i^{th} value for a discrete random variable
q	Elementary charge
R	Electrical resistance
R_E	Earth's radius
T	Temperature in Kelvin

$T_{circular}$ The orbital period of a circular orbit

V Electrical voltage

x_i The i^{th} value of a discrete random variable

Acknowledgments

I would like to extend my sincere thanks to everyone who contributed their time, expertise, and support to this thesis and the broader MARMOTSat project. Their collective efforts have been instrumental in the success of this work.

The following individuals and groups deserve special mention:

- Peter Driessen
- Afzal Suleman
- Alexander Doknjas
- Levente Buzas
- Tristan Tarnowski
- Maarteen Meerman
- Evan Peters

1 Introduction

Small satellites, particularly CubeSats, have revolutionized access to space by providing a low-cost, rapid development platform for scientific research, technology demonstration, and educational missions. This thesis presents the design, analysis, and implementation of the Electrical Power System (EPS) for MARMOTSat, a 3U CubeSat developed at the University of Victoria under the Canadian Space Agency's CUBICS program. MARMOTSat carries the Modular CubeSat Radio (MCR), an open-source, ITAR-free software-defined radio payload that enables both amateur radio and scientific experiments. The mission builds on design heritage from ORCASat, the University of Victoria's previous CubeSat, while introducing deployable solar arrays and a higher power EPS to support the increased power demands of the MCR. The EPS is designed to provide power generation, energy storage, and regulated power distribution while adhering to the strict size constraints of the CubeSat form factor. This thesis outlines the analysis used to appropriately size the energy generation and storage elements of the EPS, followed by the detailed electrical design of the main EPS Power Conditioning and Distribution Module (PCDM), which is responsible for harvesting energy from the solar array, charging the batteries, and distributing regulated power to all MARMOTSat subsystems.

1.1 Nanosatellites and CubeSats

Nanosatellites, defined as satellites with masses between 1 and 10 kilograms, have become an increasingly important class of spacecraft for scientific research, technology demonstration, and educational missions in low Earth orbit (LEO) [1]. They offer affordable access to space for universities, small companies, and emerging space nations, enabling targeted missions that can address scientific questions, provide Earth observation data, or test new technologies in the space environment. Among nanosatellites, the CubeSat standard has been particularly impactful in lowering the barriers to space access. Initially proposed by California Polytechnic State University and Stanford University in 1999, the CubeSat standard defines spacecraft in units of 10cm $\times$ 10cm $\times$ 10cm ("1U"), which provides a standard form factor used by many commercial deployers; simplifying integration with launch vehicles [2]. Despite their advantages, CubeSats face significant challenges due mainly to their

limited volume and mass budgets, which require compact subsystem design. Thermal management, radiation tolerance, and power generation remain non-trivial challenges [1], due to the size and cost constraints of these missions.

1.2 ORCASat

ORCASat was a 2U CubeSat developed by the University of Victoria under the Canadian CubeSat Project; it operated in an ISS orbit from December 2022 to July 2023, with the objective of providing an optical calibration source in orbit for ground-based telescopes [3]. All subsystems, with the exception of the GNSS receiver and ADCS, were fully developed by students and researchers at UVic, providing the team with experience in spacecraft systems engineering, subsystem design, payload integration, and spacecraft operations. The lessons learned and experience gained from ORCASat have directly informed the development of MARMOTSat, with MARMOTSat reusing many of the subsystems developed for ORCASat.

1.3 MARMOTSat

MARMOTSat is a 3U CubeSat currently being developed by the University of Victoria as part of the Canadian Space Agency's CUBICS program, aimed at providing hands-on training in spacecraft systems engineering and demonstrating the capabilities of the open-source Modular CubeSat Radio (MCR). The MCR, also developed by the UVic team, is an ITAR-free software-defined radio intended for amateur radio and scientific experimentation on CubeSat platforms. MARMOTSat will host multiple MCR-based payloads, including a VHF digipeater, VHF and HF Morse code beacons, an HF DVB-S2 video beacon, and an HF linear frequency-modulated beacon designed for transionospheric sounding. Scheduled to launch aboard SpaceX's Transporter-17 rideshare mission using an EXOpod Nova deployer, MARMOTSat aims to establish flight heritage for the MCR and key spacecraft subsystems. The mission will help advance accessible small-satellite technologies and further build Canadian expertise in CubeSat mission design, integration, and operations.

1.3.1 Spacecraft Architecture

Figure 1.1 illustrates the internal layout of MARMOTSat, clearly identifying each subsystem. The spacecraft's external features are shown in Figure 1.2, while Figure 1.3 presents

the placement of internal electronics within the fully assembled spacecraft, along with the defined MARMOTSat coordinate system.

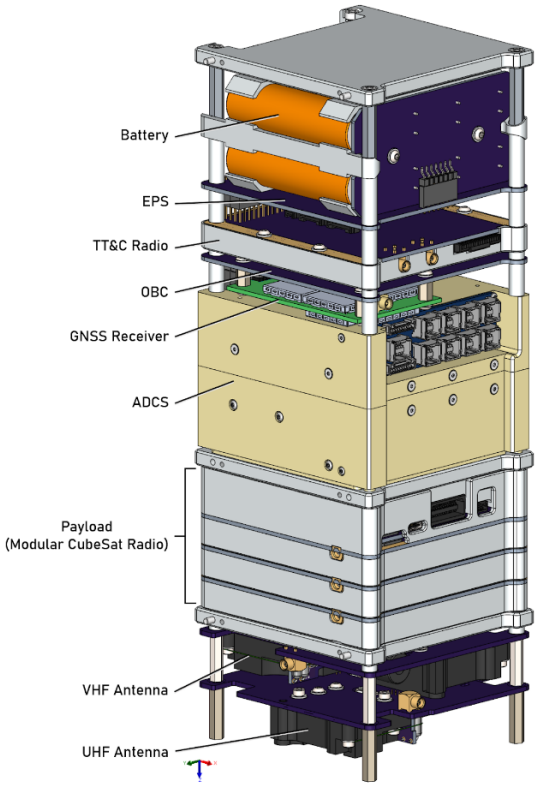

Figure 1.1: MARMOTSat Internal Electronics (Illustration by Tristan Tarnowski)

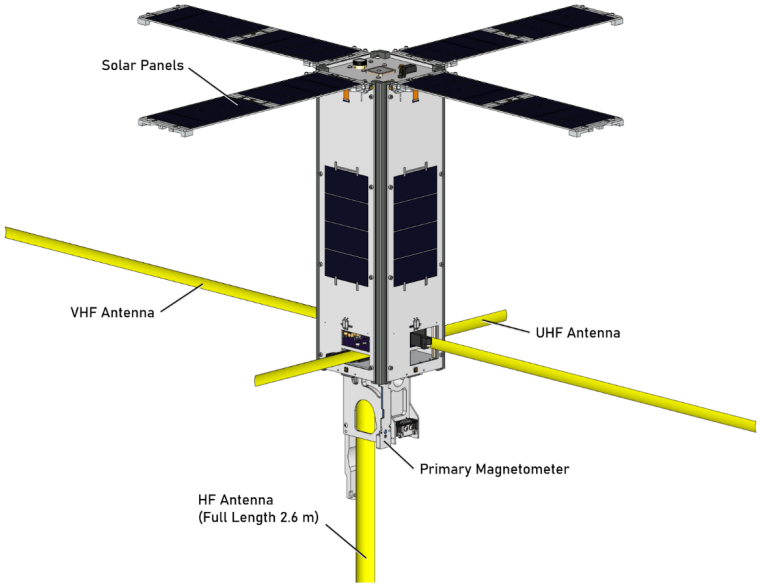

Figure 1.2: MARMOTSat External Features (Illustration by Tristan Tarnowski)

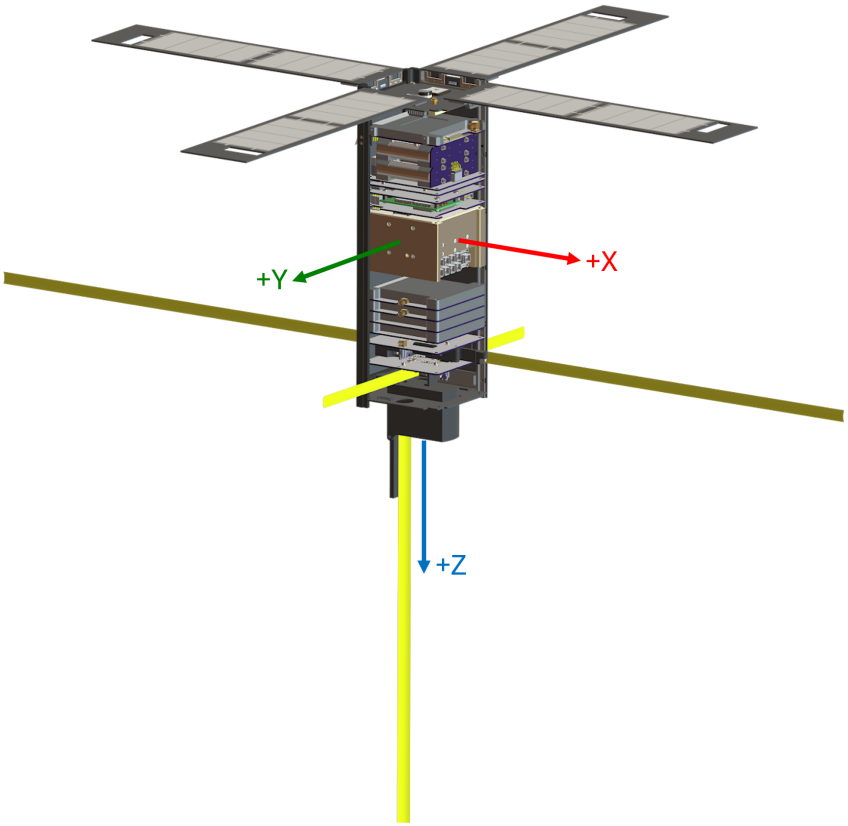

Figure 1.3: MARMOTSat Coordinate System(Illustration by Tristan Tarnowski)

Payload The MARMOTSat payload is the Modular CubeSat Radio (MCR), an open-source, ITAR-free software-defined radio (SDR) developed by the University of Victoria with funding from Amateur Radio Digital Communications (ARDC). Designed as a flexible, reconfigurable radio platform for space applications. It integrates a high-performance FPGA MPSoC for onboard processing and an AD9865 mixed-signal front-end for RF digital conversion. The modular architecture accommodates specialized front-end modules tailored to specific frequencies and mission requirements; MARMOTSat specifically carries an HF power amplifier module and a VHF transverter module. A camera is included in the payload stack to support the DVB-S2 video beacon. This modularity not only addresses the current mission's objectives but also establishes a foundation for future advancements in amateur satellite communication technology.

On-Board Computer The On-Board Computer (OBC) is responsible for controlling core spacecraft functions, including command routing, telemetry collection, and subsystem control. The OBC is built around the Texas Instruments TMS570 safety microcontroller, which offers fault tolerance capabilities, such as ECC RAM and a lock-step Cortex-R4F CPU. It interfaces with other spacecraft subsystems primarily via CAN and UART communication links. The OBC integrates a NovAtel OEM719 GNSS receiver for orbit determination and timing, enabling precise position and velocity measurement along with time synchronization. The OBC design builds on the heritage of the ORCASat mission, leveraging flight-proven design with minor adaptations to meet the specific mission requirements of MARMOTSat.

Telemetry, Tracking, and Command The Telemetry, Tracking, and Command (TT&C) subsystem provides the primary communications link between MARMOTSat and ground operators, enabling command uplink and telemetry downlink. The subsystem is based on the Texas Instruments CC1110 system-on-chip (SoC), integrating a low power microcontroller and an RF transceiver. Building upon the design heritage of the ORCASat TT&C subsystem, it operates within the UHF amateur radio band and supports half-duplex communication. Communication with the ground station is facilitated by a deployable tape-spring antenna that extends after spacecraft deployment. Routine telemetry monitoring and command uplinks are conducted via the University of Victoria's ground station. The

TT&C subsystem operates using an entirely separate RF band, antenna, and RF path from the MCR payload, ensuring a dedicated and reliable communications channel for critical spacecraft operations and health monitoring.

Attitude Determination and Control MARMOTSat employs CubeSpace's Gen 2 system for three-axis stabilization, utilizing reaction wheels and magnetorquers for attitude control and Sun sensors, magnetometers, and MEMS rate sensors for attitude determination. Reaction wheels maintain spacecraft orientation by exchanging angular momentum with the satellite body. However, their momentum storage capacity is limited by their maximum spin speed, requiring magnetorquers to periodically remove accumulated angular momentum by interacting with Earth's magnetic field. This prevents reaction wheel saturation by transferring the spacecraft's angular momentum to Earth.

The ADCS supports multiple pointing modes that will be used during different phases of the mission. Immediately after deployment, the spacecraft enters a passive tumbling state with no attitude control and subsequently transitions into either a Y-Thompson spin using magnetorquers. The Y-Thompson spin provides robust, low power stabilization by aligning the spacecraft Y axis with the orbit normal direction and slowly rotating the spacecraft around the Y axis, this simplifies transitions to other pointing modes. For optimal solar power generation, the spacecraft can enter a Sun-pointing mode, orienting its deployable solar array toward the Sun. During routine operations, nadir-pointing modes align either the +Z or +X axis toward Earth. The +Z nadir-pointing mode optimizes the communications link, while the +X nadir-pointing mode minimizes atmospheric drag caused by the large HF antenna, which is particularly beneficial when at lower altitudes. This allows MARMOTSat to balance power generation, communication requirements, and payload operations throughout its mission.

Structure The spacecraft structure consists of an aluminum frame with rails compatible with the EXOpod deployment system and contains the deployable solar panels and antennas. The deployables use proven designs from ORCASat, featuring burn-wire mechanisms for release and mechanical switches for deployment detection. The structure also facilitates thermal management through conduction paths and thermal coatings, helping to maintain stable thermal conditions during operations.

Electrical Power System The Electrical Power System (EPS) generates, stores, and distributes electrical power to all MARMOTSat subsystems. It includes body-mounted and deployable solar panels for energy generation, a battery pack for energy storage, and dedicated electronics for power regulation and distribution. While the EPS design leverages heritage from the ORCASat mission, significant enhancements have been made to meet the increased power demands of the MCR payload. Like ORCASat, the MARMOTSat EPS uses lithium titanate batteries, enabling battery charging at sub-zero temperatures without active thermal control. Subsequent chapters in this thesis present the analysis, design, and testing undertaken for the EPS, including power generation modeling, battery sizing, and the development of the Power Conditioning and Distribution Module (PCDM).

1.4 Risk Management

The design philosophy of the EPS is heavily influenced by the inherent trade-off between mission cost and risk, a common consideration in academic CubeSat programs. To adhere to budgetary constraints, the design relies extensively on Commercial-Off-The-Shelf (COTS) components, which offer a significant cost advantage over their space-qualified counterparts, often being over one hundred times cheaper. This approach introduces a level of risk, as COTS parts are typically not characterized or hardened for the space radiation environment, leading to an increased probability of premature component failure due to effects such as Total Ionizing Dose (TID) or Single Event Effects (SEEs). A similar trade-off is made in the decision to develop an in-house EPS rather than purchase a commercial alternative. While this introduces risk associated with flying a new design, it provides more training opportunities and dramatically lowers the per-unit cost. This approach enables the production of multiple EPS units, facilitating more extensive system-level testing and providing more students with hands-on hardware experience. This risk management strategy, prioritizing affordability and student training while accepting a lower level of reliability, is fundamental to the overall EPS design and is critical for enabling missions like MARMOTSat within the financial scope of a university project.

2 Background

The Electrical Power System (EPS) of a spacecraft is responsible for ensuring a continuous supply of power to all subsystems. To achieve this, the EPS must regulate the power from the solar array, store energy to provide power during the eclipse, and distribute generated and stored power to other subsystems [4]. A high-level block diagram of these EPS functions is shown in Figure 2.1. All commercial EPS modules surveyed employ a switching regulator to charge a lithium-ion battery from the solar array, and typically offer distribution of common regulated voltages (e.g. 3.3V or 5V) or unregulated battery voltage to the spacecraft subsystems [2], [5]–[7]. These systems generally support multiple solar array inputs with maximum power point tracking (MPPT), enabling efficient operation across variations in illumination, thermal conditions, or solar array configuration between spacecraft faces. Figure 2.2 presents a block diagram of a typical COTS EPS.

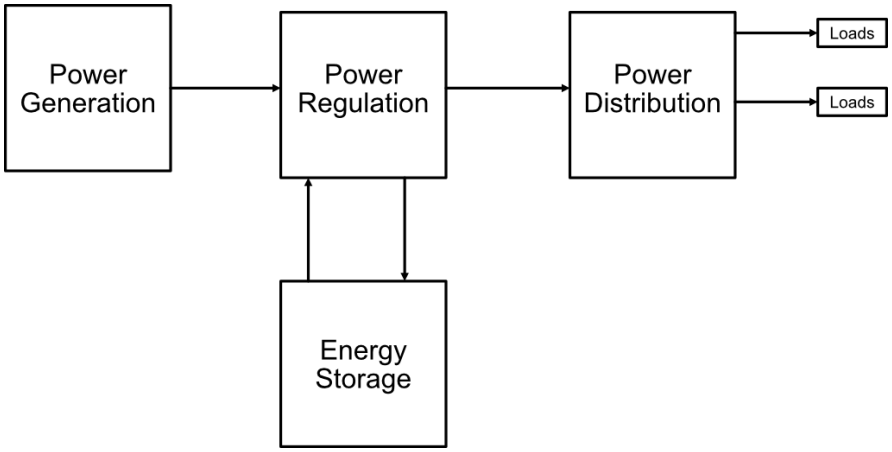

Figure 2.1: Basic EPS Functions

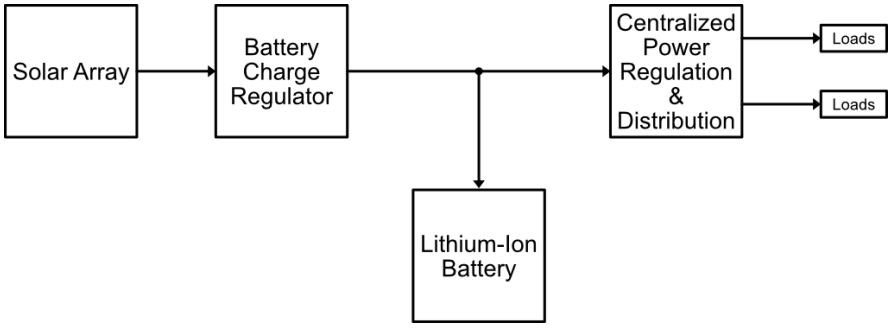

Figure 2.2: Typical COTS EPS Block Diagram

The remainder of this chapter establishes the foundational knowledge required to understand the components of an EPS, and more specifically the design and analysis of the MARMOTSat EPS. It begins with an overview of orbital mechanics relevant to spacecraft power generation and then discusses photovoltaic (PV) cell characteristics, battery technologies, and power conversion methods. The chapter concludes by examining the space radiation environment and its effects on electronics, key factors influencing EPS design choices for long-duration missions.

2.1 Orbits

A basic understanding of orbital mechanics is essential for analyzing spacecraft power generation. MARMOTSat will be launched into a Sun-synchronous orbit (SSO) as part of a SpaceX Transporter mission, so this section focuses exclusively on SSOs. An SSO is a high-inclination, nearly circular orbit that's orbital plane roughly maintains its orientation with respect to the Sun over the course of the year [8]. This allows for both consistent power generation and lighting conditions on the ground below the spacecraft, making these orbits highly desirable, particularly for earth imaging spacecraft [8]. The full implications of this orbital configuration are explored in more depth for the remainder of this section.

A spacecraft in a circular orbit maintains a constant altitude and angular velocity. The period of such an orbit around Earth is given by Equation 1, adapted from [9], where μ is Earth's standard gravitational parameter, R_E is Earth's radius, and h is the spacecraft's altitude above Earth's surface. The relevant physical constants for these calculations are listed in Appendix A. Lastly, since the angular velocity remains constant in a circular orbit, the angular position of the spacecraft as a function of time can be expressed by Equation 2.

$$T_{\text{circular}} = \frac{2\pi}{\sqrt{\mu}}(h + R_E)^{\frac{3}{2}} \tag{1}$$

$$\theta = \frac{2\pi}{T_{\text{circular}}}t \tag{2}$$

The inclination of an orbit is the angle between the orbital plane and Earth's equator, as illustrated in Figure 2.3. Together with the orbital altitude, inclination determines the rate

at which the orbit precesses around Earth's axis of rotation. This precession is caused by Earth's equatorial bulge, known as the J2 perturbation [8]. The precession rate, $\dot{\Omega}$, for a circular orbit is given by Equation 3 from [8], where i is the orbit's inclination, h is the orbital altitude, and J_2 is Earth's zonal harmonic coefficient (listed in Appendix A). If the precession rate matches $\frac{365^\circ}{1\text{year}}$, the orbit becomes Sun-synchronous, maintaining an approximately constant orientation relative to the Sun throughout the year, as shown in Figure 2.5. Plotting inclination against altitude for circular orbits satisfying this condition yields Figure 2.4, which shows that circular Sun-synchronous orbits are nearly polar, with inclinations close to 90°.

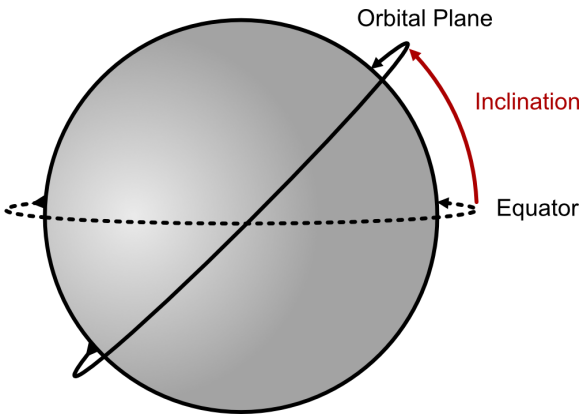

Figure 2.3: Orbit Inclination

$$\dot{\Omega} = -\left[\frac{3}{2}\frac{\sqrt{\mu}J_2R_E^2}{(R_E+h)^{\frac{7}{2}}}\right]\cos i \tag{3}$$

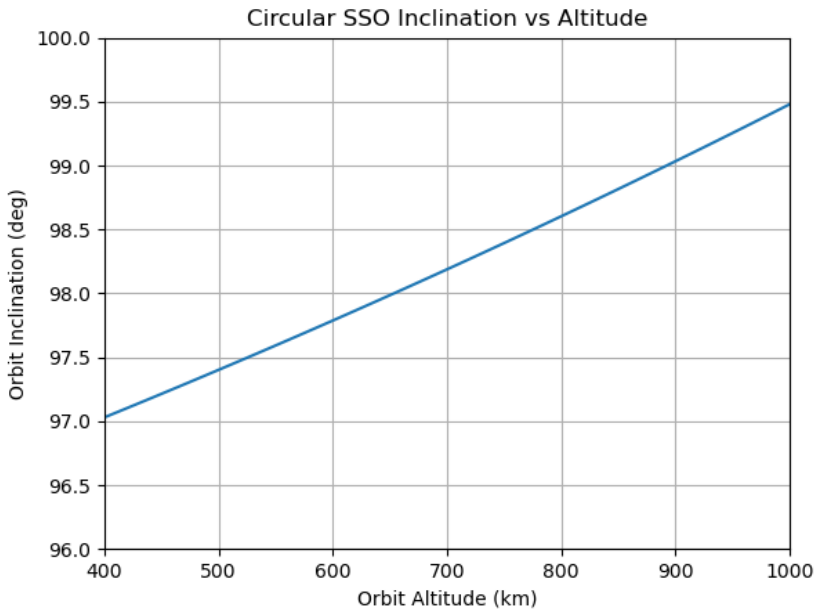

Figure 2.4: Sun-Synchronous Condition for Circular Orbits

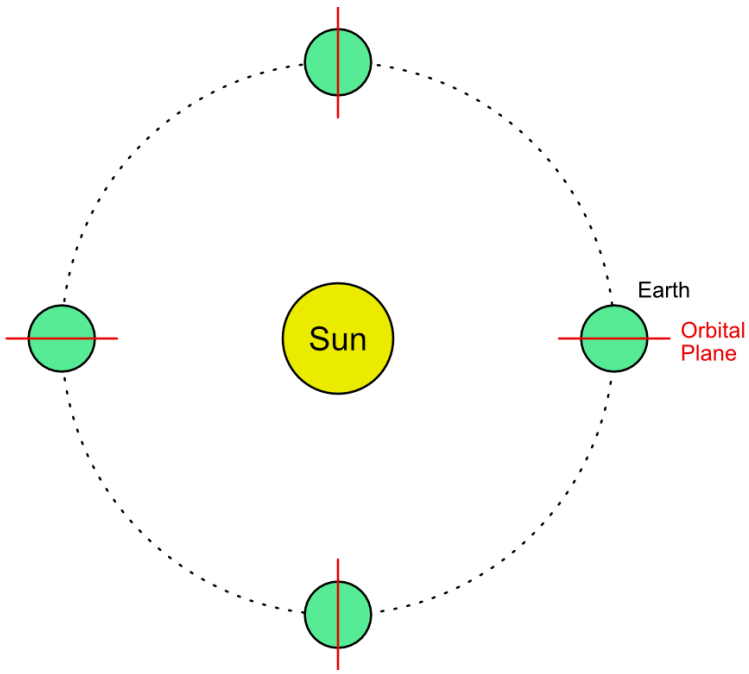

Figure 2.5: A Sun Synchronous Orbit

The solar beta angle, or simply the beta angle, is the angle between a vector pointing from Earth's center to the Sun and the spacecraft's orbital plane. This angle determines both the duration of orbital eclipses and the Sun's position relative to a nadir-pointing spacecraft, making it a critical factor in spacecraft power generation. If we make the simplifying assumption that Earth's orbit around the Sun is circular and that Earth's rotational axis is orthogonal to its orbital plane, the beta angle for a spacecraft in SSO remains constant throughout the year. This relationship is illustrated in Figure 2.6, where the "Mean Sun" is a conceptual point that occupies the Sun's position under these ideal conditions. The angle between the orbital plane and the "Mean Sun" vector defines the Mean Local Time of Ascending Node (MLT or LTAN), which is typically expressed in hours rather than degrees. The LTAN also represents the local solar time when the spacecraft crosses the equator heading north [8].

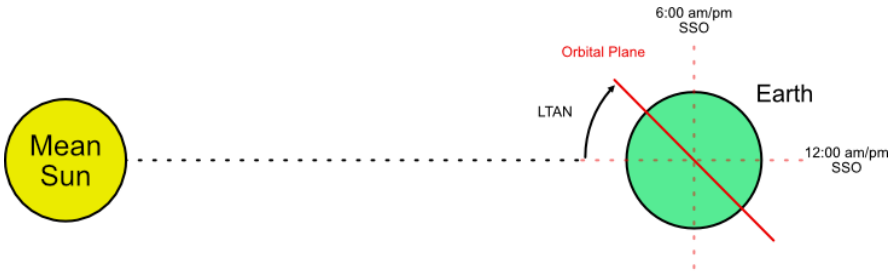

Figure 2.6: SSO LTAN/MLT

Next, we must remove our simplifying assumption and account for the effects of Earth's axial tilt (obliquity) and orbital eccentricity, which cause the Sun's position relative to the spacecraft's orbital plane to vary throughout the year. This variation reflects the difference between the positions of the real Sun and the fictitious Mean Sun. This difference can be approximated using Equations 4–10, adapted from [10], and simplified by assuming the year 2000, as the solar position remains relatively stable across years. In these equations, ε is the obliquity of Earth's orbit ($23.44°$), N_{day} is the day of the year, δ is the solar declination (in radians), and E is the equation of time (in radians). Although some intermediate parameters have physical significance, they are not relevant for our analysis. The true solar beta angle can then be computed using Equations 11, 12, and 13 from [8], where Ω_{LTAN} is the LTAN in radians, i is the orbital inclination, and δ and ε are derived from the previous equations. The result is an equation for the solar beta angle, β, that accounts for Earth's inclination

and orbital eccentricity.

$$M = 357.5291^\circ + 0.9856 \times (N_{day} - 1) \tag{4}$$

$$C = 1.9148^\circ \times \sin M + 0.02^\circ \times \sin 2M + 0.003^\circ \sin 3M \tag{5}$$

$$L_0 = 280.4665^\circ + 0.98564736^\circ \times (N - 1) \tag{6}$$

$$L = L_0 + C \tag{7}$$

$$y = \left(\tan \frac{\varepsilon}{2}\right)^2 \tag{8}$$

$$\delta = \arcsin\left(\sin \varepsilon \sin L\right) \tag{9}$$

$$\begin{aligned} E = & -y \times \sin 2L_0 + 2 \times 0.0167 \times \sin(M) \\ & - 4 \times 0.0167 \times y \times \sin M \times \cos 2L_0 \\ & + 0.5 \times y^2 \times \sin 4 \times L_0 \\ & + 1.25 \times 0.0167^2 \times \sin 2M \end{aligned} \tag{10}$$

$$\hat{s} = \begin{bmatrix} \cos \delta \cos \varepsilon \\ \cos \delta \sin \varepsilon \\ \sin \delta \end{bmatrix} \tag{11}$$

$$\hat{h} = \begin{bmatrix} \sin i \cos \Omega_{LTAN} \\ -\sin i \cos \Omega_{LTAN} \\ \cos i \end{bmatrix} \tag{12}$$

$$\beta = \arcsin(\hat{h} \cdot \hat{s}) \tag{13}$$

The validity of these equations can be quickly verified by comparing the computed beta angles to those generated by simulations in Ansys Systems Tool Kit (STK), a commercial spacecraft mission planning and simulation software. The comparison, shown in Figure 2.7, demonstrates a close match between the simulated and calculated values. Minor discrepancies are expected due to the approximations used, such as neglecting leap years and long-term variations in Earth's orbit and inclination. Nonetheless, the results are sufficiently

accurate for the purposes of this analysis.

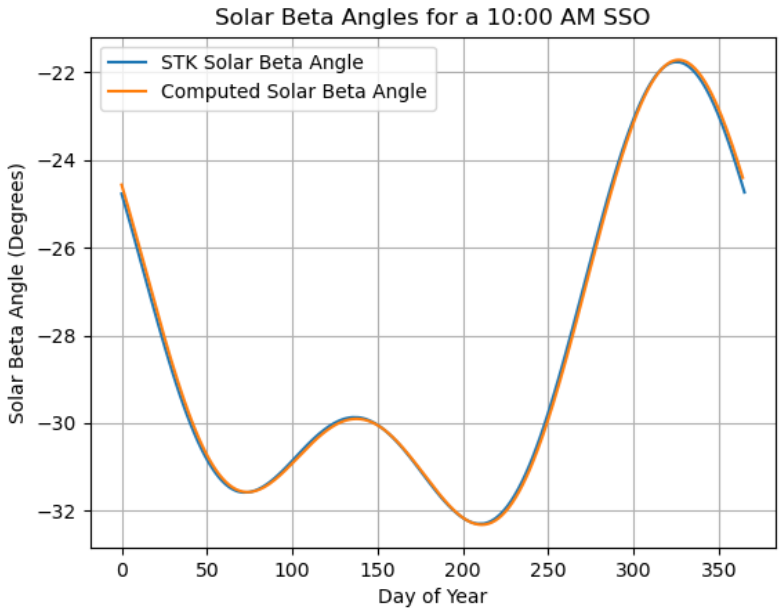

Figure 2.7: STK Simulated Beta Angle and Computed Beta Angle for the 2025 Epoch

Using the derived equations, we can plot the minimum and maximum beta angles encountered throughout the year as a function of the orbit's LTAN, shown in Figure 2.8. As expected, LTANs near noon or midnight correspond to beta angles near $0°$, while LTANs around 6 AM or 6 PM approach beta angles of $\pm 90°$. This relationship provides a quick reference for estimating the range of beta angles for a given LTAN, offering useful insights into how LTAN selection impacts a spacecraft's power generation.

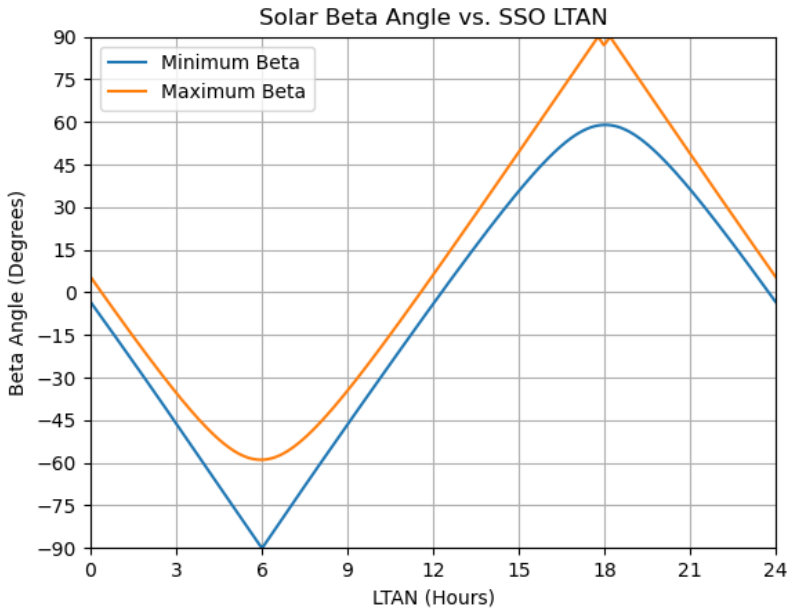

Figure 2.8: Minimum and Maximum Beta Angles vs LTAN for 520km circular SSO

2.2 PV Cells

Photovoltaic (PV) cells are the primary source of electrical power for most Earth-orbiting satellites [11]. For CubeSat and SmallSat applications, triple-junction gallium arsenide (GaAs) coverglass interconnected cells (CICs), produced by manufacturers such as Azure Space and Spectrolab, are commonly used due to their high efficiency; typically above 30% [12], [13].

Understanding the current-voltage (IV) characteristics of solar cells is essential for designing power systems that efficiently extract energy from them. An idealized IV relationship for a solar cell is given by [14]:

$$I = I_{SC} - I_0 \left(\exp \frac{qV}{mk_bT} - 1 \right), \tag{14}$$

where I is the output current, V is the voltage across the cell, I_{SC} is the short-circuit current, I_0 is the diode reverse saturation current, q is the elementary charge, k_b is Boltzmann's constant, T is the absolute temperature of the cell in Kelvin, and m is the diode ideality factor.

Figure 2.9 illustrates a typical IV curve for a solar cell, along with its corresponding power curve. The open-circuit voltage (V_{OC}) occurs when the output current is zero, while the short-circuit current (I_{SC}) corresponds to the condition when the output voltage is zero. Notably, there is a specific voltage less than V_{OC} where the product of current and voltage, or the power, is maximized. This operating point is known as the maximum power point (MPP).

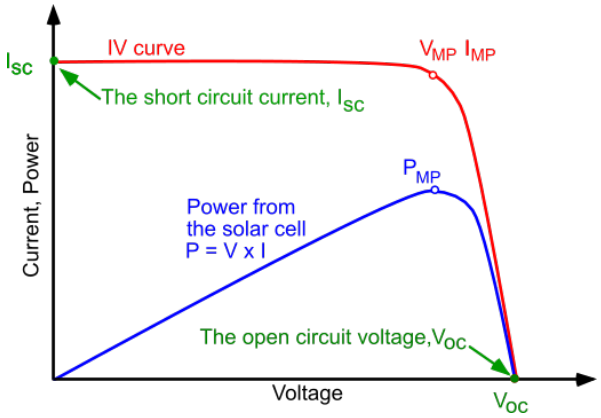

Figure 2.9: Typical Solar Cell IV and Power Curve from [15]

Equation 14 also highlights that the IV and power-voltage (PV) characteristics of a solar cell vary with temperature and illumination conditions. Manufacturers typically provide values for V_{OC}, I_{SC}, the maximum power voltage V_{MP}, and the maximum power current I_{MP}, along with temperature coefficients that describe how these parameters change with temperature. To maximize power extraction under varying conditions, the operating voltage of the solar cell must be dynamically adjusted to track the MPP, a process known as maximum power point tracking (MPPT).

2.3 Battery Characteristics

Batteries are a critical component in CubeSat electrical power systems, providing the energy storage necessary for continuous operation during eclipse periods and for peak power demands that exceed the instantaneous generation capacity of the solar arrays. The constraints inherent to CubeSat platforms, such as limited mass, volume, and thermal management capabilities, necessitate the use of compact, high energy-density battery technologies, with lithium-ion chemistry being the prevailing choice [11]. Understanding the fundamen-

tal characteristics of batteries, including state of charge, capacity, efficiency, and internal resistance, is crucial for the design of spacecraft power systems.

State of Charge (SoC) is a unit-less quantity that represents the charge status of a battery cell, defined as 100% when fully charged and 0% when fully discharged. It is important to note that "fully discharged" does not imply the cell is entirely depleted of charge; rather, it indicates that the cell has been discharged to a voltage cutoff selected to prevent damage or safety concerns [16]. While open-circuit voltage (OCV) is often used to infer SoC, terminal voltage under load is an unreliable indicator due to its dependence on temperature, hysteresis effects, and transient phenomena such as diffusion voltages [16].

The capacity of a cell characterizes its ability to store and deliver charge and energy, commonly specified in units of ampere-hours (Ah) or milliampere-hours (mAh). The total charge capacity is defined as the total charge extracted from the cell during a complete discharge from 100% SoC to 0% SoC, under ideal conditions at a very slow rate of discharge, and is considered a parameter of the cell model that does not depend on temperature or current. In contrast, the discharge capacity refers to the charge removed from the cell during a constant-rate discharge until the terminal voltage reaches the specified cutoff voltage. This quantity is dependent on discharge rate and temperature and is typically lower than the total capacity unless the discharge is performed at an infinitesimally slow rate. Energy capacity, measured in watt-hours (Wh), is computed as the product of the cell's nominal voltage and its nominal charge capacity. As the cell ages, it undergoes capacity fade due to irreversible side reactions that consume cyclable lithium and due to structural degradation within the electrode materials [16].

Recharge efficiency, also referred to as coulombic efficiency, quantifies the charge efficiency of the cell during cycling. During charging, a small portion of the charge passing through the cell is lost to reactions that do not contribute to increasing the SoC. For lithium-ion cells, coulombic efficiency is typically 99% or higher, although it is difficult to model precisely due to its dependence on SoC, current rate, temperature, and the internal electrochemical state of the cell. It is important to distinguish coulombic efficiency from energy efficiency, the latter being closer to 95% in lithium-ion cells due to resistive and entropic

losses during charge and discharge cycles. The variability in coulombic efficiency across cells within a battery pack is a primary driver of long-term imbalance, as the differences in SoC that develop during charging cycles are not neutralized during discharge [16].

The internal resistance of a cell, commonly modeled as equivalent series resistance (ESR), models the instantaneous voltage drop across the cell during current flow. This resistance is a function of the cell's state of charge and its internal temperature and generally increases over the cell's operational lifetime. Unlike differences in coulombic efficiency among cells, variations in internal resistance do not directly cause SoC imbalance but instead result in different loaded terminal voltages and can limit the maximum deliverable power of the pack [16].

2.4 Power Converters

Voltage regulators convert one voltage level to another, generally by using a closed-loop control system. In many designs, MOSFETs serve as the primary regulation element, either as a variable resistive pass element or as a high-speed switch. A control loop continuously measures the output voltage, compares it to a reference, and adjusts the MOSFET's operation to maintain the desired output.

2.4.1 Linear Regulators

Linear regulators, including low dropout regulators (LDOs), control the voltage drop across the device using an adjustable resistive element. This is typically achieved by modulating the gate-to-source voltage (V_{GS}) of a MOSFET to adjust its resistance ($R_{DS(on)}$), although bipolar transistors can also be used for this purpose [17]. This approach enables the regulator to maintain a stable output voltage despite variations in input voltage or load conditions. A block diagram of a typical linear regulator is shown in Figure 2.10.

As voltage regulation is achieved using a resistive element, the input current is approximately equal to the output current, plus a small amount of current consumed by the control circuitry. When the regulated output voltage is significantly lower than the input voltage, the regulator must dissipate the excess power as heat, leading to considerable power loss

and heat generation under high current loads. The main advantages of linear regulators are their simplicity and low output noise. However, they are inherently inefficient when the difference between input and output voltage is large.

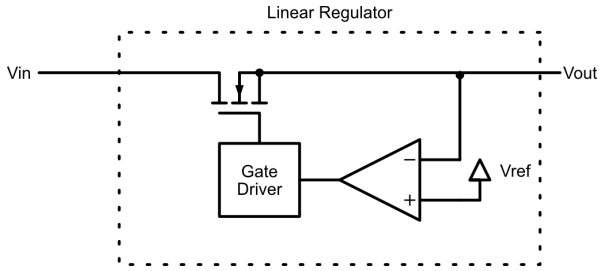

Figure 2.10: Linear Regulator Block Diagram

2.4.2 Switching Regulators

Unlike linear regulators, switching regulators, also known as switch-mode power supplies (SMPS), use reactive elements to step the input voltage up or down, rather than relying on resistive elements. This method avoids the inherent inefficiency of resistive voltage drops, with power losses only arising from the non-ideal characteristics of real components. SMPS circuits typically use MOSFETs to rapidly switch the connection between the power source and reactive elements, typically inductors. By adjusting the duty cycle of this switching process, the output voltage is regulated. Because the energy is transferred through inductive rather than resistive elements, SMPS can achieve high efficiency, even when there is a significant difference between input and output voltages. There are various topological configurations for combining switching and reactive elements in SMPS designs. However, this discussion will focus on three common types: the buck converter (step-down), the boost converter (step-up), and the four switch buck-boost converter (step-down/up).

Buck Regulator Figure 2.11 shows the basic structure and operation of a buck converter. At its core, a buck converter uses an LC filter to average a switching input voltage to a lower output voltage. This is expressed mathematically by Equation 15, where the output voltage of the buck converter is given by:

$$V_{out} = D \cdot V_{in}, \tag{15}$$

where V_{out} is the output voltage, V_{in} is the input voltage, and D is the duty cycle expressed as a value between 0 and 1 with 1 corresponding to the switch being always closed. The peak-to-peak values of the AC components of the inductor current output voltage, known as the ripple current and ripple voltage respectively, are given by [18]

$$\Delta I_L = \frac{(V_{in} - V_{out}) \times D}{f_s \times L} = V_{out} \left(1 - \frac{V_{out}}{V_{in}}\right) \frac{1}{f_s \times L}, \tag{16}$$

where ΔI_L is the inductor current ripple, f_s is the switching frequency, and L is the inductance. The approximate peak-to-peak output voltage ripple is:

$$\Delta V \approx \frac{\Delta I_L}{8 \times C \times f_s} + R_{ESR} \times \Delta I_L, \tag{17}$$

where ΔV is the output voltage ripple, C is the output capacitance, R_{ESR} is the equivalent series resistance of the output capacitor, and ΔI_L is as defined above. From these equations, we can note that the ripple voltage can be reduced by increasing the inductance, output capacitance, or switching frequency. However, increasing inductance or capacitance typically requires physically larger components, so higher switching frequencies are often preferred for compact designs, despite increased switching losses that can reduce efficiency, as discussed in later sections.

The diode in Figure 2.11 can be replaced with a second FET to create a synchronous buck converter. Synchronous converters generally achieve higher efficiency under heavy loads because the voltage drop across a conducting FET is lower than that across a diode. In contrast, asynchronous converters, which retain the diode, are simpler in design and can be more efficient at very light loads or during no-load conditions, since they require driving only a single FET. The analysis and equations presented here assume the buck converter is operating in continuous conduction mode (CCM), where the inductor current remains positive and never reaches zero. At low load conditions, if the DC component of the inductor current drops below $\frac{\Delta I_L}{2}$, the converter may either continue operating in CCM—allowing negative current flow or transition to discontinuous conduction mode (DCM). Figure 2.12 compares inductor current waveforms in these two modes. DCM is typically more efficient at light loads but results in increased output voltage ripple. While synchronous converters can operate in either CCM or DCM, asynchronous converters cannot allow negative induc-

tor current due to the diode and are therefore restricted to DCM operation at light loads. Many COTS buck converters offer selectable modes, allowing users to switch between CCM and DCM under light loads, or to reduce switching frequency to improve light-load efficiency.

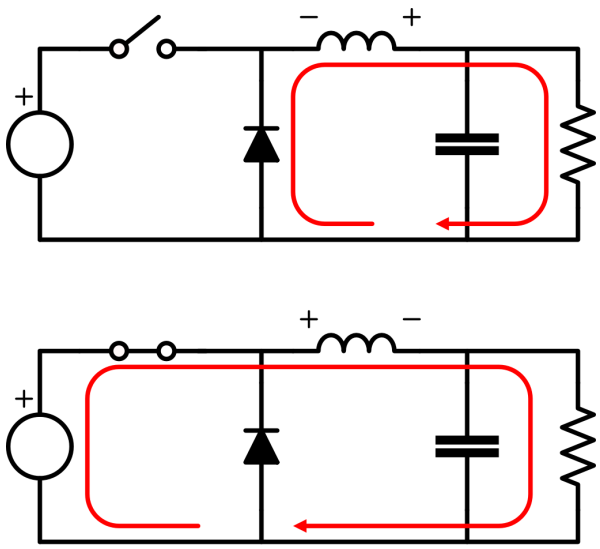

Figure 2.11: Buck regulator topology.

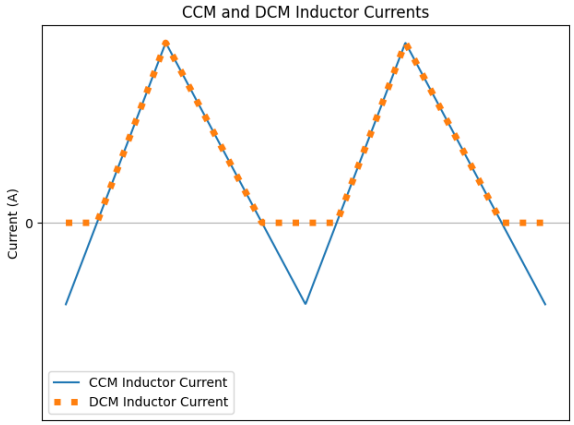

Figure 2.12: CCM vs DCM

Boost Boost converters produce an output voltage that is always higher than their input voltage. Figure 2.13 shows the basic structure and operation of a boost converter. The main difference between a buck and boost converter is that the inductor's voltage is added to the supply voltage as opposed to being subtracted from it. Additionally, when the switch is on and the inductor is being charged, all of the load current is being sourced via the

output filter capacitor as opposed to it being mainly sourced by the inductor in the case of a buck regulator. Equations 18-20 from [19] describe the duty cycle, ripple current, and ripple voltage of a boost converter. Notice that the ripple voltage now increases with load current, due to the load current being sourced from the output capacitor while the inductor is charging. The trade-offs between switching frequency, inductance, and capacitance are the same between buck and boost converters. Boost converters can be implemented as synchronous or asynchronous converters and can operate in DCM or CCM as with buck converters.

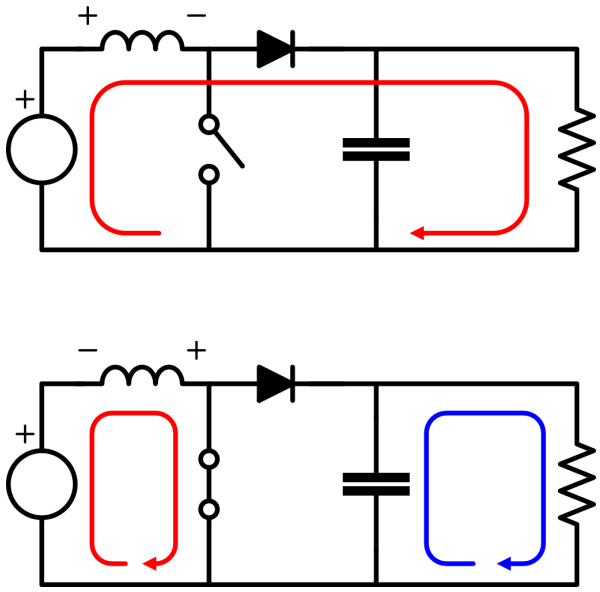

Figure 2.13: Boost Regulator Topology

$$V_{out} = \frac{V_{in}}{1 - D} \tag{18}$$

$$\Delta I_L = \frac{V_{in} \times D}{f_s \times L} \tag{19}$$

$$\Delta V \approx \frac{I_{OUT} \times D}{f_s \times C} + R_{ESR} \times \left(\frac{I_{OUT}}{1 - D} + \frac{\Delta I_L}{2} \right) \tag{20}$$

Buck/Boost The four switch Buck/Boost converter combines the switches needed for a buck and for a boost converter as shown in Figure 2.14; allowing it to operate as either a buck or a boost converter to step the input voltage up or down. The downside of this design is more complicated internal circuitry and control schemes and lower efficiency due to the

losses incurred by the extra FETs. The equations present for the buck converter apply when the converter is stepping down the input voltage and the boost converter equations apply when the input voltage is being stepped up.

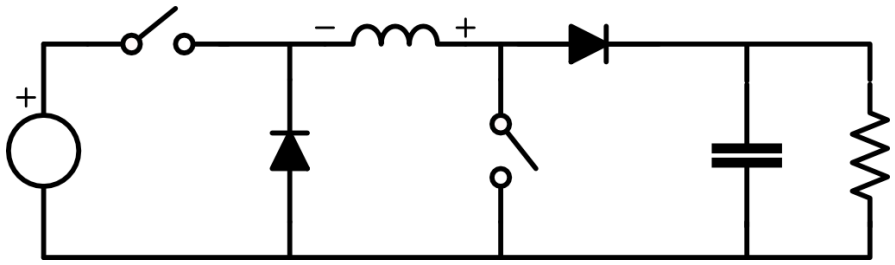

Figure 2.14: Buck/Boost Regulator Topology

2.4.3 Losses in Switching Converters

The majority of losses in a switch-mode power supply (SMPS) arise from conduction losses and switching losses. Conduction losses result from the DC resistance of the MOSFETs, inductors, and any diode forward voltage drop present in the circuit. Switching losses occur during the turn-on and turn-off transitions of the switching MOSFET(s). During these transitions, the MOSFET briefly passes through a high-resistance region, leading to elevated power dissipation. At lower output currents, losses are predominantly due to the energy required to charge and discharge the MOSFET gate capacitance, along with the power consumed by the SMPS control circuitry. Equations 21 to 23 summarize these relationships, based on simplified derivations from [20]. Switching losses can be reduced by lowering the switching frequency (f_{sw}); however, doing so requires larger inductance and output capacitance to maintain the same output voltage ripple. Alternatively, selecting MOSFETs with lower gate capacitance allows for faster transitions between on and off states, which also reduces switching losses. However, this often comes at the cost of higher MOSFET on-resistance, increasing conduction losses. Thus, optimizing SMPS efficiency involves carefully balancing these trade-offs.

$$P_{switching} \propto V \times I \times f_{sw} \tag{21}$$

$$P_{res} \propto I^2 \tag{22}$$

$$P_{static} \propto K \tag{23}$$

2.5 The Space Radiation Environment

The low Earth orbit (LEO) radiation environment is shaped by three primary sources: trapped particles, solar particle events (SPEs), and galactic cosmic rays (GCRs). Each of these contributes differently to the total radiation exposure experienced by spacecraft, with variations depending on orbital altitude, inclination, and space weather conditions. In polar orbits, the radiation environment is especially harsh due to the reduced strength of the Earth's magnetic shielding over the poles and more direct exposure to energetic particles[21].

Trapped particles are energetic protons and electrons confined by Earth's magnetic field within the Van Allen radiation belts. These belts consist of an inner region and an outer region. Though the belts are most intense at equatorial latitudes, polar and high-inclination orbits are still affected, especially where the belts curve downward at the poles, forming the so-called polar horns. Additionally, the South Atlantic Anomaly (SAA), where the inner belt dips closest to Earth's surface, increases radiation exposure for satellites even in low-altitude polar orbits[21]. The real-world effect of the SAA can clearly be seen in Figure 2.15, that plots the locations where SEU were observed in DRAM onboard the ADEOS-II spacecraft.

Solar particle events (SPEs), such as coronal mass ejections (CME), are transient bursts of high energy protons and heavier ions ejected from the Sun during solar flares and coronal mass ejections. Although the Earth's magnetic field deflects many of these particles, this shielding is weakest over the poles, making polar orbiting spacecraft more vulnerable during solar storms. SPEs can dramatically increase local radiation doses over short periods, potentially damaging spacecraft electronics [21].

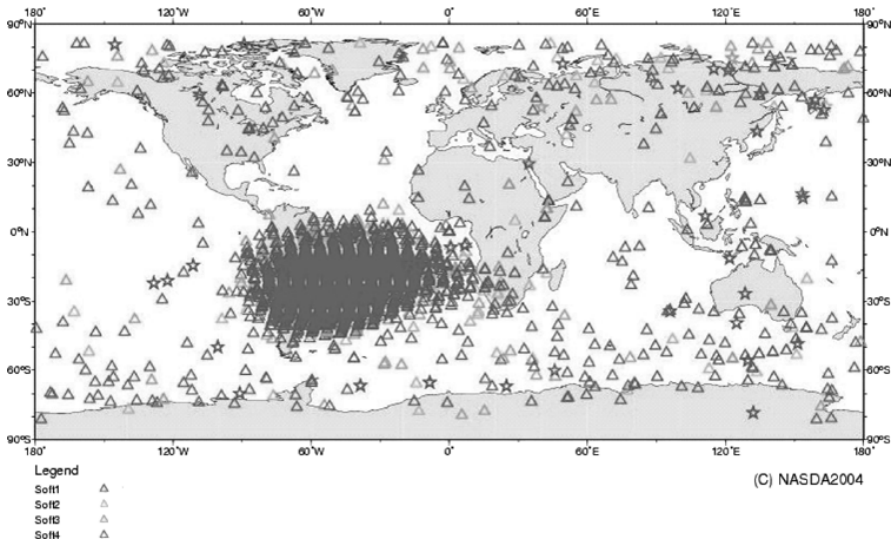

Figure 2.15: Map of SEU Observed on the ADEOS-II Spacecraft [22]

Galactic cosmic rays (GCRs) originate from beyond the solar system and are produced by high energy astrophysical processes such as supernovae [23]. These fully ionized atomic nuclei have very high energy levels and pass through spacecraft shielding. Although the Earth's magnetic field provides partial shielding, this is significantly reduced at high latitudes, increasing GCR exposure in polar orbits [21].

2.6 Radiation Effects on Electronics

There are three broad categories of radiation effects on electronics that will be considered: Ionization, Displacement Damage, and Single-Event Effects (SEE)[24]. Ionization and displacement damage are cumulative effects caused by long-term exposure to radiation; in contrast, SEEs are probabilistic events triggered by single random interactions with a high energy particle.

2.6.1 TID Effects

As ionizing radiation deposits energy in CMOS and bipolar devices, it generates electron hole pairs. Positively charged holes can become trapped in the insulating oxide layers in bipolar devices and the gate oxides in MOS devices. This shifts the MOSFET threshold voltages as a result of persistent positive bias in the gate oxide in MOS devices and degrades the gain of bipolar devices [25]. The total ionizing dose (TID) quantifies the cumulative energy absorbed per unit mass; this is typically measured in rad or Gy (100 rad = 1 Gy = 1

J/kg). TID-induced damage is typically exacerbated when a strong electric field is present, as this results in more deposited charge per incident particle [25]. This results in biased devices degrading faster than unbiased devices when exposed to radiation. The effects of TID induced damage vary between devices; quiescent and leakage/bias currents will typically increase for CMOS and bipolar devices[24] and various other device parameters, such as timing or voltage references/thresholds, may change for more complex devices[26]. Typically, non radiation tolerant/hardened COTS devices are safe to use up to doses of around 5-10 krad; however, some devices may suffer from parametric degradation at doses as low as 2 krad[27]. As TID is mainly accumulated from low energy protons and electrons, small amounts of aluminum shielding can be used to significantly reduce the dose received by components[26].

An additional complication when testing for TID effects is Enhanced Low Dose Rate Sensitivity (ELDRS), which primarily affects bipolar technologies. Certain bipolar devices can experience greater degradation when exposed to radiation at a low dose rate than at a higher dose rate [25]. As a result, environments with low continuous radiation, such as deep space, can be more damaging to bipolar components than the short bursts of intense radiation encountered during typical radiation tests.

2.6.2 DDD Effects

Displacement Damage Dose (DDD) refers to the degradation caused by high energy particles, such as protons and electrons, physically displacing atoms within the silicon crystal lattice[25]. DDD primarily impacts components like solar cells and CCD image sensors, where crystal integrity is crucial for performance. For example, in CCD cameras, displacement damage can increase dark current and reduce sensitivity, while in solar panels it leads to decreased power output[24]. However, MOSFET devices are largely insensitive to DDD, as their operation depends more on the oxide charge and interface quality than on bulk silicon properties[25].

2.6.3 Single Event Effects

Single Event Effects (SEEs) cover a wide range of destructive and non-destructive effects caused by high energy particles depositing energy into semiconductor devices. As the effects occur due to single-particle interactions, they occur randomly at a constant rate determined by the radiation environment. Radiation shielding generally cannot reduce the SEE rate of a device, as SEEs are primarily caused by high energy particles that are not stopped by shielding. Large amounts of shielding can even increase the SEE rate due to a single high energy particle producing many slightly lower-energy particles after interacting with the shielding[24].

Single Event Latch-Up A Single Event Latch-Up (SEL) is a potentially destructive effect that occurs when a high energy particle activates the parasitic SCR structure present in most CMOS devices. This results in both sides of complementary pair of MOS structures becoming "Latched" on, resulting in a short circuit between a device's power supply and ground through the CMOS gate. The condition will persist until the device is powered cycled. A SEL is not inherently damaging to the device; however, the high current condition can result in thermal damage to the device (Ex. bond wires melting) if it is not removed quickly[28].

Single Event Gate Rupture Single Event Gate Rupture (SEGR) is a destructive effect that typically affects power MOSFETs. A SEGR occurs when a high energy particle causes a large electric field across the gate oxide of a MOSFET, exceeding the breakdown voltage of the oxide layer. This results in the gate electrode becoming short circuited to the body of the MOSFET, destroying the device [29]. Higher gate to source and drain to source voltages increase the chance of SEGR, so heavily derating the parameters of power MOSFET devices can reduce the chance of a SEGR occurring[26].

Single Event Burnout Single-Event Burnout (SEB) is a potential destructive effect in N-channel power MOSFETs caused by a high energy particle strike when a high drain to source voltage is present on the device. The particle can trigger an uncontrolled current surge and avalanche breakdown, permanently damaging the device. Similarly to SEL, SEB is not inherently damaging, but the high current condition it produces will often damage the device

if not removed immediately[29].

Single Event Upset A single event upset (SEU) is a "bit-flip" in a memory element caused by a high energy particle interaction. SEUs should be considered for any devices that have internal memory, such as microcontrollers or configurable devices[30]. Special considerations should be given to ensure that no configuration of a device can damage the system. For example, current limiting resistors should be used to prevent an input pin from being reconfigured as an output pin from shorting out. Error detection and correction circuits on memory can be used to correct SEU induced bit flips, and configuration "scrubbing," where a configuration is periodically re-written to a device, can be used to ensure that configurable devices stay configured correctly [26].

Single Event Functional Interrupt A single event functional interrupt (SEFI) is a generic term for a non-damaging SEE that causes a device to stop working until it is power cycled, ex. due to an SEU corrupting some internal state of the device [24]. Watchdog timers or frequent power cycles can be used to mitigate SEFI.

Single Event Transient Single event transients (SET) are short voltage exertions within the circuit caused by high energy particles. In the case of digital logic, a SET could be captured by a memory element and cause a SEU. Both linear and switching power regulators are also susceptible to SET, so special care should be taken to ensure any sensitive downstream devices are protected from momentary over-voltage transients. In the case of analog signals, SETs generally just appear as additional noise and can be reduced using low pass filtering [24].

Stuck Bits In addition to SEUs, high energy particles can cause a bit of memory to become permanently stuck in one state [24]. Depending on the location of the stuck bit, this can have severe effects and even render components inoperable. For example, if one of the instructions used to boot a MCU became corrupted, the MCU would be rendered inoperable. A single stuck bit can be partially mitigated with SECDED EDAC; however, no additional SEU induced bit flips in that word will be able to be corrected.

2.6.4 Summary of Effects & Mitigation

The preferred mitigation strategy for all radiation effects is the selection of radiation tolerant or hardened components; however, due to their high cost, this is often not feasible for small CubeSat missions. Table 2.1 summarizes the previously presented radiation effects and simple mitigation strategies that are generally feasible for CubeSat missions.

Radiation Effect	**Affected Component Types**	**Mitigation Strategies**
Total Ionizing Dose (TID)	CMOS devices, bipolar devices	- Aluminum shielding (TID < 10 krad) - Power off components when unused - Design with large margins to allow for parametric degradation
Displacement Damage Dose (DDD)	Solar cells, CCD sensors	- Plan for degradation
Single Event Latch-Up (SEL)	CMOS devices	- Active or passive over-current limiting with frequent power cycles
Single Event Gate Rupture (SEGR)	Power MOSFETs	- V_{GS} and V_{DS} derating
Single Event Burnout (SEB)	N-channel Power MOSFETs	- V_{DS} derating - Use P-Channel MOSFETs
Single Event Upset (SEU)	Microcontrollers, SRAM, Flash, FPGAs	- ECC/EDAC on critical memory - Configuration scrubbing - Avoid using devices with memory for critical functions
Single Event Functional Interrupt (SEFI)	Microcontrollers, FPGAs	- Watchdog timers - Periodic power cycling
Single Event Transient (SET)	Analog circuits, regulators, ADCs/DACs	- Low-pass filtering/digital averaging - Over-voltage protection for sensitive devices
Stuck Bits	Memory, configuration registers	- ECC/EDAC - Avoid using devices with memory for critical functions

Table 2.1: Summary of Radiation Effects, Affected Components, and Mitigation Strategies

3 System Requirements

The system requirements for the MARMOTSat Electrical Power System (EPS) are derived from both mission objectives and external constraints imposed by launch providers. MARMOTSat's primary mission objective is to demonstrate the Modular CubeSat Radio (MCR) through a variety of amateur radio and scientific experiments. A minimum payload duty cycle of 10% is required to fully service Canada with the amateur radio experiments; however, higher duty cycles are also desirable. Several EPS requirements are mandated by the launch provider; specifically, that the spacecraft must be fully powered down when in the deployer [31]. The following sections detail the specific system-level requirements governing EPS design, energy generation, storage, and power conditioning necessary for mission success.

3.1 Inhibit Requirements

The goal of the inhibit system is to ensure that the spacecraft remains fully powered off while inserted in the deployer and powers on automatically upon deployment. This is a strict requirement from the SpaceX Rideshare Payload User Guide (RPUG) [31]. Although the spacecraft is permitted to power up immediately after deployment, it must wait several minutes before beginning RF transmissions or deploying any mechanical appendages. To simplify system design, the deployment and transmission timers are implemented in software on the OBC and are not considered further in this discussion. Additionally, a Remove Before Flight (RBF) mechanism is required to force the spacecraft into the pre-deployment (powered-off) state, enabling testing and transport. The inhibit system must also function if the spacecraft's batteries become fully depleted, either in flight or prior to deployment, ensuring the spacecraft can recover from such scenarios. Since the spacecraft may be integrated into the deployer several months before launch, the current draw of the inhibit system must be minimal while the spacecraft is in its powered-off state to prevent battery depletion before launch. Finally, a fail-safe mechanism is included to allow the OBC to power-cycle the entire spacecraft via a "heartbeat" signal. If the heartbeat is not toggled periodically, the spacecraft will automatically power cycle. These objectives are formalized in the requirements listed below:

1. The inhibit system shall be activated when the deployment switches or RBF mechanism is active

2. The inhibit system shall be deactivated when all of the conditions listed below are met:

   (a) The deployment switches are not depressed

   (b) The RBF mechanism is not active

   (c) The spacecraft's batteries are not depleted or the spacecraft is in sunlight

3. The inhibit system shall inhibit power to all subsystems when active

4. The current into or out of the battery pack shall be less than 100 uA when the spacecraft is in the stowed state

5. The inhibit system shall inhibit power to all subsystems for 10 seconds if the spacecraft heartbeat signal is not asserted periodically

3.2 Power Conditioning and Distribution Requirements

Table 3.1 summarizes the required voltages and maximum expected currents for all spacecraft subsystems. These values are based on datasheet specifications for commercial off-the-shelf (COTS) components and measured or design values for in-house developed components. Most subsystems, with the exception of the payload and the ADCS VBAT channel, require tightly regulated voltages. The payload includes its own internal voltage regulation and can be powered directly from the spacecraft battery. Similarly, the ADCS VBAT channel supplies power to the ADCS reaction wheels, which can operate over a wide input voltage range.

We also require an average end-to-end efficiency of 75% or greater. While somewhat arbitrary, this target is both achievable and, as the power budget section will demonstrate, sufficient for spacecraft operations. This figure accounts for all losses, including those from power converters and battery charging. For this requirement, we conservatively assume that all energy is transferred through the battery, as battery usage varies significantly depending on the orbit LTAN and the durations of eclipse and daylight payload operations.

Channel	Maximum Current	Min Voltage	Max Voltage	Max Ripple
5V5 TTC	1.5 A	5.4 V	6 V	N/A
5V ADCS[32]	0.6 A	5 V	5.25 V	N/A
5V5 BURN	2.7 A	4 V	5.5 V	N/A
3V3 ADCS[32]	0.6 A	3.2 V	3.5 V	N/A
3V3 CDH	0.15 A	3.1 V	3.4 V	N/A
3V3 GNSS[33]	1.7 A	3.135 V	3.465 V	100 mVpp
VBAT ADCS[34]	2 A	8 V	18 V	N/A
VBAT PAY	2.5 A	6 V	24 V	N/A

Table 3.1: Subsystem Power Regulation Requirements

Assuming a 95% battery recharge efficiency, the required efficiency for the power regulation stages is:

$$\frac{0.75}{0.95} \approx 80\%$$

Given that the selected EPS architecture requires all power to pass through two regulators,the battery charge regulator (BCR) and a power conditioning and distribution (PCD) regulator, each regulator must achieve an efficiency of:

$$\sqrt{0.8} \approx 90\%$$

This is a relatively loose requirement, but it provides clear design targets for the regulators. This is summarized in Table 3.2.

Component	Efficiency
Battery	$> 95\%$
BCR	$> 90\%$
PCD	$> 90\%$

Table 3.2: EPS Efficiency Requirements

3.3 Energy Storage and Generation Requirements

The MARMOTSat mission requires a minimum payload duty cycle of 10%, so the EPS energy generation and storage must be sized to meet this. Additionally, during the LEOPs phase, the EPS must provide sufficient power for the spacecraft to be detumbled so that antennas and solar arrays can be safely deployed. MARMOTSat is expected to have a mission

life of approximately 5 years, so the EPS should allow the spacecraft to remain operational for the full mission. As fully estimating battery and PV cell decay can be difficult and require a large amount of experimental data, the last requirement is somewhat soft and will generally be met on a best effort basis by ensuring large BoL margins on energy generation and storage. The requirements are formalized as shall statements below:

- The EPS shall provide sufficient energy generation and storage to operate the MCR payload at a 10% duty cycle
- The EPS shall provide sufficient energy generation and storage to de-tumble the spacecraft during LEOPS
- The EPS energy generation and storage shall allow the spacecraft to remain operation for a minimum of 5 years

3.4 Reliability and Radiation Mitigation Requirements

As the EPS must operate in the harsh space environment for several years, some consideration must be given to the reliability and radiation tolerance of the design. Due to the limited development time and budget, the general approach to this is to keep the design as simple as possible and heavily derate components where appropriate. More complicated systems typically used in larger missions, such as triple modular redundancy or cross strapping, can generally only replace one failure point with another. These systems add significant complexity to the design, and it is difficult to quantify if they improve the reliability of the entire system, as the radiation performance of the COTS components is difficult to predict without extensive testing[26]. The following requirements attempt to ensure that the EPS is as reliable as practical:

- The EPS shall ensure that a short circuit or over-current event (Ex. SEL) within a subsystem does not damage the EPS and does not effect other subsystems.
- The EPS shall protect powered subsystems from SET on the EPS regulated voltage channels
- All MLCC on the EPS shall be soft terminated to reduce the risk of cracking due to thermal or mechanical stress

- All EPS components shall be rated for an operating temperature range of at least -40 ℃ to 85 ℃.
- The EPS subsystem shall comply with NASA guidelines for selecting all non-metallic materials based on available outgassing data. The subsystem shall not utilize any non-metallic materials with a Total Mass Loss (TML) greater than 1.0 percent or a Collected Volatile Condensable Material (CVCM) value of greater than 0.1 percent.
- SEUs in configurable elements of the EPS shall not result in damaging events (Ex. add current limiting resistors to an MCU input port, so it getting reconfigured to an output port will not result in an over-current condition)
- All power MOSFETs and power MOSFETs based devices drain to source voltage shall be derated by a factor of at least 0.5 and by 0.2 when possible (Ex. a FET with a 5V V_{DS} rating should have its V_{DS} exceed 1V in the design) to reduce the risk of SEGR or SEB[26].

4 Power Budget

A power budget is used to compare the energy a spacecraft generates to the energy required for spacecraft operations. If the size of the spacecraft is not fixed, this analysis can be used to determine the required solar array area and battery capacity. In the case of small academic CubeSat missions, like MARMOTSat, the size of the spacecraft is generally fixed with limited feasible options for gaining large amounts of additional solar array area. For these types of missions, the power budget generally acts as a constraint on the scope of the mission as well as informing decisions regarding solar cell placement and spacecraft attitude. The MARMOTSat mission is somewhat unusual, in that there are no strict requirements for how often the payload must operate. A minimum duty cycle of 10% was chosen to allow for coverage of Canada by the Amateur Radio experiments; however, higher duty cycles are also beneficial and lower duty cycles could still achieve most mission objectives. This drove the design of the EPS to maximize power generation while maintaining the 3U structure and avoiding complex and costly "double" deployable panels.

4.1 System Loads

Estimating spacecraft power usage is a critical step in developing the power budget, requiring the power consumption of each subsystem to be measured or estimated. For the MARMOTSat mission, flight-like models of the OBC and TT&C boards were available from the outset, as their designs were reused from the ORCASat mission. This enabled direct power measurements on the bench as well as validation through ORCASat telemetry. The payload was developed specifically for MARMOTSat, so its power consumption was estimated using a combination of datasheet specifications and prototype measurements. The ADCS power consumption was estimated based on manufacturer data, though it is the most challenging to predict in flight due to its dependence on drag, radiation pressure, and other environmental disturbances. Given the presence of the large HF antenna, these disturbances are expected to be significant, especially toward the end of the mission as atmospheric drag increases with orbital decay. The purpose of this analysis is to determine the spacecraft's required power generation capacity.

TT&C System Load The TT&C subsystem's power consumption depends on whether it is transmitting or receiving, so estimating the maximum transmit duty cycle is necessary. The TT&C team determined that the spacecraft will be within range of the ground station for approximately 15 minutes per day, with each pass lasting around 5 minutes. Although nominal operations require less than 5 minutes of daily contact to downlink telemetry, a conservative estimate assumes the spacecraft transmits 100% of the time while in range. This results in a transmit duty cycle of:

$$\frac{15 \text{ minutes/day (TX)}}{1440 \text{ minutes/day (total)}} \approx 1\%$$

The TT&C power consumption, based on prototype board measurements provided by the TT&C team, is summarized in Table 4.1.

Mode	**Duty Cycle**	**Voltage**	**Current**	**Power**
Receive	99%	5.5 V	15.7 mA	350 mW
Transmit	1%	5.5 V	1.1 A	6 W
Average Power	-	-	-	403 mW

Table 4.1: TT&C Subsystem Power Consumption

CDH System Load The C&DH subsystems has two sub-components: the on-board computer (OBC) and a Novatel OEM719 GNSS receiver. The OBC is always on; however, it can be configured to enter a low power mode when it is idle to reduce power consumption. To be conservative, we will not count on the OBC entering its low power mode as it is not used by default. The GNSS receiver is periodically turned on to acquire the current time as well as the spacecraft's position and velocity. This does not need to occur any more frequently than once per orbit; during nominal operation and it is likely that this will be done once per day at most. Making the conservative assumption that the GNSS receiver takes 9 minutes to acquire a lock and that it is used once per orbit, gives a duty cycle of approximately 10%.

ADCS System Load MARMOTSat uses a COTS ADCS system manufactured by CubeSpace, all power usage estimates come from the ADCS and Reaction wheel ICDs [32], [34]. Note that the "CubeWheel" power consumption varies depending on the current wheel speed and torque; for the power budget, it is assumed that wheels are biased to approxi-

Mode/Component	Duty Cycle	Voltage	Current	Power
OBC Active	100%	3.3 V	69 mA	230 mW
OBC Idle	0%	3.3 V	49 mA	160 mW
OEM719 GNSS Reviver [33]	10%	3.3 V	390 mA	1.3 W
Average Power	-	-	-	360 mW

Table 4.2: C&DH Subsystem Power Consumption

mately half of their maximum momentum and are in steady state (not exerting any torque on the spacecraft). The CubeTorque duty cycle also varies depending on the external disturbances applied to the spacecraft. A value of 10% is typical for most CubeSat [32]; however, the HF antenna will significantly increase atmospheric drag, so it will likely be higher. The maximum duty cycle is 80% to allow sampling the magnetometers when the MT are turned off. A value of 20% is assumed for nominal operations. ADCS power consumption is summarized in Table 4.3.

Component	Duty Cycle	Voltage	Current	Power
CubeComputer [32]	100%	3.3 V	70 mA	231 mW
CubeMag Compact [32]	100%	3.3 V	15 mA	70 mW
CubeMag Deploy [32]	100%	3.3 V	15 mA	70 mW
CubeSense Sun [32]	100%	3.3 V	28 mA	93 mW
3× CubeWheel (control) [32]	100%	3.3 V	66 mA	218 mW
3× CubeTorqure CR004 [32]	20%	5 V	375 mA	1.875 W
3× CubeWheel CW0057 [34]	100%	8 V	150 mA	1.2 W
Average Power	-	-	-	2.26 W

Table 4.3: C&DH Subsystem Power Consumption

Payload System Load Payload power estimates are shown in Table 4.4, the numbers are estimates from prototypes or datasheet values. All nominal payload modes use approximately 11W of power, so different operating modes will not be considered separately for the purposes of the power budget. The high-power HF modes are only intended to be used for very short periods of time; therefore, limited consideration will be given to them.

EPS System Load The EPS PMU system designed to draw less than 50 mW when it is active. This power level of consumption was chosen because it is relatively easy to achieve and does not have a significant impact on the spacecraft's power usage. Power usage by the power conversion portions of the EPS is not considered here, as their power usage is

Component	Duty Cycle	Voltage	Current	Power
Payload Computer	100%	Internally Regulated	N/A	3 W
SDR	100%	Internally Regulated	N/A	3 W
VHF Module	0-100%	Internally Regulated	N/A	5 W
HF PA Module	0-100%	Internally Regulated	N/A	5 W or 10 W
Camera	0-100%	Internally Regulated	N/A	260 mW
Core Power	-	-	-	6 W
VHF Modes	-	-	-	11 W
HF Modes	-	-	-	11 W
HF High Power Modes	-	-	-	16 W
DVB-S2 Power	-	-	-	11.26 W

Table 4.4: Payload Core Power

accounted for by the converter efficiency. Lastly, the inhibit and deployment circuitry is required to draw minimal power to avoid draining the battery while awaiting launch and deployment. Its power draw accounts for much less than 0.1% of the spacecraft's power usage, so it is also not considered here.

4.2 Spacecraft Modes

Table 4.5 summarizes the spacecraft operating modes that will be encountered during the mission and Table 4.6 summarizes the power consumption for each mode. The orbit average power (OAP) generation for each mode is calculated by assuming a 10% payload duty cycle, with the spacecraft in standby mode when the payload is not active.

4.3 Spacecraft Attitudes

The power generation of a spacecraft is highly dependent on the attitude of the spacecraft and the solar panel placement. We will begin by considering the different attitudes that the spacecraft may encounter during the mission; the energy generation for each attitude will then be analyzed. A brief description and explanation is given for each mode in Table 4.7 and Figure 4.1 shows the spacecraft's nominal and EoL orientations with respect to the earth.

Mode	Description
Safe Mode	In this mode, only the TT&C and C&DH subsystems are active. This is the lowest power consumption mode that allows the spacecraft to remain operational.
Low-Rate Detumble Mode	The spacecraft is detumbled using only a single MT at a time. This mode is capable of detumbling the spacecraft after deployment.
High-Rate Detumble Mode	The spacecraft is detumbled using all three MTs simultaneously. This mode is used if the spacecraft rotation exceeds the maximum rate that the low-rate mode can correct (e.g., due to reaction wheels spinning down).
LEOPS Mode	The ADCS is active with its reaction wheels disabled. This enables basic attitude control, such as Y-Thompson spin, while reducing power consumption during LEOPS before the solar array is deployed.
Standby Mode	All subsystems except the payload are fully active, and all ADCS control modes are available.
Payload Mode	The payload is active with either the VHF or HF module powered on and transmitting or receiving. Since both modules consume similar power, they are not distinguished separately in the power budget.
High Power Payload Mode	The payload HF module is powered on and transmitting in its high-power mode.

Table 4.5: Spacecraft Operating Modes

Mode	TTC	ADCS	CDH	EPS	PAY	Total	OAP
Safe	0.4 W	0 W	0.23 W	0 W	0 W	0.63 W	0.63 W
Low-Rate Detumble	0.4 W	0.96 W	0.36 W	0.05 W	0 W	1.77 W	1.77 W
High-Rate Detumble	0.4 W	1.96 W	0.36 W	0.05 W	0 W	2.77 W	2.77 W
LEOPS	0.4 W	0.84 W	0.36 W	0.05 W	0 W	1.65 W	1.65 W
Standby	0.4 W	2.26 W	0.36 W	0.05 W	0 W	3.07 W	3.07 W
Payload	0.4 W	2.26 W	0.36 W	0.05 W	11 W	14.07 W	4.17 W
High Power Payload	0.4 W	2.26 W	0.36 W	0.05 W	16 W	18.07 W	4.57 W

Table 4.6: Operating Modes Average Power

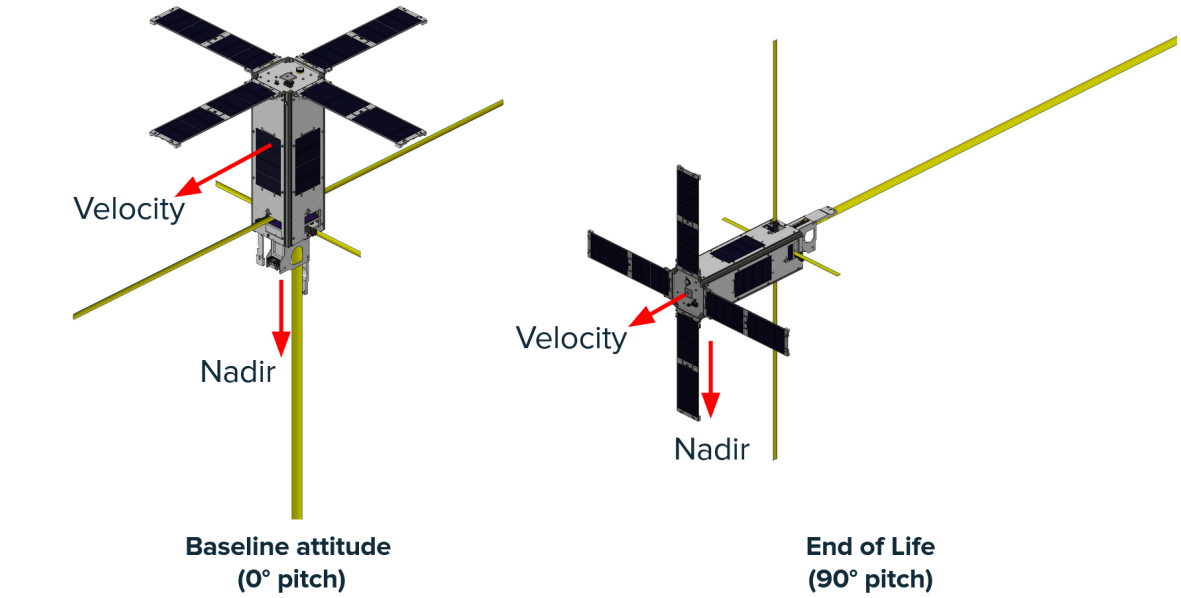

Figure 4.1: Spacecraft Attitudes

Mode	Description
Random Tumble	In this mode the spacecraft is randomly tumbling with no attitude control. This will occur after deployment and if the spacraft looses attitude control at any point during the mission (ex. due to an unexpected reset disabling the ADCS)
Y-Thompson	In this mode the spacecraft is only spinning about its Y axis and the Y axis is aligned with the orbit normal vector. This mode only requires magnetorquer control and is one of the modes that the spacecraft can be de-tumbled into. This mode must be entered prior to switching to Sun or nadir pointing modes.
Z-Thompson	This mode is identical to Y-Thompson, except that the spacecraft is spinning about its Z axis and the Z axis is aligned with the orbit normal vector.
+Z Nadir	In this mode the +Z spacecraft axis is pointing in the nadir direction and the +X axis is pointing in the direction of velocity. This mode ensures that the antennas are oriented correctly with respect to the ground and will be used for all TT&C or payload operations.
+X Nadir	In this mode the +X spacecraft axis is pointing in the nadir direction and the -Z axis is pointing in the direction of velocity. This minimizes disturbance torques induced by HF antenna drag, reducing the amount of torque the ADCS magnetorques need to exert. At low altitudes, this is the only mode the ADCS will be able to control the spacecraft in.
Sun Pointing	In this mode the deployable solar array is always pointing towards the Sun, this maximizes power generation at the cost of reducing antenna performance. Entering this mode at high and low latitudes allows for increased power generation without impacting TT& or payload as these subsystems are not active at these lattitudes.

Table 4.7: Spacecraft Pointing Modes

4.4 Expected Orbit

The local time of ascending node (LTAN) of a Sun-Synchronous orbit (SSO) is critical for modeling spacecraft power generation, as it determines the beta angles the spacecraft will experience throughout the year, which in turn affect the relative position of the Sun and the duration of orbital eclipses. Unfortunately, SpaceX does not publish the exact orbital parameters for Transporter missions until several months before launch. As a result, we must estimate the expected orbital parameters based on past Transporter missions.

Using data from [35] and [36], we estimate the LTANs of previous SpaceX Transporter launches by analyzing the TLEs of satellites known to have flown on these missions. The results are summarized in Table 4.8. Notably, all LTANs are within 1–3 hours of a 12:00 am or 12:00 pm SSO, which is expected since these orbits are preferred for Earth imaging applications [8]. For the purposes of power budgeting, we assume the orbit will have an LTAN within this range; a more detailed analysis will be performed once the exact LTAN is confirmed.

Mission	LTAN (h)
Transporter 1	21.58
Transporter 2	2.12
Transporter 3	22.00
Transporter 4	22.86
Transporter 5	1.12
Transporter 6	21.49
Transporter 7	10.43
Transporter 8	1.29
Transporter 9	22.64
Transporter 10	1.70
Transporter 11	22.78
Transporter 12	22.80
Transporter 13	10.31

Table 4.8: LTAN values for SpaceX Transporter missions

The orbital altitude is also known to be between 520 km and 620 km. For the purposes of power budgeting, the lower bound of 520 km is assumed, as it results in slightly higher eclipse fractions than higher orbits and therefore lower power generation, providing a conservative estimate for system design.

4.5 Stowed Energy Generation

Now that we have estimated the energy generation requirements and orbital parameters, we must ensure that the spacecraft can generate the required power for all expected orbits. We will begin by considering the spacecraft's power generation with only body-mounted solar cells, to estimate power generation before the solar array has been deployed and demonstrate the need for a deployable solar array. Using the basic orbit equations and geometry previously described, we will construct a simple analytical model for spacecraft power generation as a function of the beta angle. This allows for rapid analysis of different spacecraft attitudes and solar array configurations as well as providing basic intuition into the problem. Table 4.9 summarizes the key equations used to estimate power generation, and Equation 24 provides the orbit average power (OAP) generated by the spacecraft, assuming that the solar panels are never shaded by parts of the spacecraft.

Description	**Equation**	**Explanation**
Orbit period	$T_{\text{circular}} = \frac{2\pi}{\sqrt{\mu}}(h + R_E)^{\frac{3}{2}}$	The period of a circular orbit at an altitude of h
Angular size of the earth	$\rho = \arcsin \frac{R_E}{R_E + h}$	The angular size of the arch as seen at an altitude of h, taken from SMAD [37]
Eclipse start/stop angle	$\cos \frac{\Phi}{2} = \frac{\cos \rho}{\cos \beta}$	The spacecraft is in eclipse when $-\frac{\Phi}{2} < \theta < \frac{\Phi}{2}$ taken from SMAD [37]
Sun vector	$\hat{\mathbf{s}} = \begin{bmatrix} \sin\theta\cos\beta \\ \sin\beta \\ \cos\theta\cos\beta \end{bmatrix}$	The Sun vector in the spacecraft nadir coordinates as a function of true anomaly and beta angle (adapted from SMAD [37]).
Solar panel power generation	$P = \hat{\mathbf{s}} \cdot \hat{\mathbf{n}} \times A \times P_{AM0} \times \eta_{PV}$	Solar panel power generation is proportional to the dot product of the Sun vector and PV cell normal vector

Table 4.9: Key Equations for Estimating Spacecraft Power Generation

$$P = \sum_{i=0}^{N} A_i P_{AM0} \eta_{PV} \int_{\frac{\Phi}{2}}^{2\pi - \frac{\Phi}{2}} \max\left(\hat{\mathbf{s}}(\theta) \cdot \hat{\mathbf{n}}_i, 0\right) d\theta, \tag{24}$$

where:

- P is the total orbit average power generated,

- N is the number of solar panel surfaces,
- A_i is the area of the i-th solar panel surface,
- P_{AM0} is the solar irradiance at Air Mass Zero (AM0) given in Appendix A,
- η_{PV} is the photovoltaic conversion efficiency,
- Φ is the angular extent of the orbital eclipse period,
- $\hat{\mathbf{s}}(\theta)$ is the unit vector pointing towards the Sun as a function of the orbital angle θ,
- $\hat{\mathbf{n}}_i$ is the unit normal vector of the i-th panel surface,
- The max function ensures that only positive dot products contribute, modeling the cosine dependence of solar incidence while ignoring back-side illumination.

Table 4.10 summarizes the key parameters used with Equation 24 to estimate the power generation of the spacecraft. Initially, we consider the spacecraft configuration shown in Figure 4.3, where each large face of the spacecraft has eight solar cells. To establish a reference for all subsequent calculations, we first estimate the maximum power that this spacecraft configuration could generate. This maximum occurs when the edge between two large spacecraft faces is always oriented toward the Sun, as illustrated in Figure 4.2, which maximizes the exposed solar panel area. In this orientation, the orbit average power (OAP) is calculated as the product of the exposed solar panel area, photovoltaic conversion efficiency, incident solar irradiance, and the daylight fraction of the orbit, as expressed in Equation 25:

$$P = A \times \eta_{PV} \times P_{AM0} \times \left(1 - \frac{\Phi}{2\pi}\right), \tag{25}$$

where:

- P is the orbit average power generated,
- A is the area of the exposed solar panels,
- η_{PV} is the photovoltaic efficiency,
- P_{AM0} is the solar irradiance at Air Mass Zero (AM0),

- Φ is the angular extent of the eclipse portion of the orbit.

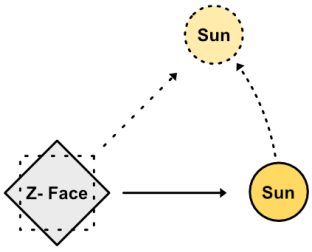

Figure 4.2: Stowed Sun Pointing Configuration

Using the values provided in Table 4.10 and Appendix A, the OAP as a function of the solar beta angle is plotted in Figure 4.4. Section 5.1 presents a more detailed model of the PV cells that these parameters were derived from. In this configuration, the worst-case power generation is approximately 5 W, which represents the absolute maximum achievable using only body-mounted panels. However, this pointing configuration does not optimally orient the payload or the TT&C antennas with respect to the ground. This maximum power is slightly more than the power required to operate the payload at its minimum duty cycle; before accounting for converter losses, confirming that a configuration based solely on body-mounted panels is not feasible for the mission.

Parameter	**Value**	**Notes**
A	20cm^2	Area per cell
η_{PV-BoL}	25.6 %	BoL efficiency @ 100 C
η_{PV-EoL}	22.1 %	EoL (1E14 cm^2) efficiency @ 100 C
h	520 km	Orbital Height

Table 4.10: Key Power Generation Model Parameters

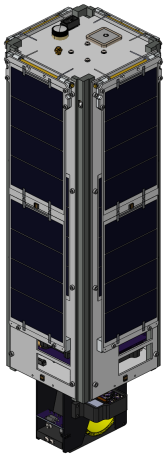

Figure 4.3: Stowed Configuration

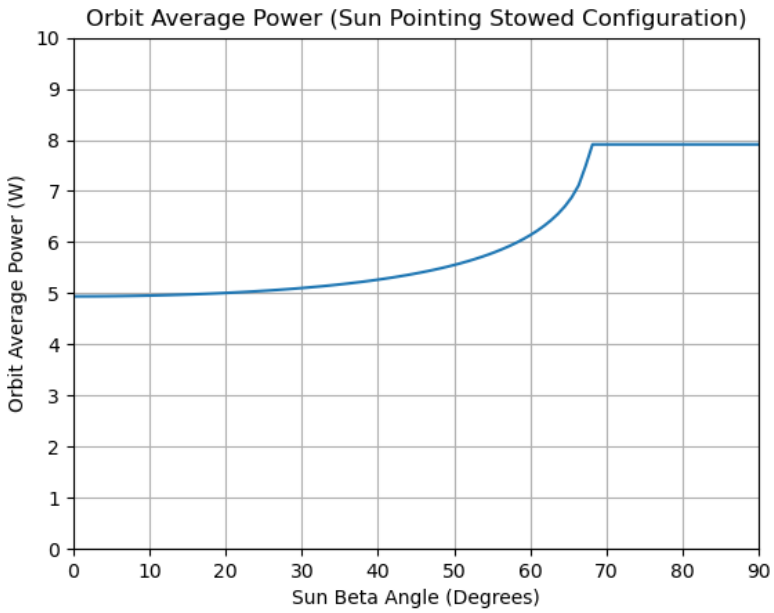

Figure 4.4: OAP vs Beta Angle for the Sun Pointing Stowed Configuration

The Sun-pointing configuration previously described is likely not a viable pointing mode in practice, as the Sun is not within the field of view (FoV) of the fine Sun sensor. Instead, the Y- or Z-axis Thompson spin modes are considered, as these are the required initial pointing states before transitioning to any other control modes. To simplify the power generation analysis in these spin configurations, we assume that the spacecraft's spin rate is much faster than the orbital period. This assumption allows us to replace the instantaneous solar panel area exposed to the Sun with the average cross-sectional area of the faces perpendicular to the orbit normal vector.

For a Y-axis Thompson spin, the X and Z faces are perpendicular to the axis of rotation, and their time-averaged projected area can be calculated using:

$$A_{avg} = \frac{1}{2\pi} \int_0^{2\pi} |A_x \hat{\mathbf{x}} \cos(\theta)| + |A_z \hat{\mathbf{z}} \sin(\theta)| \, d\theta, \tag{26}$$

where:

- A_{avg} is the average cross-sectional area of the X and Z faces,
- A_x and A_z are the areas of the X and Z faces respectively,
- θ is the rotation angle about the Y-axis,
- $\hat{\mathbf{x}}$ and $\hat{\mathbf{z}}$ are the unit vectors along the X and Z body axes.

Evaluating the integral in Equation 26 yields:

$$A_{avg} = \frac{2}{\pi}(A_x + A_z), \tag{27}$$

which provides the effective average area exposed to the Sun during a Y-axis spin. Note that the Z face does not have any solar cells on it, so in this case A_z is 0. A similar approach can be applied to the Z-axis Thompson spin, with corresponding face area substitutions.

Applying this method to Y and Z Thompson spins, yields Figure 4.5. Notice that Z-Thompson gives a higher power generation at low beta angles and Y-Thompson gives higher power generation at high beta angles. This is expected as the nadir and velocity directions are exposed to the majority of the sunlight at lower beta angles and the orbit normal

axis is exposed to the majority of the sunlight at higher beta angles. Finally, although the Z-Thompson spin does produce more power at the lower beta angles we are likely to encounter; it is undesirable as it results in the UHF antenna nulls frequently pointing towards the ground station, reducing TT&C reliability. For this reason, it will not be further considered. Plotting minimum and maximum power generation vs LTAN yields Figure 4.6, the power margin is computed assuming a 75% average efficiency and the lower power LEOPS operating mode.

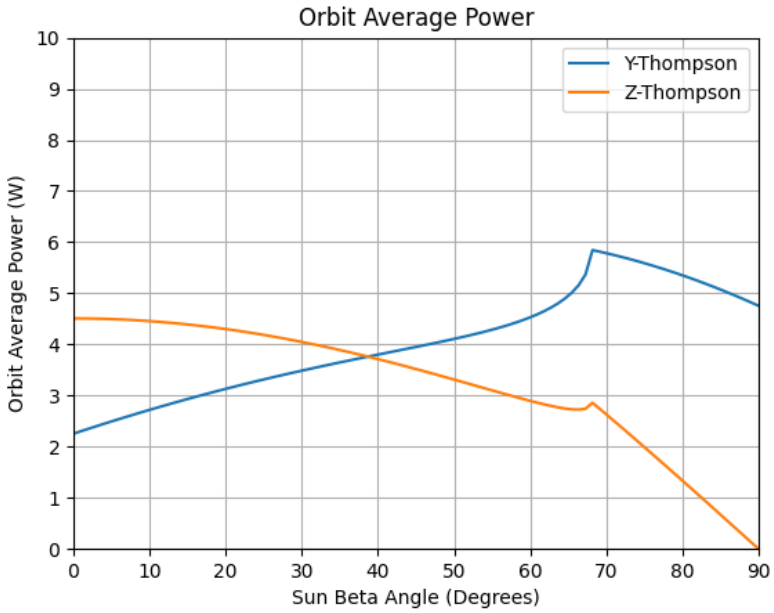

Figure 4.5: Y and Z Thompson Spin Power Generation (Stowed)

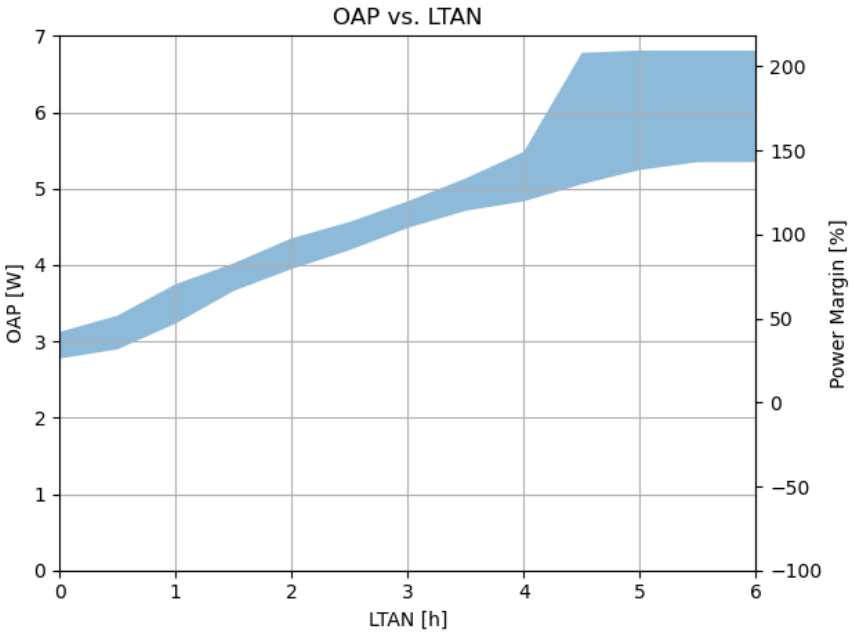

Figure 4.6: Y Thompson Power Generation vs LTAN (Stowed)

4.6 Deployed Array Energy Generation

This section focuses on estimating spacecraft power generation when the solar array has been fully deployed. Only nadir pointing configurations are considered, as it was found that sufficient power could be generated in this mode for payload operations. Additional power could be generated by transitioning to sun pointing modes when TT&C and the payload are not active (ex. when at high latitudes); however, it is unknown if the spacecraft will be able to reliably transition between modes due to the large moment of inertia and potential flexing of the HF during the rapid rotations needed to transition between pointing modes. For completeness, the sun pointing OAP is shown in Figure 4.7, note that this represents the maximum power generation capability of MARMOTSat, all other pointing modes are expected to produce less power than this.

The solar array configuration shown in Figure 1.3 was chosen early in the project; mainly to satisfy antenna and mechanical constraints. Other configurations were mechanically infeasible or resulted in the deployable solar array interfering with spacecraft antenna radiation patterns, and the preliminary power generation analysis indicated that this configuration would generate sufficient power for the spacecraft mission. The main design decision made for power generation purposes was the exact angle at which to deploy the solar pan-

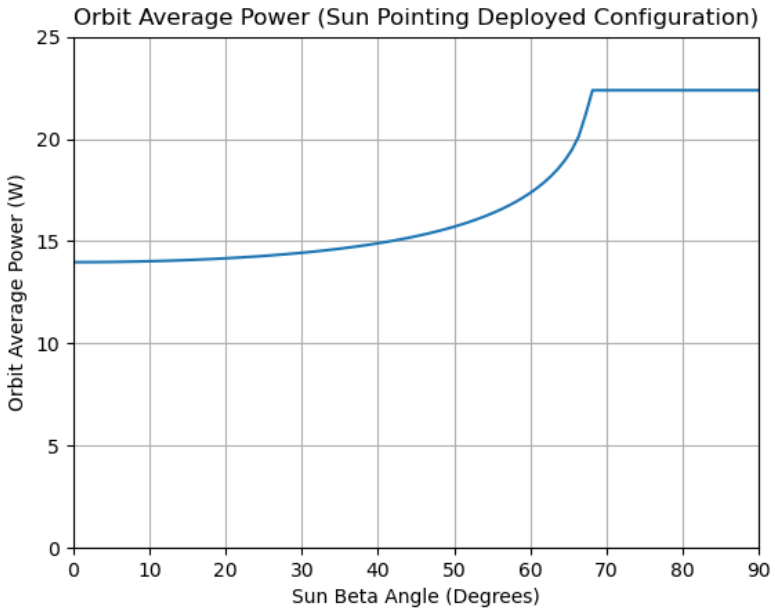

Figure 4.7: Sun Pointing OAP for Deployed Solar Array

els. Figure 4.8 demonstrates how the deployment angle is measured for the remainder of this section. A 0° angle corresponds to the ”default” configuration shown in Figure 1.3 and positive angles are angles that result in the panel being deployed at a larger angle relative to the stowed position.

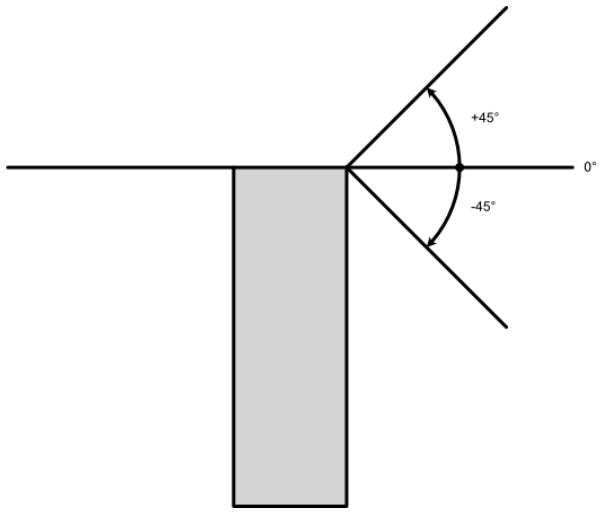

Figure 4.8: Array Deployment Angle Sign Conventions

Estimating the power generation for the solar array deployed is slightly more complicated than for the stowed configuration. Equation 24 cannot be used as deployable panels can

shade body-mounted panels, so a more sophisticated model is needed. STK provides a model that takes shading into account when simulating power generation; however, it is relatively slow and clumsy to use when exploring a large design space covering a wide variety of orbits and solar array configurations. To speed up analysis, a simple tool for estimating the OAP was developed that accounts for the shading caused by the spacecraft geometry. This tool works in much the same way as STK's built-in solar panel tool; it renders the spacecraft model with the solar cells rendered a specific color and then counts the number of colored pixels in the image. This approach leverages the OpenGL graphics library, which allows for a relatively simple implementation. The results generated using this tool are then compared with the STK results to validate the simulations.

The OpenGL based solar model allows the analysis of alternative nadir-pointing attitudes by applying a static rotation matrix to the spacecraft geometry. For each orbital time step, the sun vector is computed using the methods described previously, providing the illumination direction in the spacecraft frame. A rotation matrix is then computed to align the spacecraft Z-axis (zenith direction) with the sun vector, transforming the geometry so that the solar panels can be evaluated under direct illumination within the rendered frame.

Using an orthographic projection, the transformed spacecraft geometry is rendered from the Sun's perspective, producing the map of illuminated solar panel surfaces shown in Figure 4.9. The area corresponding to each pixel is calculated from the projection window size and image resolution, and the number of red-tagged pixels is counted to determine the effective illuminated area at each time step. By scaling this illuminated area with the incident solar flux, the instantaneous power generation is computed systematically across the orbit. This process is repeated across the entire circular orbit to compute the OAP for the specified configuration.

To perform a quick "sanity check" on the output of our model, we will perform a simulation of the power generation for a single orbit with a $90°$ solar beta angle with the panels deployed to $0°$, as we can trivially calculate the expected output. A $90°$ beta angle will not have an eclipse and the Sun will always be perpendicular to the X+ face, so the OAP will simply be the nominal AM0 output power of a single 4S string. Figure 4.10 plots the simu-

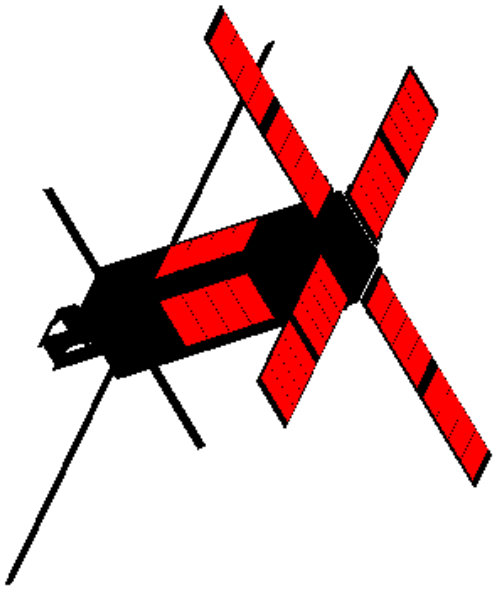

Figure 4.9: OpenGL Rendering of the Spacecraft

lated power for a single orbit; as expected, we can see that it is constant. The exact value output by the simulator was a 2.9W OAP; this is slightly higher than the expected 2.78W based on the PV cell parameters presented. This discrepancy is due to the PV cells used in the model having an area slightly larger than the 20cm^2 area of actual PV cells. The model is based on the physical dimension of the PV cells, which have a small border around the active portion of the cell. This could be compensated for by adjusting the model; however, since the power generation is directly proportional to the PV area we will simply scale all power generation by a factor of 0.959 to compensate for the slightly larger PV cells as this allows for our model to easily be kept in sync with the mechanical model of the spacecraft. After applying this correction factor to the model, the results match the expected output. Next, the output of the model was compared to the output obtained from STK for a 45° beta angle. After accounting for reduced solar flux due to the STK simulation being run near aphelion, the OpenGL-based model demonstrated close agreement with STK, validating the

geometric projection and power calculation pipeline. Figure 4.11 shows the simulated power generation over a single orbit generated using both models. Note that no correction factor was used for this simulation so that the results of the developed model and STK match.

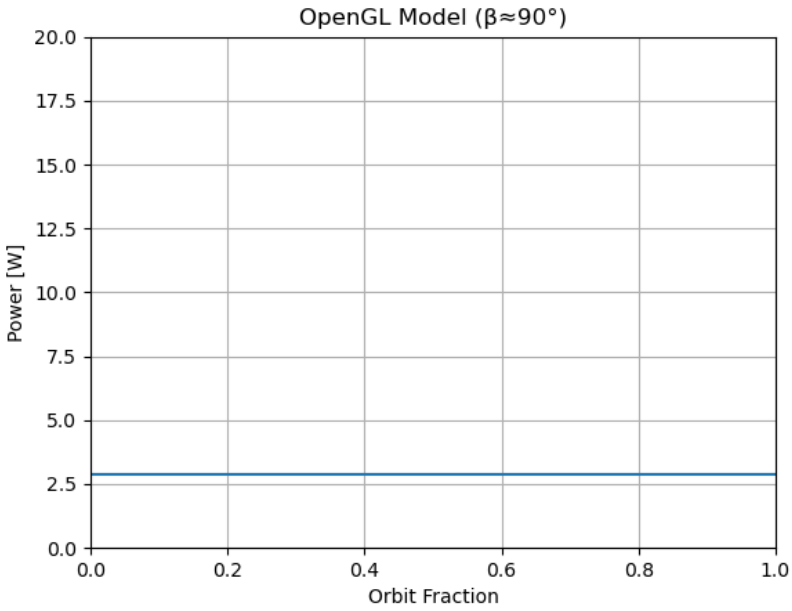

Figure 4.10: 90° Solar Beta Angle Check

Effect of Deployment Angles A symmetry in power generation versus the deployment angle of the Y+ and Y– panels with respect to the solar beta angle is expected. This arises from the geometry of the apparent motion of the Sun relative to the spacecraft. Specifically, when the solar beta angle changes sign, the apparent path of the Sun across the spacecraft mirrors across the orbital plane. Likewise, if the spacecraft is rotated 180 degrees about the nadir axis, the orientation of the Y axis panels relative to the Sun also mirrors. This implies that the Y+ panel at a positive beta angle should experience illumination conditions identical to those of the Y– panel at the corresponding negative beta angle; in other words, the results are mirrored about $\beta = 0$. Figure 4.12 demonstrates that this relationship is reflected in the results produced by our model, verifying that this geometric reasoning is consistent with the simulated power generation behavior.

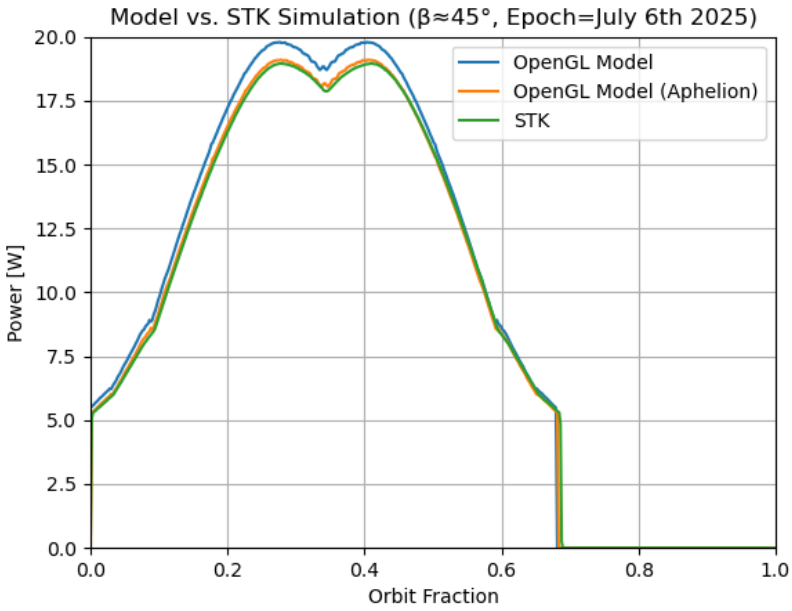

Figure 4.11: OpenGL Model and STK Single Orbit Power Generation

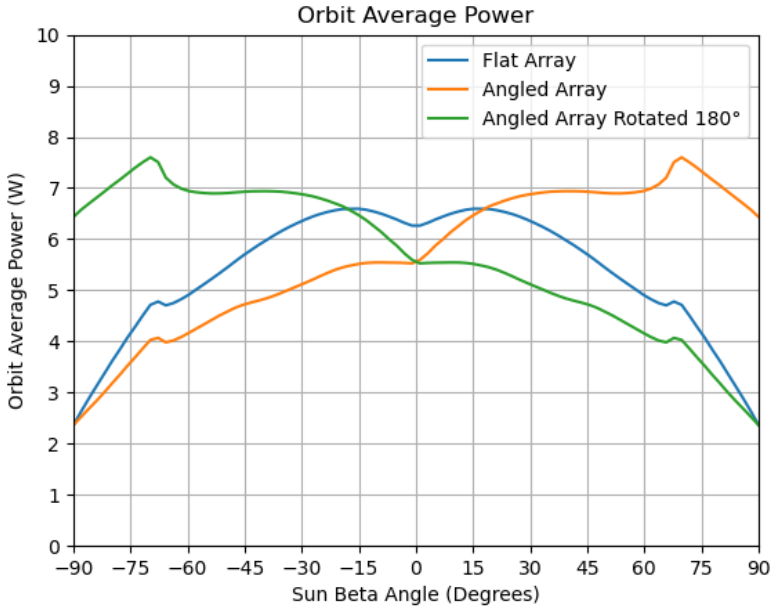

Figure 4.12: Symmetry of the Y+ and Y+ Panel Deployment Angles for Y- deployed to $+60^\circ$

Figure 4.13 shows how power generation varies as a function of the deployment angle and the solar beta angle, while Figure 4.14 presents the optimal deployment angle versus the beta angle. Note that the deployment angles were computed in 10° increments, leading to the stepped appearance in the figure. It can be seen that the optimal deployment angle

generally increases with increasing beta angle. At $|\beta| = 90°$, the Sun remains on one side of the spacecraft throughout the orbit, so we expect the panel to be deployed to approximately $\pm 90°$, with the sign determined by the sign of the beta angle and the side of the spacecraft on which the panel is mounted. In contrast, at $\beta = 0°$, the Sun moves directly overhead, and a deployment angle of $0°$ should maximize power generation. This is consistent with the results shown in Figure 4.14. Figure 4.15 combines these results with the solar beta angle vs. the previously generated SSO LTAN plot to plot the minimum deployment angle that maximizes the minimum OAP for each LTAN. This figure shows roughly the results we would expect; LTANs near dawn/dusk have higher deployment angles near $\pm 90°$ and LTANs near noon/midnight have deployment angles near $0°$.

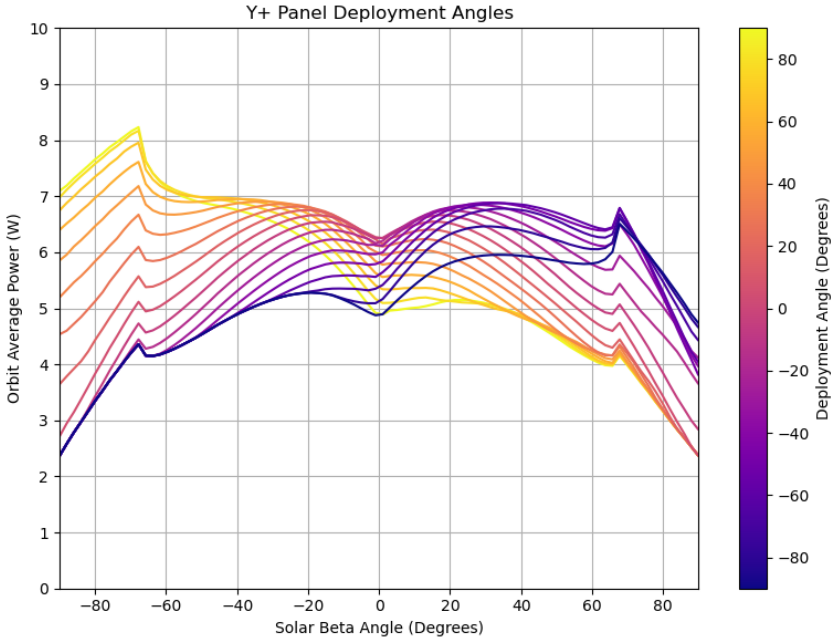

Figure 4.13: OAP vs. Y Panel Deployment Angle

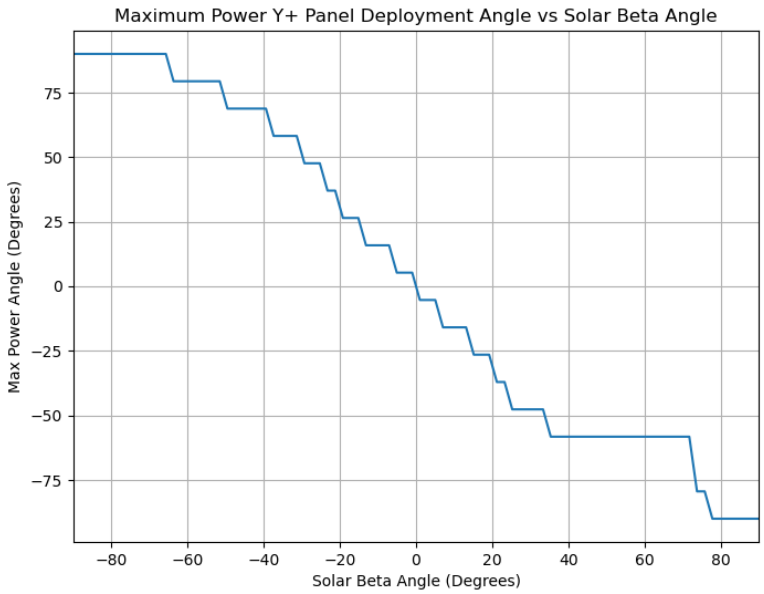

Figure 4.14: Optimal Y Panel Deployment Angle vs Solar Beta Angle

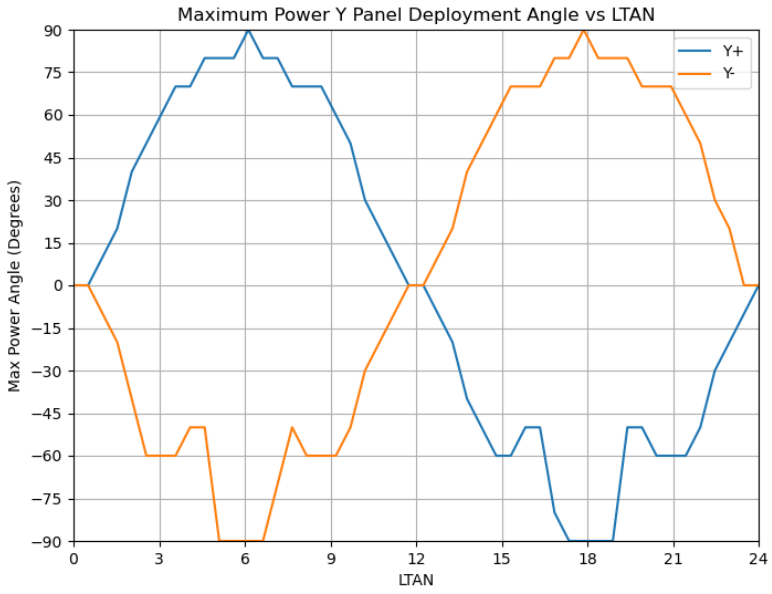

Figure 4.15: Y Panel Deployment Angles that Maximize Minimum OAP vs LTAN

This procedure was also applied to the X+ and X− panels, with results shown in Figure 4.16. The analysis indicates that deploying these panels to angles other than 0° does not significantly improve power generation. This outcome is expected because the apparent motion of the Sun, as the beta angle varies, occurs primarily along the Y-axis. Consequently,

rotating the X+ and X− panels about the Y-axis does not effectively align them with the Sun's trajectory, unlike the Y+ and Y− panels.

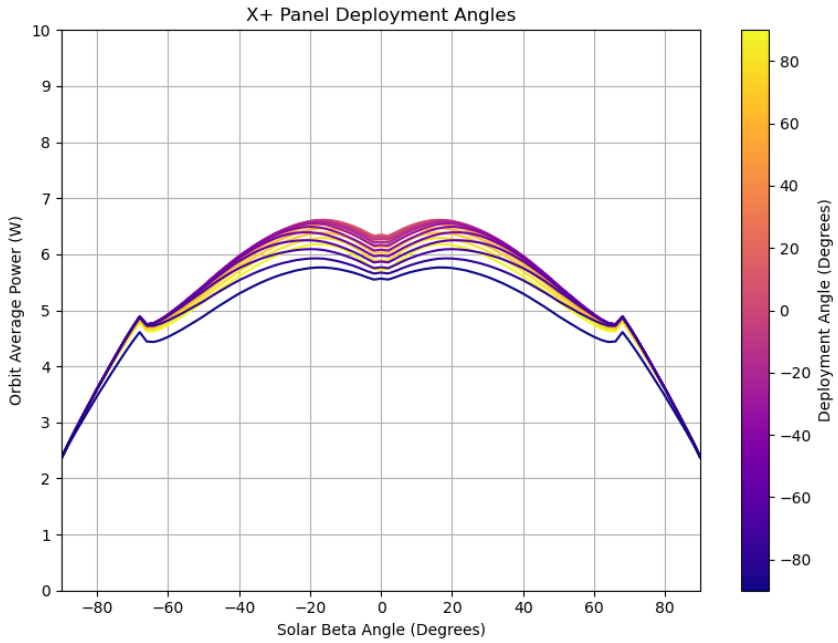

Figure 4.16: OAP vs X Panel Deployment Angle

Figure 4.15 shows that the optimal solar array deployment angle, that maximizes the minimum OAP encountered, changes rapidly with LTAN, particularly for LTANs near noon or midnight, which are the most likely deployment windows for MARMOTSat. As a result, we cannot fully optimize power generation without knowing the exact LTAN in advance, so we must design for the worst-case scenario. From Figure 4.13, we observe that for the Y− panel, increasing the beta angle generally increases power generation when the deployment angle is greater than $0°$. Similarly, for the Y+ panel, increasing the beta angle improves power generation when the deployment angle is less than $0°$. This behavior implies that the worst-case deployment angles correspond to the LTAN closest to noon or midnight, where the minimum beta angles occur and power generation is at its lowest.

Based on the data in Figure 4.14 and summarized in Table 4.11, the deployment angles that maximize the minimum power generation across all expected LTANs are Y+ = $\pm 10°$ and Y− = $\mp 10°$. Figure 4.17 compares the minimum and maximum yearly orbit average power (OAP) versus LTAN for several configurations: the "optimal" $\pm 10°$ array, a baseline $0°$ array, and two more aggressive configurations where the Y+ panel is deployed to $40°$ or

$60°$ and the Y$-$ panel to $-20°$. LTANs are plotted from 0 to 6 hours since the spacecraft's symmetry allows inference of power generation for the full 24-hour range. The negative deployment angle is limited to $-20°$ to avoid interference with the spacecraft's antenna patterns.

The comparison reveals that while the "optimal" configuration maximizes minimum power generation around the 1h LTAN, the $40°/-20°$ configuration yields only slightly lower minimum OAP but substantially higher power generation for LTANs further from noon or midnight. The most aggressive $60°/-20°$ configuration results in significantly reduced power near the 1h LTAN, with only marginal gains compared to the $40°/-20°$ setup. Due to this, the $40°/-20°$ configuration is recommended.

LTAN (h)	Y- Angle (deg)	Y+ Angle (deg)
0	0	0
1	-10	10
2	-40	40
3	-60	60
4	-50	70
5	-80	80
6	-90	90
7	-80	80
8	-50	70
9	-60	60
10	-40	40
11	-10	10
12	0	0
13	10	-10
14	40	-50
15	60	-60
16	70	-50
17	80	-90
18	90	-90
19	80	-90
20	70	-50
21	60	-60
22	40	-40
23	20	-20
24	0	0

Table 4.11: LTAN vs Y- and Y+ Panel Angles

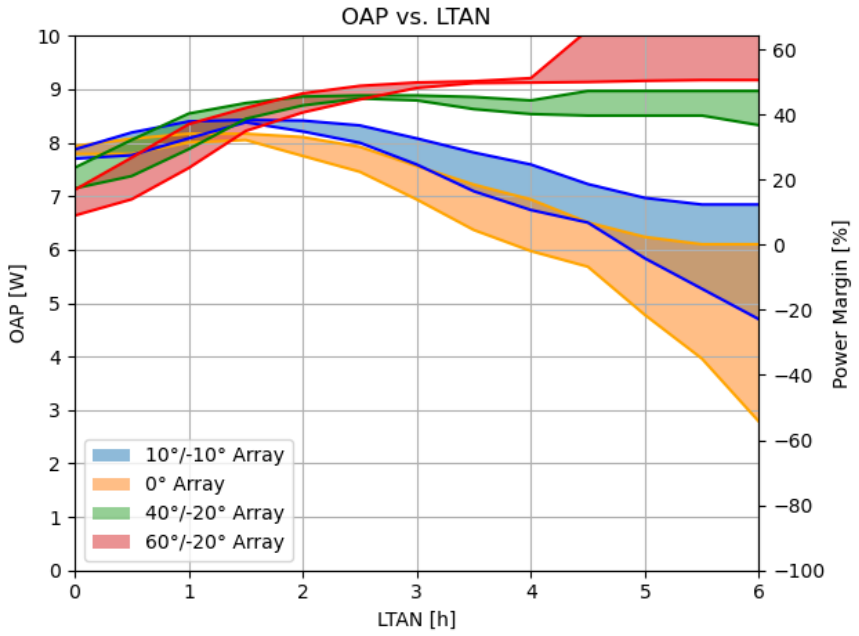

Figure 4.17: Flight Configuration OAP

4.7 End of Life Energy Generation

As the spacecraft orbit decays, the drag on the HF antenna will increase due to the increasing atmospheric density. The ADCS team determined that this will overwhelm the ADCS's ability to dump momentum via its magnetoqurers. When this occurs, the spacecraft will be forced into an attitude with the small face facing in the direction of travel (Ram). This still leaves the spacecraft free to rotate along the velocity vector (spacecraft Z axis). Power generation could be optimized by utilizing the ADCS's partial Sun tracking mode, which would allow the spacecraft to partially track the Sun by rotating along the Z axis; however, as the fine Sun sensor is often unable to see the Sun in this configuration it should not be relied upon and will not be further considered. Figure 4.18 shows the OAP for the selected $40°/-20°$ solar array configuration and the $0°$ configuration, accounting for the estimated PV cell deration due to radiation. Note that the OAP power is significantly lower in this mode than in nominal mode; however, this is acceptable because the spacecraft will be near the end of its life when this mode is entered, so a degree of degradation is acceptable. Lastly, we note that the actual deration of the PV cell under long-term exposure to the LEO envi-

ronment is unknown and may be significantly higher than estimated due to degradation in the optical properties of the FEP top-sheet. This is acceptable, as the spacecraft is experimental and can operate in very low power modes if needed, so it is likely that at a minimum housekeeping telemetry can be collected for the whole mission life.

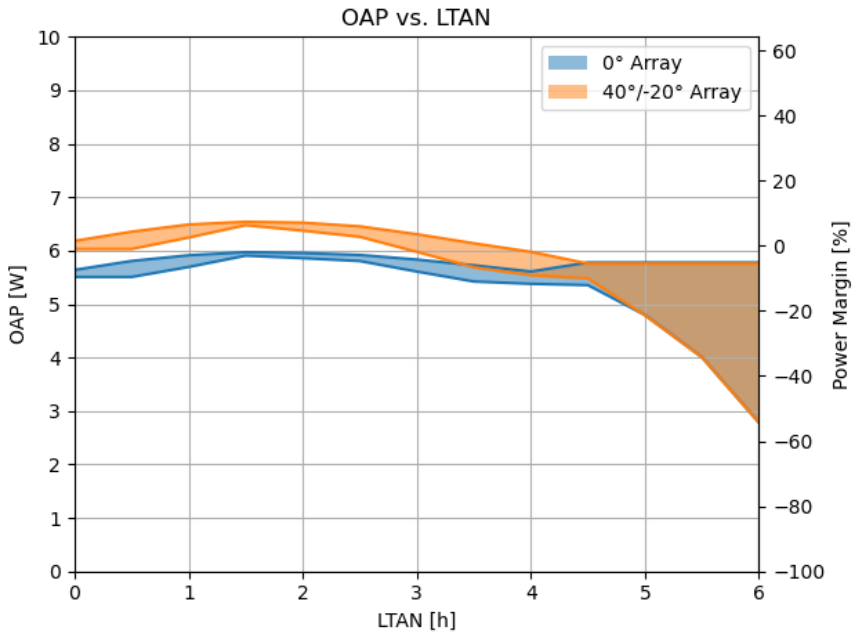

Figure 4.18: EoL Configuration OAP

4.8 Battery Usage

Figures 4.19 and 4.20 show the average, minimum and maximum battery depth of discharge (DoD) expected to be encountered over the MARMOTSat mission. The minimum and maximum DoD are computed considering different payload operations periods (eclipse and daylight) as well as over all beta angles encounters for the given LTAN. The mean values assume a random payload activation period, i.e. one that is uniformly distributed over the orbit, and account for the varying beta angles over the course of the year. We can see the expected pattern of higher average and maximum DoDs at lower LTANs due to the longer eclipse periods. A quick sanity check on the results shown here can be performed by referring back to Figure 4.17, we can see that the OAP for the chosen PV array configuration is approximately 7.5W maximum for dawn/dusk orbits and we know from previous analysis that this power generation will be relatively constant over the whole orbit due to the

lack of an eclipse period at high beta angles. The orbital period is approximately 94 minutes, so a payload activation period of 10% corresponds to 9.4 minutes and the payload will draw approximately 18W during this period. This will discharge (18-7.5V)×9.4 minutes=99 Wmin=1.6 Wh, this roughly lines up with what is shown in Figure 4.19. The power varies slightly over the course of the orbit, as the maximum power beta angle is not 90° (Figure 4.13), so the actual minimum DoD is slightly lower as the PV array will be generating more than the OAP during the best case payload operation period. This is also reflected in the results shown in Figure 4.19, so the results of this analysis appear to be reasonable.

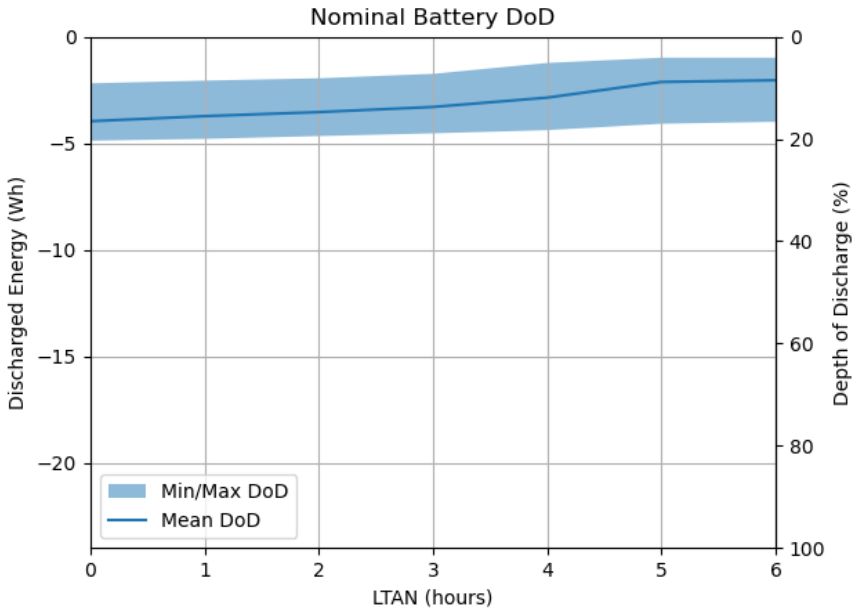

Figure 4.19: Nominal Attitude DoD vs LTAN (10% Payload Duty Cycle)

From Figure 4.19, we can see that the maximum DoD is expected to be around 20% with the average around 15%. This is slightly high; however, the longer lifespans of the LTO cells mean that they can be cycled harder than traditional LCO cells. For a 5 year mission, a 20% DoD per orbit corresponds to roughly 6000 equivalent full cycles; this is around the 7000 cycles to 70% capacity lifetime reported by the manufacturer [38]. As the spacecraft can remain operational even with $> 50\%$ capacity degradation, it seems likely that the capacity degradation due to cycling over the mission will be manageable.

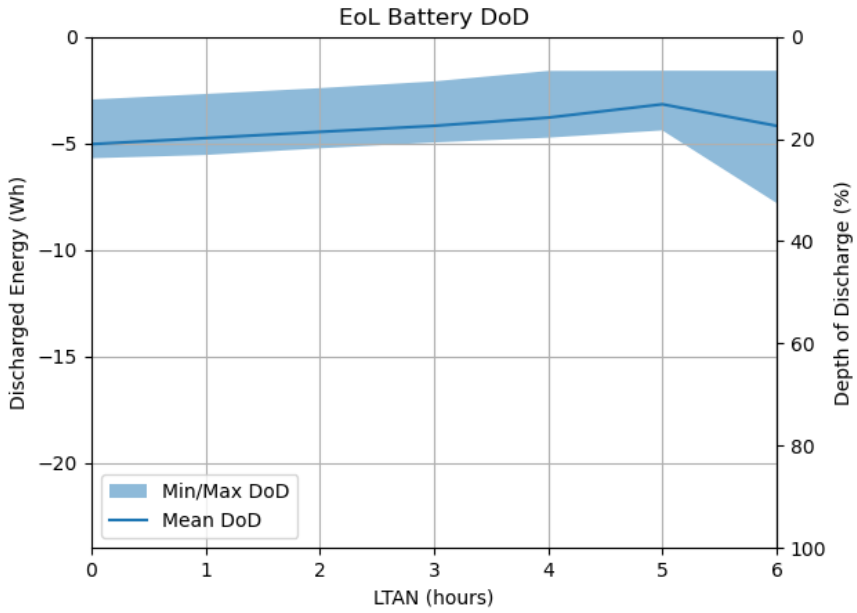

Figure 4.20: EoL Attitude DoD vs LTAN (10% Payload Duty Cycle)

4.9 Limitations of Power Generation Modeling

While the power generation modeling performed in this work provides a solid basis for system-level EPS sizing and mission feasibility analysis, several limitations should be acknowledged:

- **Deviation from the Cosine Law**: The analysis assumes that incident solar power on photovoltaic (PV) cells strictly follows a cosine dependence on the angle of incidence. In practice, PV cell generation deviates from this ideal due to surface reflections, especially at higher incidence angles, which can reduce effective power generation compared to the ideal cosine model.

- **String-Level Voltage Tracking and Shading Effects**: The current EPS design tracks the entire solar array to a single voltage using a centralized maximum power point tracking (MPPT) implementation. As a result, shading on even a small portion of a PV cell within a series-connected string can significantly reduce the power output of the entire string, as the current is limited by the most shaded cell. Consequently, power output is not directly proportional to the unshaded PV area, and partial shading can lead to disproportionate losses that are not fully captured in the idealized power generation model used in this analysis.

- **Assumed Constant AM0 Illumination**: The modeling assumes a constant Air Mass Zero (AM0) solar irradiance of 1361 W/m^2 throughout the orbit and over the mission duration. In practice, solar irradiance varies slightly over the course of the year due to the elliptical nature of Earth's orbit, being marginally lower during aphelion and higher during perihelion. While this variation is small, it introduces minor discrepancies between the modeled and actual power generation capabilities of the spacecraft over its operational lifetime.

These limitations should be considered when interpreting power budget margins, particularly in worst-case mission scenarios with low illumination conditions and potential partial shading events.

4.10 Power Budget Summary

It is difficult to design a spacecraft for an unknown orbit, particularly if the spacecraft is nadir pointing, as the power generation of the spacecraft is highly dependent on both the geometry of the orbit and the placement and geometry of the spacecraft solar array. Based on past SpaceX transporter launches it was estimated that the MARMTOSat LTAN will most likely be 1 to 3 hours away from a noon/midnight orbit, so the PV array placement focuses on maximizing power generation for this range of LTANs. During nominal operations, with a 10% payload duty cycled, the spacecraft is expected to have a power margin $> 30\%$ for all likely launch LTANs, with the maximum battery DoD of approximately 20%. During LEOPS, before the main solar array has been deployed, the spacecraft generates significantly less power and will need to rely on magnetorquer only control modes, such as Y-Thompson. For this low power mode, the power margin is $> 50\%$ for the most likely LTANs. Lastly, as MARMOTSats orbit decays the atmospheric drag on the deployed HF antenna will force the spacecraft into a lower power generation attitude. At this attitude, the power budget is barely positive with less than a 10% margin for the BoL PV cell power generation and bus power consumption. It is expected that PV cell generation will degrade due to environmental effects, including radiation, and that the bus power usage will increase due to TID degradation of the on board electronics. Based on this it is very likely that the spacecraft will not be able to conduct regular payload operations near the end of its life; however, the spacecraft's lowest power operating mode consumes 7 times less power

than the nominal mode, so the spacecraft will generate sufficient power to maintain basic housekeeping functions until the spacecraft reenters the Earth's atmosphere.

5 System Design

This section presents the detailed design of the MARMOTSat Electrical Power System (EPS), responsible for generating, storing, regulating, and distributing electrical power to all spacecraft subsystems. The EPS ensures continuous operation throughout all mission phases while adhering to deployment constraints and launch provider requirements. The EPS architecture is composed of the following core functional elements also shown in Figure 5.1:

- **Power Generation**: Power is generated by a combination of body-mounted and deployable solar panels equipped with triple-junction GaAs cells.
- **Energy Storage**: Electrical energy is stored in a lithium titanate (LTO) battery pack, chosen for its high cycle life and ability to safely charge at sub-zero temperatures without active thermal management.
- **Power Conditioning and Distribution Module (PCDM)**: The PCDM serves as the central component of the EPS, integrating several key functions:
  - **Battery Charge Regulation (BCR)**: Implements maximum power point tracking (MPPT) to optimize power extraction from the solar arrays while safely managing battery charging.
  - **Power Regulation and Distribution**: Provides multiple regulated voltage rails and distributes power via protected output channels tailored to subsystem requirements.
  - **Power Control Unit (PCU)**: Implements the required inhibit logic to ensure the spacecraft remains powered off while in the deployer, and safely powers on only after deployment, in accordance with SpaceX Rideshare requirements. Also includes a hardware-based heartbeat mechanism that allows the OBC to reset the spacecraft by cycling power if the heartbeat signal is not periodically refreshed.
- **Command and Telemetry Interface**: The PCDM includes GPIO-based control lines from the OBC to enable or disable individual power channels in flight. Additionally, a dedicated telemetry interface provides continuous monitoring of voltage, current, and temperature across all EPS channels, supporting real-time health diagnostics and fault detection.

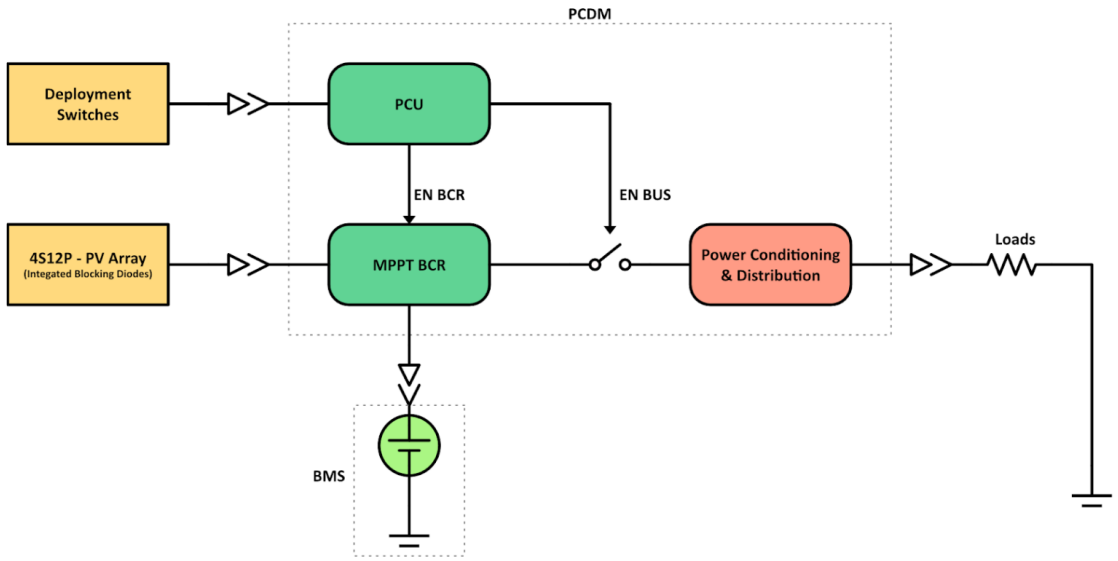

Figure 5.1: EPS Top Level Block Diagram

The following sections detail the design, implementation, and testing of each component of the EPS, supported by analysis that verifies compliance with mission requirements and operational constraints.

5.1 Solar Cells

MARMOTSat uses 4S12P arrays of flexible triple junction GaAs solar cells produced by Microlink Devices that can be seen in Figure 5.2. These cells come pre-assembled in the 4S arrays backed with a pressure sensitive silicone adhesive and pure silver electrical interconnects and are primarily targeted at high altitude UAVs [39]. The primary reason for choosing these cells for more traditional CICs was for their slightly lower cost and much lower lead times, as the lead times for most conventional CIC cells from large manufacturers were more than the duration of the MARMOTSat project. Instead of the cover glass on traditional CIC cells, these cells have a flexible polymer-based (FEP) top sheet. The ability of this top sheet to shield the cells from radiation and its susceptibility to atomic oxygen degradation are relatively unknown. Some data on FEP based top sheets in the LEO environment is available from an experiment performed aboard the Long Duration Exposure Facility (LDEF) shown in Figure 5.3, a facility that was placed in LEO in 1984 and recovered by the Space Shuttle Columbia in 1990 to study the effects of the LEO environment

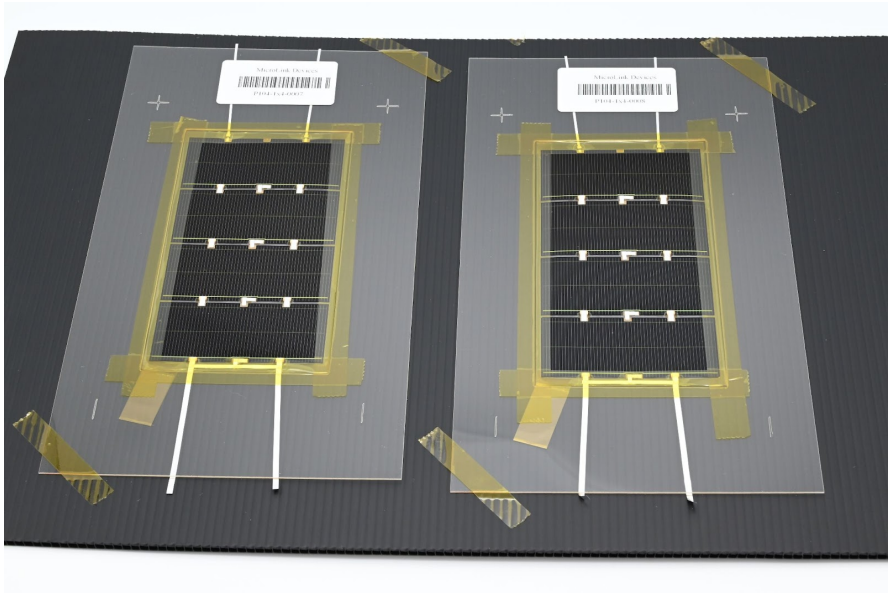

Figure 5.2: The Microlink PV Array

on a variety of different materials [40]. The JPL SAMPLE (Solar-Array Materials Passive LDEF Experiment), included solar cells with similar FEP based top-sheets to those used on the Microlink Devices solar cells. The result of the experiment was that the FEP based top sheets continued to protect the cells from atomic oxygen; however, they suffered an 8% greater degradation of the optical properties of the cover glass than traditional cover glass materials over the 6 year mission [41]. Furthermore, some radiation test data was provided by Microlink Devices; however, it is less extensive than that provided by typical solar cells. This provides some confidence that the solar cells will continue to function for the course of the mission; albeit, with a higher degree of degradation than would be present in traditional space-grade CIC cells.

In order to design the solar power regulation system for MARMOTSat, it is necessary to understand the current-voltage (IV) characteristics of the solar cells that comprise the spacecraft's solar array. These characteristics define the range of input voltages and currents that the regulator system must be capable of handling. The analytical model developed by [42] is used to estimate the IV curve of solar cells under varying operating conditions, based on manufacturer-provided specifications. This model is given by Equations 28–31. Changes in voltage due to variations in illumination are neglected, as these effects are generally small [43] and specific data is not available from the manufacturer. Note that this equation

Figure 5.3: The Long Duration Exposure Facility [40]

is in the same form as Equation 14; however, the parameters are derived from datasheet values rather than physical constants. The key result of this equation is that the open circuit voltage, maximum power point voltage and maximum power all decreases as temperature increases. This can more clearly be seen by plotting the equation for several values as shown in Figure 5.4, then by directly inspecting the equation.

$$J = \alpha \cdot J_{max} \cdot \tau_i - \alpha \cdot J_{max} \cdot \exp\left(\frac{V}{b \cdot (\gamma \cdot \alpha + 1 - \gamma) \cdot (V_{oc} + \tau_V)} - \frac{1}{b}\right), \tag{28}$$

$$\gamma = 1 - \frac{V_{oc}}{V_{oc} - \tau_V}, \tag{29}$$

$$\tau_V = TCV \cdot (T - T_N), \tag{30}$$

$$\tau_i = 1 + TCi \cdot (T - T_N), \tag{31}$$

where:

- J is the current density output of the solar cell,
- V is the voltage across the solar cell,
- α is the relative solar irradiance intensity (normalized between 0 and 1 with respect

to the reference level),

- J_{max} is the ideal maximum current density,
- b is the characteristic IV curve constant,
- V_{oc} is the open-circuit voltage at the reference irradiance level,
- γ is a correction factor accounting for temperature-dependent voltage shifts,
- τ_V is the voltage temperature correction term,
- TCV is the voltage temperature coefficient,
- T is the operating temperature of the solar cell,
- T_N is the reference temperature,
- τ_i is the current temperature correction factor,
- TCi is the current temperature coefficient.

The electrical parameters for the Microlink Devices cells are not publicly available and only provided to customers under a NDA; example parameters from similar cells provided by Spectrolab [12] will be used to replace non publicly available parameters for demonstration purposes. These parameters are summarized below in Table 5.1. Note that the J_{mp} parameter has been scaled to match the publicly stated 29% AM0 efficiency stated by Microlink Devices. The parameter I_{sc} has also been scaled by the same factor. Solving Equations 32 and 33, yields the I_{max} and b model parameters shown in Table 5.2.

TCV	$-5.6\frac{\text{mV}}{\text{K}}$
TCi	$0.059\frac{\%}{\text{K}}$
T_N	300K
V_{OC}	2.75V
V_{mp}	2.435V
I_{sc}	372mA
I_{mp}	358mA

Table 5.1: Manufacture Provided PV Parameters

$$I_{max} = \frac{I_{SC}}{1 - \exp\left(-\frac{1}{b}\right)} \tag{32}$$

$$I_{mp} = \frac{I_{SC}}{1 - \exp\left(-\frac{1}{b}\right)} \left(1 - \exp\left(\frac{V_{mp}}{b \cdot V_{OC}} - \frac{1}{b}\right)\right) \tag{33}$$

b	0.0349
I_{max}	0.358mA

Table 5.2: PV Model Parameters

Figure 5.4 shows Equation 28 plotted over voltage for several different values of solar panel temperature. Note that the V_{mp} voltage ranges from approximately 2 to 2.7 V per cell. For the 4S string used in MARMOTSat, this gives a total array voltage ranging from 8-10.8V.

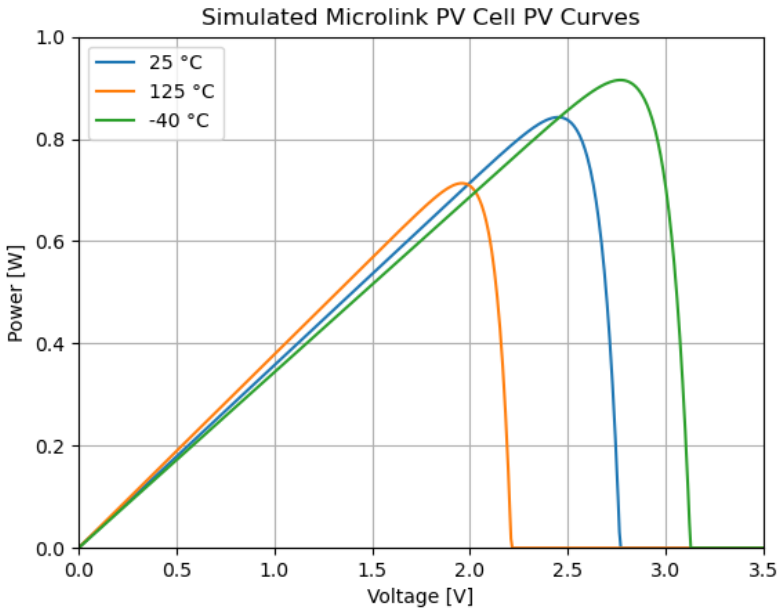

Figure 5.4: Modeled IV Curves for MARMOTSat Solar Cells

5.2 LTO Battery Characteristics

MARMOTSat utilizes the same Hunan Huahui New Energy lithium titanate oxide (LTO) cells used for the ORCASat mission, originally designed by Alexander Doknjas. The primary advantage of these cells over traditional lithium cobalt oxide (LCO) cells used by many

CubeSats is a much wider operating temperature, allowing them to be charged down to -30 ℃ with no damage to the cell. This allows for fully passive battery thermal control, removing the need for battery heaters present on most CubeSat battery packs. Additionally, the chosen LTO cells have over 6 times the lifespan of similar LCO cells, meaning their capacity will degrade much slower throughout the mission; however, this advantage is largely offset by their much lower BoL capacity. A comparison between the selected LTO cell and an equivalent LCO cell is shown in Table 5.3. While LTO cells do offer some advantages for the MARMOTSat mission, they were primarily chosen to build on the ORCASat heritage; a more traditional LCO battery pack with a resistive heater would have also been a viable solution, with the advantage of significantly increased BoL battery capacity.

	LTO 18650 [38]	**LCO 18650** [44]
Energy per Cell	3.12 Wh	11.7 Wh
Nominal Voltage	2.4 V	3.6 V
Charge Operating Temperature	-30-60 ℃	+10-45 ℃
Discharge Operating Temperature	-40-70 ℃	-20-60 ℃
Standard Charge Current	1.3 A	1.625 A
Max Discharge Current	13 A	6.5 A
Lifetime	3000 (85% Capacity)	500 (80% capacity)

Table 5.3: Comparison of LTO and LCO 18650 Cells

The minimum and maximum operating voltages, as well as the charge and discharge currents, are the main cell parameters of interest when designing the EPS. Figure 5.5 shows the discharge curves for the chosen cells; notice that for most temperatures less than 10% of the capacity remains after the cell has been discharged down to 2 V. For this reason, the minimum battery voltage has been derated from 1.5 V to 2 V. This serves two purposes: to ensure the batteries do not become too deeply discharged and to simplify the EPS design by raising the minimum battery voltage the EPS has to operate under. Additionally, the maximum battery voltage has been de-rated from 2.85 V down to 2.75 V to prolong battery life [45]. Figure 5.6 shows the cycle life characteristics of the chosen LTO cells.

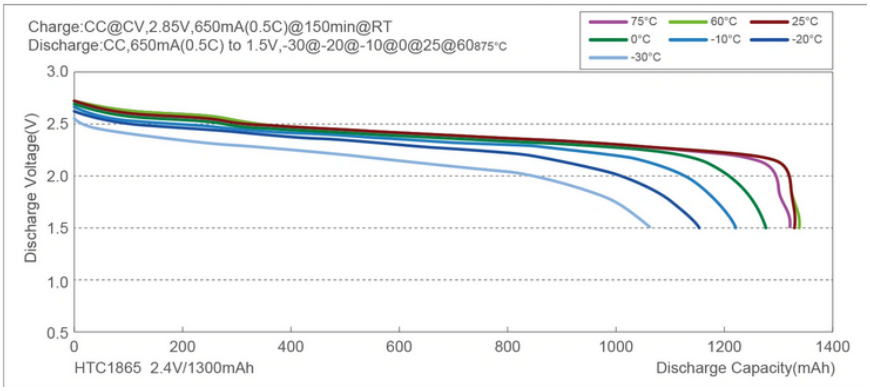

Figure 5.5: Manufacture Provided HTC1865 LTO Battery Discharge Curve [38]

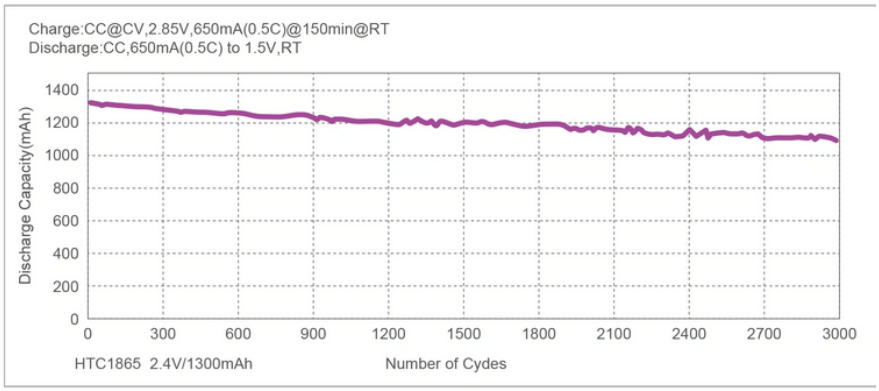

Cycle life	0.5C1 cycle	300 cycles	600 cycles	900 cycles	1200 cycles	1500 cycles	1800 cycles	2100 cycles	2400 cycles	2700 cycles	3000 cycles
(mAh)	1317.7	1317.7	1261.1	1236.6	1202.4	1194.6	1190.8	1158.7	1145.9	1136.6	1123.2
(%)	100.0%	97.5%	95.7%	93.8%	91.2%	90.7%	90.4%	87.9%	87.0%	86.3%	85.2%

Figure 5.6: Manufacture Provided HTC1865 LTO Battery Lifetime Characteristics [38]

5.3 Architecture

There are three key decisions when structuring a CubeSat EPS: how to regulate solar panel voltage, whether to regulate the bus voltage or use the raw battery voltage, and where to regulate the bus voltage to the required voltage for each subsystem.

5.3.1 Solar Panel Voltage Regulation

Direct Energy Transfer (DET), Peak Power Tracking (PPT), and Maximum Power Point Tracking (MPPT) are common solar array regulation strategies used in spacecraft power systems. A DET system connects the solar arrays directly to the battery bus via blocking diodes, possibly with a shunt or linear regulator to prevent the PV array voltage from exceeding the maximum battery voltage [37]. PPT and MPPT, by contrast, regulate the solar

array voltage to either a fixed peak point or continuously track the true maximum power point, respectively. DET is the simplest to implement but suffers from higher losses, while MPPT offers the highest efficiency with increased system complexity[4].

Direct Energy Transfer The main drawback of DET is that the solar array voltage follows the battery voltage, which varies with the battery's state of charge. While this approach is simple, reliable, and requires minimal components, it can be inefficient since the battery voltage rarely aligns with the maximum power point (MPP) of the solar array. Additionally, if the solar array's open-circuit voltage drops below the battery voltage, power generation ceases entirely. Elevated temperatures and radiation exposure can lower the open-circuit voltage of solar cells [12], exacerbating this issue.

Figure 5.7 plots PV cell IV curves with overlaid battery voltages. For the considered configurations, the 1S and 2S battery configurations severely limit power generation, while the 4S configuration risks preventing battery charging entirely under high-temperature conditions. The 3S option seems very promising; however, a 3S pack cannot be made with 8 cells, so either a 12 cell or 6 cell pack would be needed. This results in either increased volume requirements or decreased battery capacity, neither of which is viable for MARMOTSat. Additionally, there is significantly reduced power generation under non worst-case conditions. Given the uncertainties in radiation-induced degradation and limited in-orbit data for Microlink cells, DET is not a viable strategy for MARMOTSat.

Peak Power Tracking Peak Power Tracking offers a compromise by regulating the solar array voltage to a fixed setpoint using a Battery Charge Regulator (BCR). The setpoint is typically chosen to correspond to the MPP under worst-case thermal conditions, ensuring continuous power generation. Unlike DET, PPT decouples power generation from battery state of charge and provides flexibility in battery configuration. However, since the MPP varies with temperature, operating at a fixed voltage is suboptimal in non-worst-case conditions.

Using the same data as in Figure 5.7, setting the PV array voltage to 8 V yields approximately 2.8 W per 4S string across all expected temperatures. Given the thermal team's worst-case PV temperature projection of 125 ℃, reduced power generation at lower temperatures is an acceptable trade-off.

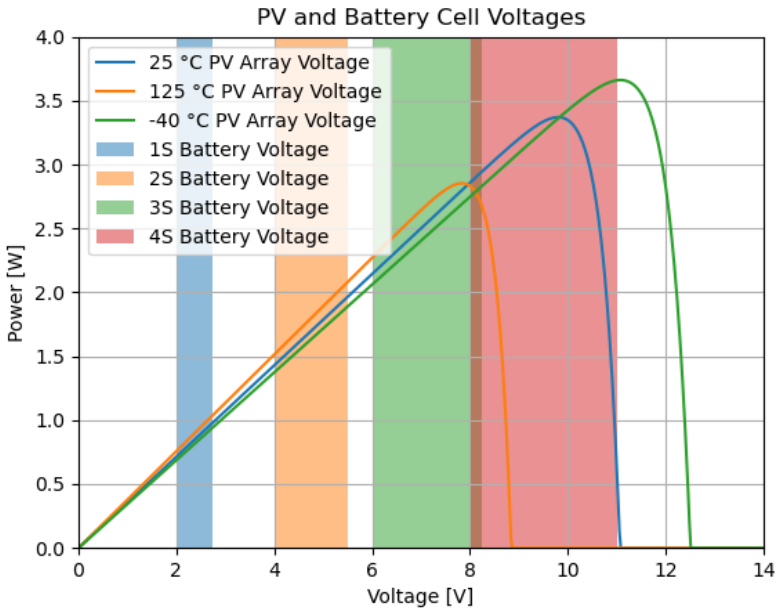

Figure 5.7: Comparison of Battery Cell Voltages and PV Cell Voltages

Maximum Power Point Tracking MPPT employs a closed-loop control algorithm to dynamically track the true MPP of the solar array. The system adjusts the solar array voltage based on real-time power measurements to maximize output. While MPPT introduces additional software complexity and requires extra components, it can significantly enhance efficiency. For MARMOTSat, MPPT was implemented alongside PPT as an optional feature. By default, the EPS operates in PPT mode, but MPPT can be enabled via command once the spacecraft is operational. This allows for higher power without much additional risk, as the system can function without MPPT working.

Solar Array Configuration The next major architectural decision is whether the PPT/MPPT should track the whole solar array to a single voltage or whether panels should be tracked individually. Individually tracking panels can increase the efficiency of the system, as panels at different temperatures will have different MPP voltages. Tracking to the global MPP of all panels results in slightly reduced power compared to tracking each panel individually. This scheme can also reduce the complexity of the BCR circuitry, as the individual BCRs can be lower power; allowing for more integrated devices, such as SMPS with integrated switches. The main downside is the increased board area required for the multiple converters and slightly increased harnessing between the PV array and the EPS module, due to the need

to connect panels individually instead of in parallel. For the MARMOTSat mission, it was decided to track all panels to a single voltage using a single BCR. This was mainly chosen to reduce the board area and allow the EPS to fit easily on a single PC104 PCB. The losses resulting from MPP mismatches are not expected to be significant. As deployable panels are expected to be approximately the same temperature, meaning MPP mismatches due to temperature variations should not be significant. Additionally, due to the spacecraft geometry, the body-mounted and deployable panels generally do not generate significant amounts of power at the same time; thus, MPP mismatches due to partial shading are expected to be minimal.

5.3.2 Bus Voltage

The EPS bus voltage is the primary output voltage produced by the PV array and batteries, which is then distributed to downstream regulators. This voltage level has significant impacts on the EPS design and performance, so it must be selected carefully. The first major choice is whether the bus voltage should be regulated to a fixed value or simply the raw battery voltage. The main advantage of a regulated bus voltage is that it slightly simplifies the design of downstream regulators and devices, as they only need to be designed for a single input voltage; however, this complicates the design of the PV regulator and BCR significantly. In the case of MARMOTSat, there was little advantage to a regulated bus voltage, as the design of downstream regulators to handle all battery voltages did not present a significant challenge.

With an unregulated bus voltage scheme selected, we must now select the voltage range in which the bus should be. This is determined by the configuration of the battery pack, more specifically the number of cells connected in series. As MARMOTSat uses an 8 cell pack, this gives 4 options: 1S, 2S, 4S, and 8S; the voltage ranges for each of these configurations are listed in Table 5.4, along with the resistive losses per mΩ under high load.

Configuration	Operating Voltage	Max Current (40 W)	Loses per mΩ
1S	2-2.75 V	20 A	400 mW
2S	4-5.5 V	10 A	100 mW
4S	8-11 V	5 A	25 mW
8S	16-22 V	2.5 A	6.25 mW

Table 5.4: Battery Pack Voltage Ranges

The 1S and 2S battery configurations result in relatively high currents under full load, leading to significant resistive losses due to the I^2R relationship. Assuming a conservative shunt resistance of 20 mΩ, the 1S configuration incurs approximately 20% power loss, while the 2S configuration experiences around 5%. Although the 5% loss is more tolerable, it still presents practical challenges for efficient power conversion and distribution at low voltages. Initially, a 2S configuration was selected to leverage design heritage from the ORCASat EPS. A prototype Battery Charge Regulator (BCR) was constructed for this configuration and achieved roughly 90% efficiency at full load. However, the associated heat dissipation raised thermal management concerns, prompting a reevaluation of the approach. An 8S configuration was not considered due to several drawbacks: balancing an 8S battery pack would be more complex, the higher bus voltage would complicate power MOSFET and monolithic SMPS derating, and the resulting 22 V maximum voltage would exceed the input limits of the ADCS, necessitating an additional regulator. A 4S configuration was ultimately adopted for MARMOTSat, as it simplifies the EPS architecture. The bus voltage enables direct battery power for the ADCS subsystem and allows all regulated output channels to be generated using buck converters, avoiding the need for less efficient buck-boost converters required in a 2S system.

5.3.3 Power Regulation

Based on the power regulation requirements presented in Section 3.2, three different regulated voltages are required. To simplify the design and reduce the number of components, a single regulator will be used for each required output voltage as opposed to having one regulator per output channel. A summary of the final design parameters for the three regulated voltage rails provided by the EPS is shown in Table 5.5. The nominal voltages were chosen to be in the approximate middle of the allowable voltage ranges for the subsystems,

and the current requirement is set to approximately 1.5× the maximum expected subsystem current draw. This is to account for higher inrush currents that have not been fully characterized for all subsystems. As the GNSS receiver is the only subsystem that has a power supply ripple requirement, target ripple voltages for the other channels were somewhat arbitrarily chosen to be 100mV as it is small enough that it is unlikely to cause issues for the subsystems and easy to meet. Note that TT&C and the 5V ADCS channels require very similar but non-overlapping voltage levels; unfortunately, this situation could not be avoided without significant changes to the TT&C design. Allowing the TT&C subsystem to be powered off of 5V would be a desirable feature for future revisions to reduce the number of required voltage channels on the spacecraft.

Voltage	**Current**	**Ripple**	**Downstream Channels**
3.3±0.1V	4.5A	50mV	3V3 CDH, 3V3 GNSS, 3V3 ADCS
5.1±0.1V	1A	100mV	5V ADCS
5.5±0.1V	5A	100mV	5V5 TTC, 5V5 BURN

Table 5.5: EPS Power Regulation Design Requirements

5.4 Battery Charge Regulator

The battery charge regulator (BCR) is responsible for regulating the solar panel voltage and charging the spacecraft battery when the spacecraft is in the Sun. The key requirements for the BCR are listed below:

1. The BCR shall be >92% efficient when the input power of the solar array is 25 W. This is to ensure that the peak BCR power dissipation is under 2W, the exact number is somewhat arbitrary, but this value was used for thermal modeling and should be achievable. The average efficiency must also be $> 90\%$ to satisfy the system level efficiency requirement.

2. The BCR have a maximum (derated) input voltage of at least 14V to accommodate the maximum open circuit voltage of a cold solar array.

3. The BCR shall regulate the solar array to a default minimum voltage of 8 V by current limiting loads that would result in the solar array voltage dropping below this minimum value.

4. The minium solar array voltage shall be adjustable by software to between 7 V and 12 V to account for all solar array maximum power points that might be encountered during the mission.

5. The BCR shall charge the battery pack using a constant current/constant voltage charging scheme.

6. The BCR shall limit the maximum battery charge current to 1C to avoid reducing the battery life by charging at high C rates.

The output voltage range for the BCR overlaps with the input voltage range of the BCR, so a converter capable of stepping the voltage up or down is needed. This is most commonly done using a SEPIC converter or a 4 switch buck/boost converter. For the BCR to be able to control the voltage across the solar array for the PPT and MPPT modes, it must have a second control loop that regulates the input voltage in addition to the standard output voltage control loop present on all power converters. The maximum current into the battery can be estimated based on the lowest battery voltage and highest solar panel power output to determine if active current limiting is required. The peak solar array power is approximately 26W and the minimum battery voltage is 8V; assuming the 100% converter efficiency, this gives a maximum charge current of $\frac{26\text{W}}{8\text{V}} \approx 3.25\text{A}$. For the 1.3Ah cell used in a 4S configuration, this is $\frac{3.25}{2\times1.3} = 1.25$ C charge rate, slightly higher than the 1C requirement. This charge rate is unlikely to occur frequently or for extended periods of time as it can only occur with a cool solar array and a deeply discharged battery. Occasional charging at 1.25C is unlikely to significantly reduce the battery lifespan as the cells are rated for up to 2C charging, so active current limiting is not strictly required.

The main feature of the BCR that drove the design was the need for a second control loop to regulate the voltage across the solar array. This requires either the selection of the SMPS controller that has this feature built in or the design of an external control loop to add this feature to a more generic SMPS controller. Using an external control loop results in a much more generic and flexible design as it can be adapted to work with most standard SMPS controllers or topologies; whereas there are much more limited options for controllers with this control loop built in. In addition to this external control circuitry, additional analysis

is needed to ensure that the SMPS controller will be stable for both feedback paths. This analysis is somewhat unique to each SMPS controller, so it will not be discussed here. This is a viable option; however, using a SMPS controller that features a built in control loop is a much simpler option.

While using an SMPS with an integrated input voltage regulation loop is the simplest approach, the number of available controllers with this capability is limited. Table 5.6 summarizes the SMPS options considered that support MPPT or input voltage regulation. The LTC3119, used in the ORCASat EPS, reduces component count and design complexity thanks to its integrated switches. However, testing revealed relatively low efficiency (85%) under MARMOTSat peak load conditions, primarily due to the higher resistance of its internal switches. Additionally, the LTC3119's 18 V maximum input rating can only be derated by a factor of 0.67, compared to the typical 0.2 derating recommended for non-radiation-hardened power MOSFETs. Ultimately, the LTC4020 was selected for MARMOTSat as it meets all design requirements and allows for external switch selection. This enables minimized conduction losses and sufficient V_{DS} derating, reducing the risk of single-event burnout (SEB) and single-event gate rupture (SEGR). Other options, such as the LT8491 and BQ2756, were also considered but require I^2C configuration for certain features. This was deemed undesirable because onboard memory introduces susceptibility to single-event upsets (SEUs) that could unpredictably alter the BCR's configuration. Monolithic converters with integrated switches generally lacked the efficiency needed at the high currents and low voltages required by the MARMOTSat BCR, particularly due to their single input channel limitations.

Part Number	**Notes**
LTC3119	Monolithic Buck-Boost Converter (2.5-18V input)
LTC4020	Buck-Boost Controller (4.5 to 55V input)
BQ25756	Buck-Boost Controller (4.2 to 70V input), I2C controlled
BQ24650	Buck Controller (5V to 28V input)
LT8491	Buck-Boost Controller (6 to 80V input), I2C controlled
LT3120	Monolithic Buck-Boost Converter (2.5-26V input)
LTC4013	Buck Controller (4.5V to 60V input)
LTC4015	Buck Controller (4.5V to 35V input)

Table 5.6: SMPS Controllers with Integrated Input Voltage Regulation

5.4.1 Maximum Power Point Tracking

In order to track the PV cell maximum power point described in Sections 2.2 and 5.1, the input voltage regulation control loop of the LTC4020 is used. This control loop can be easily adapted to support both peak power tracking (PPT) and maximum power point tracking (MPPT) when controlled by an MCU and a DAC. Typically, the setpoint for this control loop is fixed using a simple voltage divider. However, by adding a third resistor to the divider, as shown in Figure 5.8, the setpoint can be dynamically adjusted by varying the voltage applied to the third resistor. The input voltage regulation setpoint, $V_{in-setpoint}$, is defined by:

$$V_{in-setpoint} = \left(\frac{V_{fb}}{R_2} + \frac{V_{fb} - V_{adj}}{R_3} \right) R_1 + V_{fb} \tag{34}$$

where:

- V_{fb}: The fixed feedback reference voltage of the LTC4020 (2.5V).
- V_{adj}: The voltage applied by the DAC or default bias to adjust the setpoint.
- R_1, R_2, R_3: Resistors in the voltage divider network (as shown in Figure 5.8).

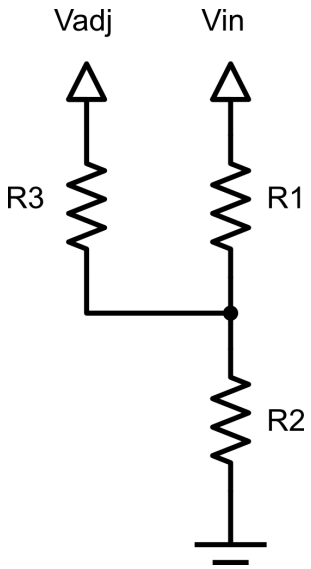

Figure 5.8: Three-Resistor Voltage Divider

To implement both fixed-setpoint (PPT) and dynamic (MPPT) modes, the circuit shown in Figure 5.9 is used. In this configuration, a default setpoint is defined by the selected values

of R_1, R_2, R_3, and the default V_{adj} voltage set by the voltage divider at the op amp input. This default can be overridden by applying a different analog voltage to V_{adj} using a DAC controlled by the MCU. When the MCU is disabled, the ADJ_MPPC input is high impedance, allowing the default voltage setpoint to be maintained via the voltage divider feeding the buffer op-amp input.

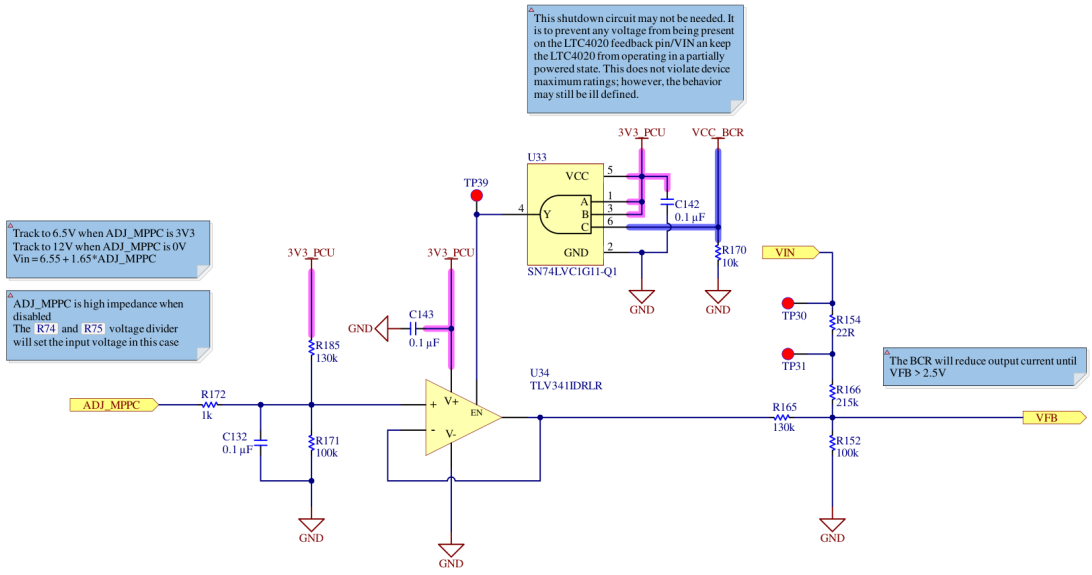

Figure 5.9: EPS Maximum Power Point Control Circuit

MPPT Algorithms Perturb and Observe (P&O) and Incremental Conductance (InC) are two widely used algorithms for MPPT [46]. P&O operates by incrementally perturbing the operating voltage and observing the resulting change in power, as shown in Figure 5.10. If the power increases, the algorithm continues in the same direction; if it decreases, the direction is reversed. While simple and easy to implement, P&O will oscillate around the maximum power point under steady-state conditions and may fail to track the MPP during rapidly changing irradiance, as it cannot distinguish between changes caused by perturbation and those caused by environmental variations.

InC is based on the fact that the PV curve is a concave function, so $\frac{\partial P}{\partial V}$ is positive to the left of the MPP and negative to the right; this relationship is described in Equation 35. The derivative can be approximated based on small changes in voltage and current using Equation 36, combining this with Equation 35 yields Equation 37. This equation represents

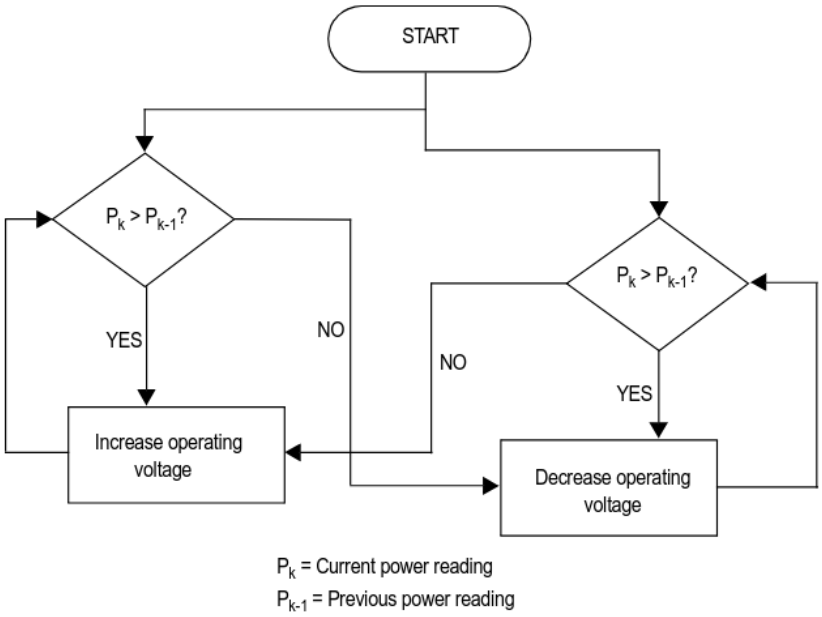

Figure 5.10: P&O Algorithm [46]

the main idea behind the InC algorithm; the location of the MPP can be inferred based on the incremental changes to the measured conductance ($\frac{I}{V}$) of the solar array. The complete incremental conductance algorithm is shown in Figure 5.11. Due to estimating the MPP using conductance and not power, the InC algorithm is able to more accurately track the MPP without the oscillation on P&O.

$$\begin{cases} \frac{dP}{dV} = 0, \text{ at } MPP \\ \frac{dP}{dV} > 0, \text{ left of } MPP \\ \frac{dP}{dV} < 0, \text{ right of } MPP \end{cases} \tag{35}$$

$$\begin{gathered} \frac{dP}{dV} = \frac{d(IV)}{dV} = \frac{IdV}{dV} + \frac{VdI}{dV} = I + V\frac{dI}{dV} \\ I + V\frac{dI}{dV} \approx I + V\frac{\Delta I}{\Delta V} \end{gathered} \tag{36}$$

$$\begin{cases} \frac{\Delta I}{\Delta V} = -\frac{I}{V}, \text{ at MPP} \\ \frac{\Delta I}{\Delta V} > -\frac{I}{V}, \text{ left of MPP} \\ \frac{\Delta I}{\Delta V} < -\frac{I}{V}, \text{ right of MPP} \end{cases} \tag{37}$$

Both of these algorithms are designed to track a PV array with a single MPP; however, as the MARMOTSat PV array has a number of PV cells connected in parallel, the IV curve

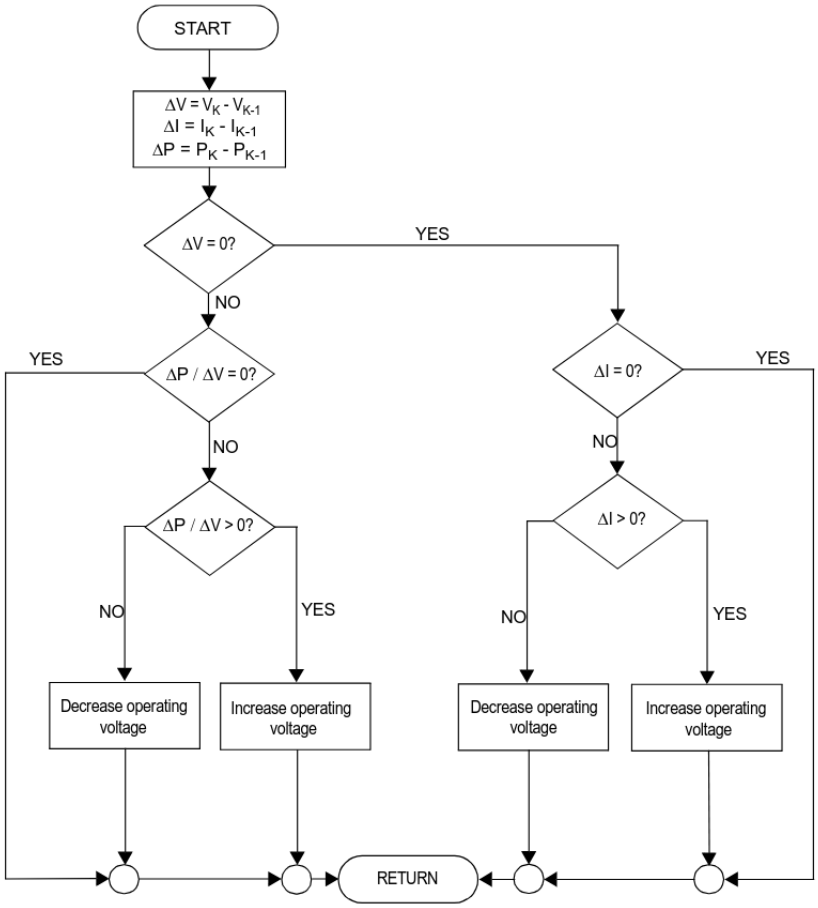

Figure 5.11: Incremental Conductance Algorithm [46]

of the solar array can have multiple MPPs, so the MPPT algorithm must ensure that it is tracking the true MPP and not a local MPP. An example of this is shown in Figure 5.12. The simplest method to determine the maximum power point is simply to sweep the array output voltage across the operating range and measure the current source at each point along the sweep. We can find the maximum power point by identifying the voltage that yields the maximum power. The main drawback of this method is that the solar array's power output will be reduced while the voltage sweep is in progress. This introduces a trade-off where performing more frequent voltage sweeps results in more accurately tracking the maximum power point, at the cost of losing more power due to the frequent sweeps. Combining a higher rate P&O or InC with periodic full array voltage sweeps offers a good compromise. Allowing the higher rate MPPT algorithm to track the MPP as it changes and periodically resetting it to the true MPP to ensure that it does not track a local maximum. For the MARMOTSat mission, the voltage sweep was combined with the InC algorithm as it offers

better performance than P&O with a minimal increase in complexity.

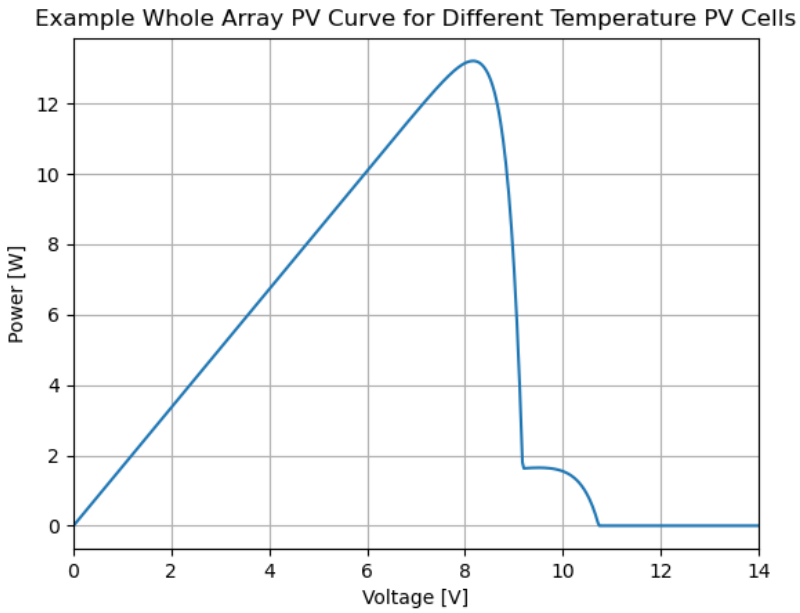

Figure 5.12: Whole Array IV Curve

5.5 Power Conditioning and Distribution

The power condition and distribution (PCD) subcomponent of the EPS is responsible for generating the regulated voltages described in Table 3.1, enabling and disabling power to subsystems, isolating faults to ensure that a fault in one subsystem cannot damage the EPS or other subsystems, and protecting subsystems from faults within the EPS. A block diagram of the PCD portion of the EPS is shown in Figure 5.13.

5.5.1 Power Regulation

The requirements for all three regulated channels are relatively similar; they all step down the same input voltage range to a lower voltage with less, and all have a maximum output current requirement of 5A or less. As all channels have similar requirements, a single converter design can be used for all three channels. As buck converters are by far the most common topology for high efficiency step down converters; this was the only option considered. Table 5.7 summarizes the requirements for the PCD regulators. A maximum input voltage of 40V was chosen, as this is a 30% derating of the 12V maximum expected input

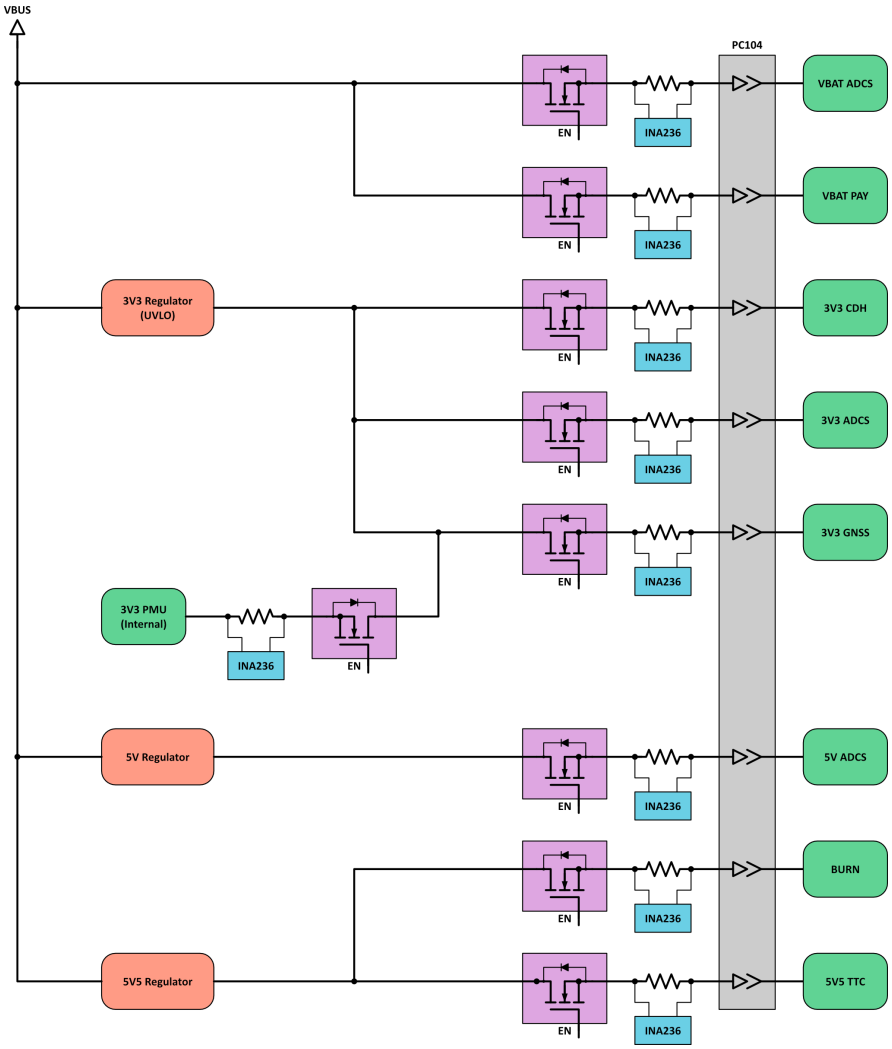

Figure 5.13: EPS BCD Block Diagram

voltage to reduce the risk of SEB/SEGR. A high conversion efficiency of over 90% in the 0.1-2A range is required to meet the 75% efficiency target, as this is the range of current that it is expected most power will be drawn at. The maximum load currents will very rarely be drawn, so efficiency at those higher transient loads is less impactful. Hundreds of buck converters meeting the requirements in Table 5.7 exist, most of which would be perfectly suitable for this application. Ultimately, the LM64460 was chosen for its high efficiency, automotive qualification, and requiring a minimal number of external components to function.

The two main design parameters of interest for the PCD regulators are the output voltage and output ripple. Table 5.8 summarizes the final design parameters for the regulators, accounting for component tolerances across the full temperature range and the voltage bias

Input Voltage	6V-40V
Output Voltage	3-6V
Output Current	$\geq$5 A
Efficiency (0.1-2A)	$>$90%

Table 5.7: PCD Regulator Requirements

effects on the MLCCs used in the output filters. Inductor selection was based on datasheet recommendations and compliance with off-gassing requirements suitable for space applications. Overall, the PCD regulators meet or exceed all system-level requirements.

Channel	V_{max} Req.	V_{max} Design	V_{min} Req.	V_{min} Design	V_{pp} Req.	V_{pp} Design
3V3	3.4 V	3.33 V	3.2 V	3.23 V	50 mV	$<$5 mV
5V	5.2 V	5.20 V	5.0 V	5.06 V	100 mV	$<$5 mV
5V5	5.8 V	5.68 V	5.4 V	5.50 V	100 mV	$<$5 mV

Table 5.8: PCD Regulator Design Specifications

5.5.2 Power Control and Protection

The internally regulated voltage channels must be distributed to the spacecraft's subsystems, which requires power control and protection circuitry. The desired behavior of the power control portion is relatively straightforward: when a subsystem is disabled, no current should be supplied, and all voltage rails should drop to approximately 0 V. Disabling current can be achieved by disconnecting the voltage rails from the supply using a FET; however, this does not guarantee that the subsystem will fully power off. Subsystems typically contain a large number of decoupling capacitors that discharge over an indeterminate period, as the nonlinear behavior of CMOS loads with respect to voltage and temperature can result in partial state retention at very low voltages. In practice, it may take several seconds for a subsystem to fully power down after supply removal.

This slow discharge is undesirable, as it complicates verification that a subsystem has been fully power-cycled. To mitigate this, the supply voltage can be pulled to ground through a relatively low impedance path to rapidly discharge any residual capacitance, bringing the rail voltage to near 0 V within a predictable timeframe. This feature is commonly known as Quick Output Discharge (QOD) and is integrated into many commercial load switches.

Subsystems and the EPS must be protected from two types of faults: overcurrent and overvoltage. Overcurrent conditions in a subsystem can arise from various causes, such as a single event latchup (SEL) during flight or mishandling during Assembly, Integration, and Testing (AI&T). Excessive current draw can damage EPS power converters and cause voltage rails to drop, potentially browning out other subsystems. Thus, protection circuits must both safeguard the EPS and isolate faults so that a malfunctioning or damaged subsystem does not affect others. Overvoltage conditions may result from internal EPS faults such as single event transients (SET), necessitating protection to prevent damage to downstream subsystems during both development and flight.

These considerations lead to the following design requirements:

1. Overcurrent faults within a subsystem shall be isolated to prevent damage to the EPS or other subsystems.

2. Subsystems shall be protected from overvoltage transients generated by the EPS.

3. The EPS shall allow the OBC to disable power to subsystems.

4. Disabled voltage channels must have a low impedance connection to ground.

Three approaches were considered for implementing the protection circuitry: digital control circuits, analog protection circuits, and fully integrated protection ICs. The first two approaches involve monitoring voltage and current on each rail and controlling a FET to disable the channel if limits are exceeded. This can be achieved using entirely analog circuits, such as current shunt amplifiers and comparators, or with digital control via an MCU or FPGA paired with ADC measurements. However, both options require significant design and verification effort and can reduce overall reliability due to the increased component count compared to a single highly-integrated solution.

Several FET-based protection devices are commercially available, often marketed as “eFuses” or “hot swap controllers.”For the MARMOTSat EPS, the Texas Instruments TPS25946 eFuse was selected, primarily due to its flight heritage on the ORCASat mission. The TPS25946 provides fast overvoltage and overcurrent protection, with response times of 1.2 μs and 500ns, respectively. As shown in the block diagram in Figure 5.14, the device integrates a

high-side FET controller, overvoltage and overcurrent comparators, and timing circuitry. This architecture closely resembles the previously discussed discrete analog solution but offers a more compact, reliable, and extensively validated implementation within a single IC.

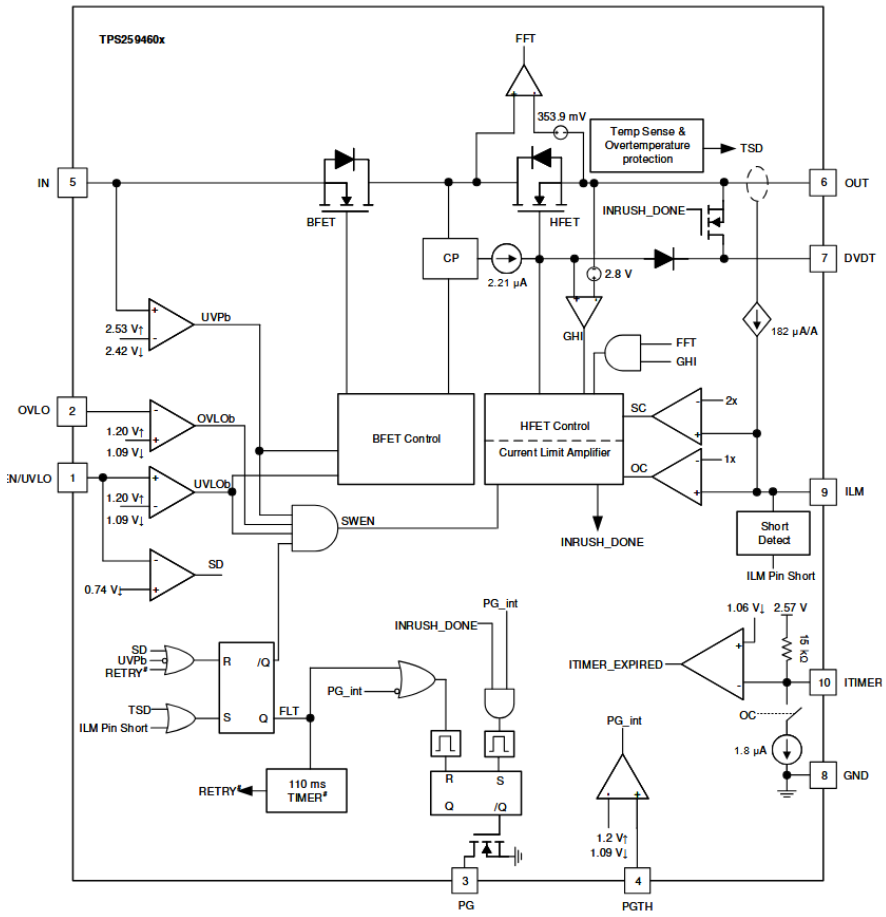

Figure 5.14: TPS25946 Block Diagram

The main limitation of the TPS25946 is its lack of built-in QOD functionality. However, this can be readily added using the external circuit shown in Figure 5.15. When the eFuse is disabled, the EN pin is pulled to 0V, disabling Q1A. This action pulls the gate of Q2A high, turning it on and providing a low impedance path between the channel output and ground through a 100Ω resistor.

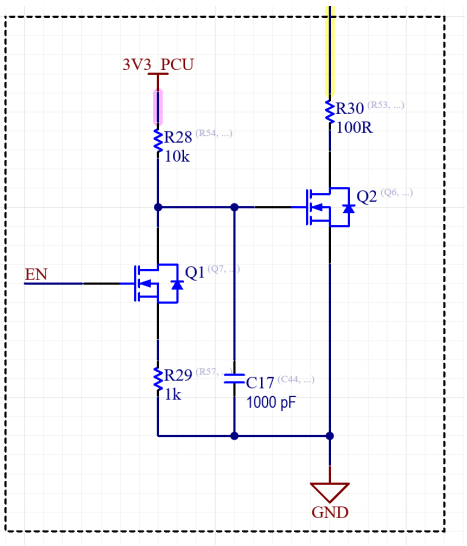

Figure 5.15: QOD Circuit

This combination of integrated eFuse protection with an external QOD circuit provides a reliable solution for power control and fault protection within the MARMOTSat EPS. These features ensure that subsystems can be safely powered, isolated, and cycled as required.

5.6 Deployment Timer & Inhibits

The inhibits must prevent both battery charging and power delivery to all subsystems, so a minimum of two inhibit switches are required. Figure 5.16 shows potential locations for placing the inhibit switches. The inhibit at position "A" is straightforward to implement because the LTC4020 controller used in the BCR includes a shutdown feature that disables switching and most internal circuitry, effectively inhibiting power from the PV array. Battery power can be inhibited from reaching the subsystems using switches at locations "C," "D," or "F." Among these, location "C" has the advantage of fully isolating power to the bus, regardless of the state of inhibit "A." This enables complete power cycling of the bus, simplifying the behavior of the heartbeat timer. The main drawback of location "C" is that it requires a high-side switch, which necessitates either a high-side NMOS driver or a PMOS-based inhibit switch, both of which are slightly more complex than a low-side NMOS inhibit. An additional requirement for this inhibit is that it must draw less than 100 μA when active to avoid discharging the spacecraft batteries during integration.

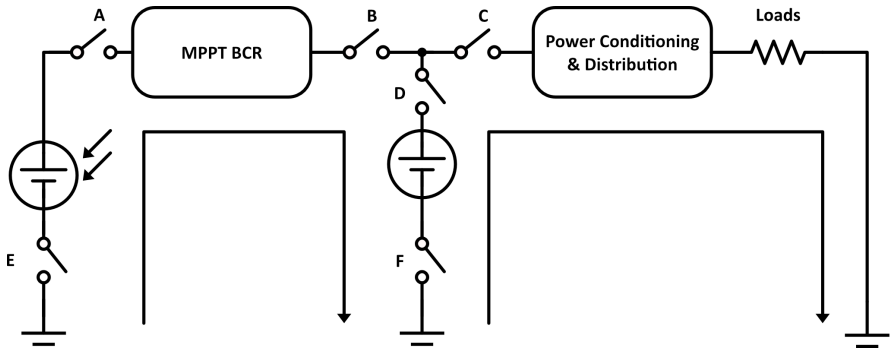

Figure 5.16: Possible Inhibit Switch Placement

The complete inhibit system, referred to as the Power Control Unit (PCU), is shown in Figure 5.17. The PCU is powered by both the PV array output and the battery via ORing diodes, allowing it to function even in eclipse when the batteries are fully depleted. A 2-second watchdog timer is integrated to automatically power cycle the entire bus if it is not regularly toggled by the OBC, enabling recovery from severe system lockups not handled by the OBC's onboard watchdog.

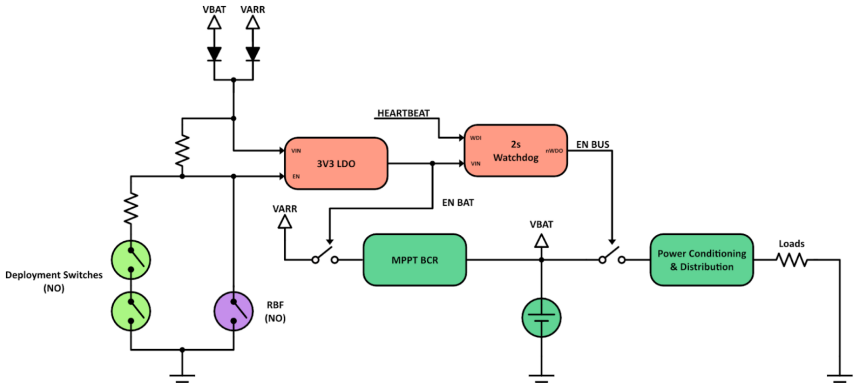

Figure 5.17: Full Inhibit System (PCU)

The TPS22811 load switch was initially selected due to its low on-resistance of 8.4 mΩ, low shutdown current of 20 μA, and built-in Quick Output Discharge (QOD) feature. However, its maximum input voltage rating is 16 V, which allows only a 0.7 derating factor relative to the operational voltage, much less than the recommended 0.2 for non-radiation-hardened power MOSFETs. For future revisions, the TPS25946, already used in the channel protection and control circuitry, is a potential alternative. It offers a higher maximum input voltage of 23 V but comes with a higher on-resistance of 40 mΩ. Even so, under a 20 W load, this only results in approximately 250 mW of power loss, and around 63 mW under a typical 10 W

load. These losses are roughly five times higher than those of the TPS22811 but remain negligible relative to the overall EPS efficiency.

5.7 Battery Pack

As previously discussed, the MARMOTSat EPS battery pack employs lithium titanate (LTO) cells to enable sub-zero charging without active thermal control. Cells are matched by capacity and internal resistance to ensure the pack capacity is not limited by a single "bad" cell; however, these parameters alone do not prevent cumulative state-of-charge (SoC) divergence in series-connected battery packs. The primary driver of long-term imbalance in such systems is differences in coulombic efficiency between cells, which cause each cell's SoC to change by slightly different amounts during every charge-discharge cycle. While differences in self-discharge rates also contribute to imbalance, their effect is generally small given the low self-discharge rates of LTO cells. The cumulative SoC imbalance at EoL can be estimated using Equation 38 adapted from [47], where $\delta\eta_c$ is the fractional difference in coulombic efficiency between cells, N_c is the number of cycles, and DoD is the depth of discharge per cycle.

$$\Delta\text{SoC}_{EoL} = \delta\eta_c \times N_c \times \text{DoD} \tag{38}$$

For MARMOTSat's five-year mission duration with a 20% DoD, limiting EoL SoC divergence to 20% would require controlling $\delta\eta_c$ to approximately 0.003%, a level that is neither practical to achieve nor measure with the available test equipment. This limitation highlights that while passive balancing is sufficient for short-duration missions or low DoD cycling, like the ORCASat mission, which operated for seven months with a 5% DoD and showed no significant signs of imbalance, missions with higher DoD and longer lifetimes require active balancing approaches. To mitigate this, a passive balancing strategy using resistive bleed paths will be implemented for the MARMOTSat mission. A high level block diagram of this system is shown in Figure 5.18, PFET driving and cell voltage monitoring circuitry is not shown. The detailed design of this updated battery pack is still under development, as the initial plan assumed a purely passive scheme similar to ORCASat. Implementation specifics are beyond the scope of this thesis.

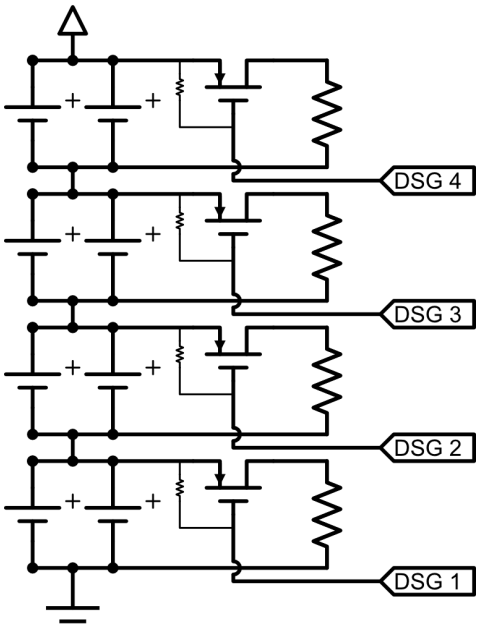

Figure 5.18: Simplified BMS Balancing Scheme

5.8 Telemetry

The two primary goals of the MARMOTSat EPS telemetry are:

1. Enable operators to assess the health of the EPS and spacecraft to support informed mission-level decision making.

   (a) Verify that the spacecraft remains power positive. This also enables in-orbit validation of the power budget.

   (b) Ensure that the spacecraft and EPS operate within safe temperature limits. This facilitates verification of onboard thermal models and the thermal budget in orbit.

   (c) Detect anomalies such as overvoltage or overcurrent conditions on any power channel.

2. Provide telemetry to support in-orbit verification of EPS performance and flight qualification of the design.

   (a) Estimate in-orbit EPS efficiency.

   (b) Estimate battery state of charge (SoC) and state of health (SoH).

   (c) Measure solar panel power generation and assess photovoltaic health.

From these high-level goals, we derive the required accuracy and sample rate for voltage, current, and temperature measurements. The MARMOTSat thermal team determined that one temperature reading per external face, accurate to within ± 2℃ and reported every 5 minutes, is sufficient to verify the thermal budget. The TMP1826 digital temperature sensor was selected for this purpose due to its single-wire interface, which simplifies harnessing between the EPS and spacecraft structure. The remaining telemetry requirements directly relate to EPS performance and are addressed in the following sections.

Note that the EPS is not responsible for telemetry storage. Instead, telemetry will be periodically requested by the OBC, which is responsible for storage and eventual downlink. A detailed description of this interface, including the list of telemetry items, is provided in Appendix B.

5.8.1 Spacecraft Power Consumption

To verify the power budget, the orbit average power (OAP) consumption of each subsystem must be measured to within $\pm 5\%$. This target provides useful insights without imposing excessive engineering effort on the EPS telemetry system. For reference, the minimum average power consumption of the MARMOTSat bus is approximately 3 W in nominal mode. Over a $\sim$1.5-hour orbit, this corresponds to a total energy usage of about 4.5 Wh. To achieve $\pm 5\%$ accuracy, the OAP energy measurement must be accurate to within ± 220 mWh. Since subsystem power draw varies over time, both voltage and current measurement errors and sampling errors (due to the stochastic nature of power draw) must be considered.

The sampling-induced error is the deviation between the true mean power and the sample mean. As this is a stochastic process, we cannot define absolute error bounds; instead, we require that the standard deviation of the OAP measurement be less than 37 mWh, corresponding to a 99.7% confidence interval of ± 110 mWh. This allocates half the error budget to sampling and the other half to sensor inaccuracies. This error allocation is somewhat arbitrary; however, as shown in Section 5.9.2 the selected sensors meet this measurement error requirement. The standard deviation of the sample mean (σ_M) is related to the population standard deviation (σ) and the number of samples (N) as follows:

$$\mu_M = \mu_P \tag{39}$$

$$\sigma_M = \frac{\sigma}{\sqrt{N}} \tag{40}$$

Estimating the standard deviation of spacecraft power draw without flight data is difficult. A simplified three-level power model (standby, payload, and peak) was adopted to approximate power variation, as summarized in Table 5.9. This model yields a standard deviation of 3.6 W, corresponding to 5.4 Wh orbital energy standard deviation. Using Equation 41, the required telemetry sampling rate (S_{rate}) for a target measurement standard deviation σ_{target} over orbit duration T_{orbit} is:

$$S_{rate} \geq \left(\frac{\sigma}{\sigma_{target}}\right)^2 \frac{1}{T_{orbit}} \tag{41}$$

For nominal mode, this yields $S_{rate} > 17$ samples/s. To ensure margin, a telemetry rate of 50 samples/s was selected.

Mode	**Power Draw**	**% Active**
Standby	3 W	79%
Payload	18 W	20%
Peak	50 W	1%

Table 5.9: Spacecraft Power Draw Estimates

$$\sigma = \sqrt{\sum p_i (x_i - \mu)^2}, \quad \mu = \sum p_i x_i \tag{42}$$

5.9 Spacecraft Power Generation

To validate the power generation budget, it is necessary to estimate how much power the solar panels can produce. The spacecraft draws maximum power from the PV array only when the combined battery charging and bus load exceeds the array's generation capability. If the battery is fully charged and the bus is in a low power state, the PV array will operate above its maximum power point (MPP), generating less than its potential maximum. Measuring the time the PV array operates at the MPP each orbit provides a rough indication of power margins: minimal time at MPP suggests excess generation capacity, while extended

MPP operation indicates near-full utilization of available power. Additionally, tracking the maximum PV power output per orbit can help monitor array health; declines may indicate degradation from radiation, atomic oxygen, or other environmental factors. Monitoring the MPP voltage also provides insights into PV cell condition, as shifts can signal performance changes. All power measurements should maintain an accuracy of $\pm 3\%$ to detect subtle variations in photovoltaic performance.

5.9.1 Battery SoC and SoH

There are two main parameters which battery telemetry should provide information about:

1. The current capacity of the battery pack (SoH), as this will degrade over the mission
2. How much of the battery capacity is being used (maximum depth of discharge)
3. How much capacity is currently available (SoC)

Both of these parameters can be estimated by knowing:

- The orbit minimum pack voltage
- The orbit maximum pack voltage
- The current pack voltage
- The amount of charge (Ah) sunk by the pack over an orbit
- The amount of charge (Ah) sourced by the pack over an orbit

The battery SoC can be estimated from the battery voltage, so the minimum battery voltage roughly corresponds to the minimum SoC. The battery voltage also depends on the temperature of the battery and the current that is sourced or sunk by the cell; so this method only provides a rough estimate of the SoC. Similarly, the SoH of the battery is related to the change in SoC vs charge sourced by the battery. Measurement of the total number of Ah sourced by the cell as well as the minimum battery voltage gives a rough estimate of the battery SoH. If the minimum battery voltage decreases for the same amount of discharged charge, then the battery capacity/SoH decreases. These limitations are acceptable for the MARMOTSat mission, as general trends are of more interest than exact measurements of

the battery SoC and accuracy estimating the SoC requires relatively complex battery models to be developed. This effort was not considered worthwhile for this mission. A resolution of 5 mV for the voltage of the battery pack and $\pm$ 3% for the current measurements is required. The battery voltage is between 2.5V and 2V for most of its SoC, so a 5 mV resolution gives 100 points in this region, allowing for reasonably precise estimation of the battery SoC. The current measurement requirement was selected to match the PV array measurement accuracy requirement.

5.9.2 Voltage and Current Measurements

The telemetry system must measure a number of different voltages, currents, and temperatures at similar levels of accuracy. A total of 11 voltage & current monitors and 12 temperature sensors are required:

- One voltage/current sensor per EPS output channel to monitor subsystem power consumption (8$\times$)
- One voltage/current sensor for the internal 3V3 PMU channel that power the telemetry collection system
- One voltage/current sensor for the solar array
- One voltage/current sensor for the battery
- One temperature sensor for each spacecraft face and deployed panel (10$\times$)
- One temperature sensor for the battery pack
- One temperature sensor for the PCDM

Two high-level approaches to measurement were considered: using all analog sensors that are then measured by an ADC or using all digital sensors with built-in ADCs that are then interfaced directly to an MCU. The analog solution allows for simpler testing as all signal levels can be measured directly with a voltmeter without the need to develop any software. However, this option complicates the hardware design and requires a large number of analog muxes and a large number of analog signals to be routed to the ADC.

For this reason, the digital solution was selected. The digital telemetry collection scheme is shown in Figure 5.19.

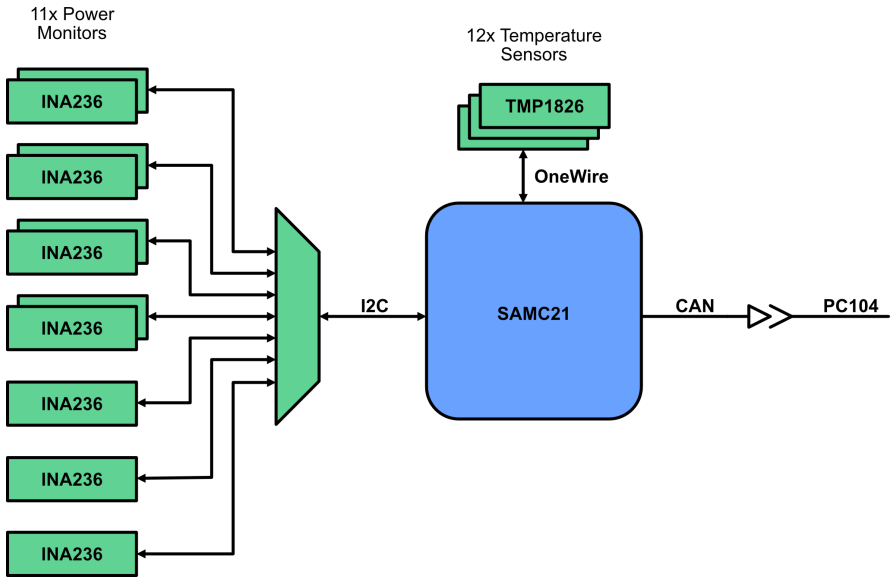

Figure 5.19: Digital Telemetry Collection Scheme

The INA236 was selected as the digital voltage and current sensor for its high accuracy and low power consumption. It features a built-in 16 bit 6.8 ksps ADC and bidirectional current shunt amplifier, allowing a single sensor to monitor both voltage and current. The INA236 has several key error sources that affect measurement accuracy. Shunt resistor-related errors include tolerance and temperature coefficient, which directly impact current and power readings. The input offset voltage of the current sense of INA236 ($\pm 10\mu V$ maximum) is the dominant source of error at low currents. Similarly, the $\pm 7.5mV$ voltage measurement offset is the dominant source of error at low voltage levels. The gain error of $\pm 0.1\%$ contributes to errors throughout the measurement range for voltage and current measurements. We can easily see that the worst case voltage is $0.1\% + \frac{7.5\text{mV}}{3.3\text{V}} \times 100\% \approx 0.3\%$. Figures 5.20 and 5.21 show measurement errors vs voltage and current. Note that the error is dominated by the offset voltage at low voltages/currents, and the current measurement error is dominated by the tolerance of the 1% shunt resistor at higher currents. The offset and gain errors can be measured and compensated for using a two-point calibration, leaving only the offset/gain errors caused by the temperature drift of the ± 50℃ operating region; the results of this are also shown in Figure 5.20.

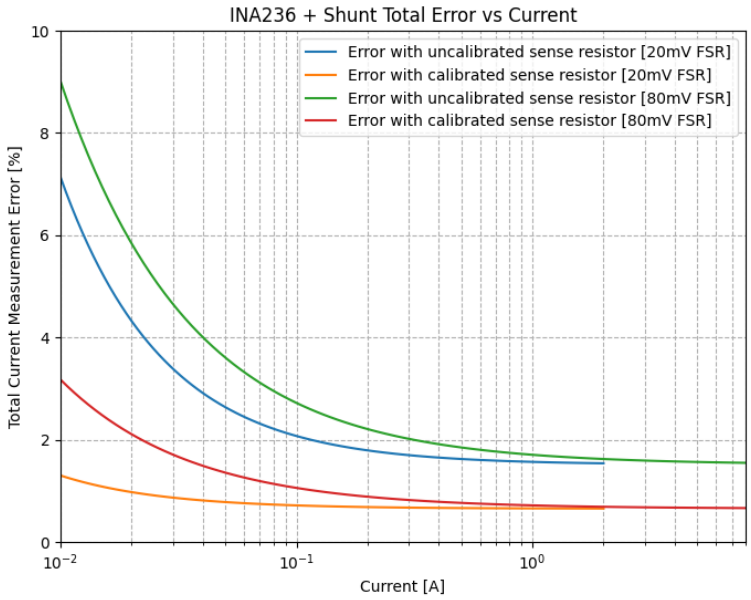

Figure 5.20: INA236 Current Measurement Error for a 100 ppm/℃, 1% 10 $m\Omega$ shunt

The exact accuracy of the measurements depends on the subsystem current draw; however, we can clearly see that the calibrated INA236 has much less than 2% current measurement error for all expected measurement ranges. The worst case voltage measurement error is 0.3%, so the total error is approximately 2.3%, less than the previously stated 2.5% power measurement accuracy requirements. The uncalibrated measurement error is also manageable; however, it will result in large measurement errors for some subsystems such as TT&C that have minimal current draw under nominal conditions, meaning the 5% OAP accuracy requirement may not be achieved for lower power modes, such as safe mode, without calibration.

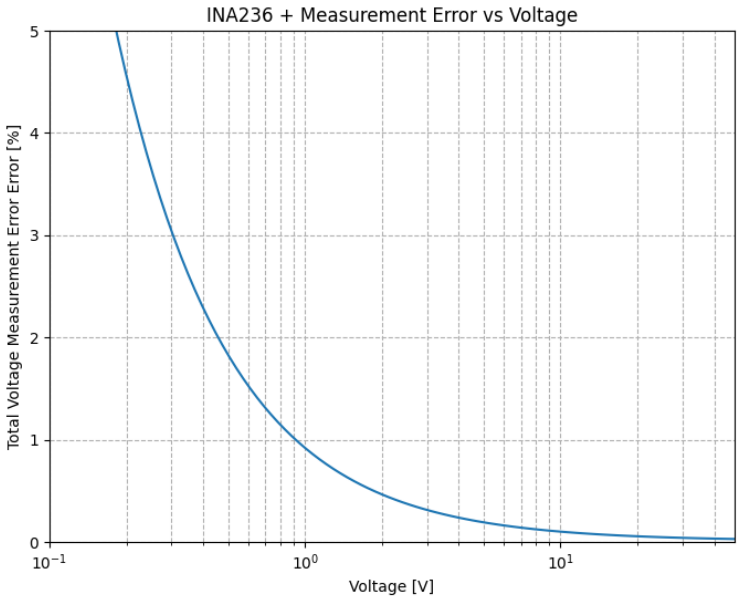

Figure 5.21: INA236 Voltage Measurement Error

6 Testing and Development

A rigorous testing campaign is essential to ensure that the EPS operates reliably throughout the mission in the space environment. A consistent and staged testing approach was followed for each MARMOTSat subsystem, beginning with early prototype validation and proceeding toward the qualification of the final flight hardware. Testing begins with the construction of prototype hardware, followed by basic functional testing to verify that each subsystem operates as intended. During this phase, modifications such as adjusting component values, cutting traces, or adding bodge wires are often required to address issues identified during initial tests. Integration with other subsystems is performed as early as possible to evaluate system-level compatibility. If design changes are identified, they are documented for incorporation into the next hardware revision. .

After the basic functionality of the design has been tested, extensive qualification and integration tests are performed to ensure that each subsystem operates according to design specifications and to identify subtle issues that may not be apparent during initial functional checks. This includes detailed measurement of the AC and DC characteristics of all major signals on the subsystems to ensure they match the expected design values and do not

exceed any component rating. Such testing is critical, as a subsystem may function correctly while only marginally meeting or even exceeding the maximum ratings of components, leading to early failures under flight conditions. For example, the maximum input voltage of a linear regulator can be exceeded and the component may continue to function for some time. This testing is conducted both at the subsystem level and the spacecraft level to identify any integration problems between subsystems.

Next, environmental tests are conducted to verify that the subsystems can operate under the conditions encountered in space. This includes thermal testing across the expected operating temperature ranges, vacuum testing to identify issues that may occur only in the absence of atmospheric convection, and long-duration stress testing at elevated temperatures to accelerate potential failures. A design that passes all of these tests can now be considered "flight-quality". Each unit produced from these designs must undergo acceptance testing to identify assembly-related defects. Acceptance testing includes comprehensive functional checks, thermal cycling, and visual inspection to reveal workmanship issues. Through this process, confidence is established that all subsystems will function reliably throughout the mission in the space environment.

To date, two full EPS prototypes have been constructed and tested; the first revision underwent limited testing because it quickly became apparent that significant design changes would be required to meet the efficiency and thermal requirements. The first revision was heavily based on the ORCASat design, including the 2S battery pack and using two PCBs connected via a board-to-board connector. Initial testing quickly showed that maintaining high efficiencies under up to 30W loads with this battery low voltage was not feasible due to high resistive losses, so it was decided to double the bus voltage to a 4S configuration to reduce resistive losses. Additionally, due to more relaxed launch provider requirements, much of the deployment inhibit and timer circuitry could be removed. This allowed the design to be condensed into a single board, simplifying the design, assembly, and testing of the EPS. The functional testing and initial qualification tests performed on the MARMOTSat EPS will now be presented; more extensive qualification, environmental, and integration testing has yet to be performed; however, the initial testing has indicated that a flight quality design can be made with only minor modifications to the current EPS PCDM revision shown in

Figure 6.1.

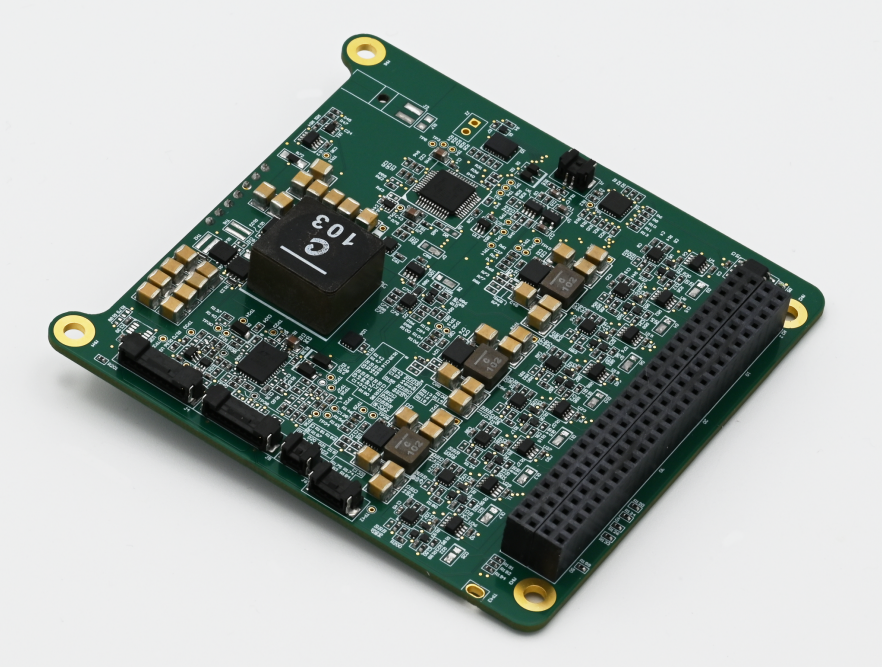

Figure 6.1: Second MARMOTSat EPS PCDM Revision

6.1 Deployment Inhibits

The goal of this test is to verify that the deployment inhibits removing power to the spacecraft bus when the normally open deployment switches are depressed, the spacecraft can be deployed from both the solar array and the battery, and that the current draw from the battery in the stowed state is under the $100\mu A$ requirement. The test setup for this test is very simple as shown in Figure 6.2. A power supply is used to supply voltage to the battery or solar array inputs on the PCDM, the PCDM current draw is measured using a 5 1/2 digit ammeter, the deployment switches are manually controlled and the bus voltage is measured using a digital voltmeter. The results of this test are summarized in Table 6.1. From this we can see that the basic inhibit functionality works and the 100μA stowed battery current consumption requirement is met. The higher current draw of 1.3mA from the PV array in the stowed state is also acceptable, most of this can be accounted for by the 10kΩ bleed resistor connected to the PV array input.

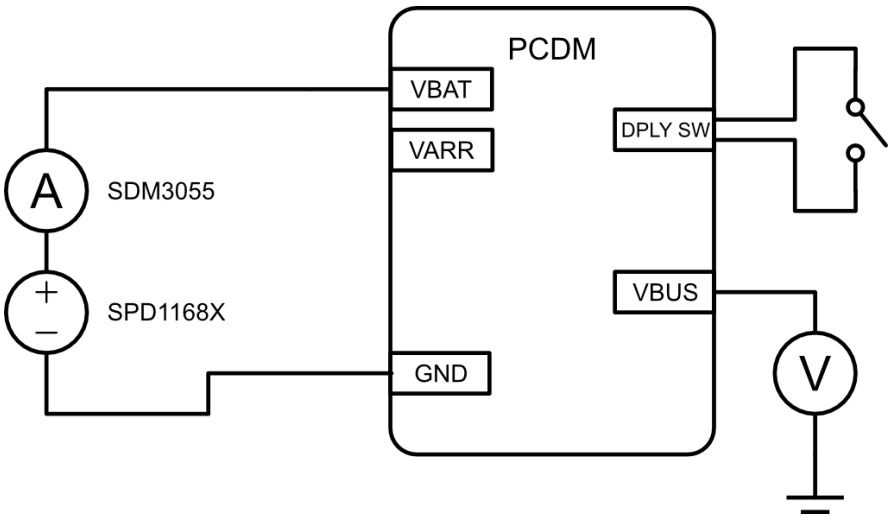

Figure 6.2: EPS Deployment Inhibit Test Setup

VBAT	VARR	SW State	Bus Voltage	Input Current
11V	Hi-Z	OFF	0V	32μA
11V	Hi-Z	ON	11V	0.8mA
8V	Hi-Z	OFF	0V	45μA
8V	Hi-Z	ON	8V	0.8mA
Hi-Z	10V	OFF	0V	1.3mA
Hi-Z	10V	ON	11V	7mA

Table 6.1: EPS Deployment Inhibit Test Summary

6.2 PCD Channel Control

This test verifies the basic functionality of the channel control circuit; verifying that all channels can be enabled or disabled. The test setup can be seen in Figure 6.3, the PCDM is powered on and the channel enable lines are pulled high, low, or left high impedance to determine the default state of the channel. Table 6.2 summarizes the results of this test; all channels can be enabled and disabled via the channel enable pins and have the expected default state. Note that the 3V3 CDH channel powers the OBC, which is always on and is responsible for enabling and disabling power to all other subsystems, so this channel cannot be disabled. The non-zero voltage measured on the disabled 3V3 PMU channel is due to some leakage current through the INA236s that have power applied to their sense inputs. This is not a major concern as 0.1V is well below the minimum power-on reset voltage of 0.8V for all devices on the EPS PMU, so all devices will be fully power cycled. This issue will be fully resolved in the next revision via the external QOD circuitry on the channel enable lines.

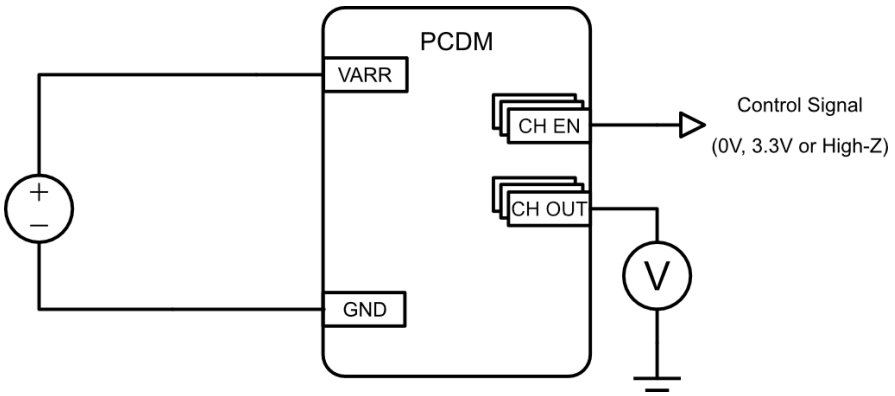

Figure 6.3: Channel Control Test Setup

Channel	Default Voltage	Enabled Voltage	Disabled Voltage
5V5 TTC	0.0V	5.6V	0.0V
3V3 PMU	3.3V	3.3V	0.1V
3V3 CDH	3.3V	-	-
3V3 GNSS	0.0V	3.3V	0.0V
3V3 ADCS	0.0V	3.3V	0.0V
5V5 BURN	0.0V	5.6V	0.0V
5V ADCS	0.0V	5.1V	0.0V
VBAT ADCS	0.0V	11.0V	0.0V
VBAT PAY	0.0V	11.0V	0.0V

Table 6.2: Channel Control Test Summary

6.3 SMPS Efficiency

The general test setup used to measure the efficiency of the SMPS on the EPS is shown in Figure 6.4, the key point to note is that 4-wire measurements must be used for the input and output voltages/currents. This ensures that the voltage is measured at the inputs/outputs of the DUT to avoid including the resistive losses of the cabling in the efficiency calculations. The PCD regulator efficiency was measured after the channel control and protection e-fuses so that the resistance of the e-fuse and sense resistors was also accounted for. When testing PCD efficiency, voltage was supplied directly to the VBAT input to avoid running current through the BCR. BCR efficiency was measured by supplying power to the VARR input and sinking current directly from the bus voltage via a dedicated test connector. The results of this test are shown in Figures 6.5, 6.7, 6.8 and 6.9.

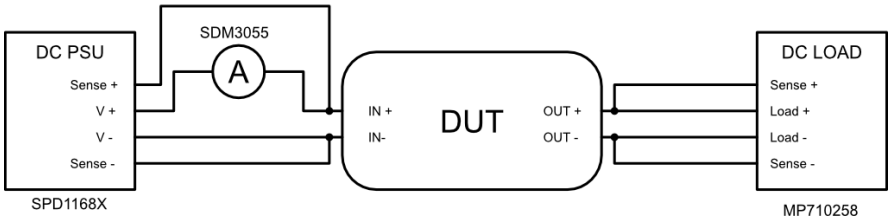

Figure 6.4: Regulator Efficiency Test Setup

BCR Results Figure 6.5 shows the BCR efficiency as a function of the input power and Figure 6.6 plots the total power dissipated as waste heat by the BCR as a function of the input power using the same data. We can see the general expected trend; at low power levels, the BCR efficiency is low and dominated by the static switching and quiescent losses. As the power level increases, these losses stay relatively constant, so the efficiency increases. At higher load currents, the resistive losses begin to dominate due to the I^2R term, resulting in a decrease in efficiency. In general, we would expect the power dissipation to be in an equation in the form $P_{static} + K_{switching}I + RI^2$. This pattern can be seen most clearly in Figure 6.6, where we can clearly see the power dissipation is a quadratic function for input currents larger than approximately 0.4 A. At currents below 0.4 A, LTC4020 operates as an asynchronous converter, where the low side buck and high side boost switches are not driven. Diodes with lower forward voltage drops than the FET body diodes are added in parallel with the disabled switches in the design to reduce the current through the body diodes of the FETs and improve efficiency. This mode results in slightly lower quiescent currents in low power modes, but causes much higher switching losses as the current increases due to the voltage drops across the switch bypass diodes. The drop in power dissipation when switching to the synchronous switching mode indicates that the threshold for entering synchronous mode could be lowered for a slight increase in efficiency at moderately low input currents. Overall, the BCR easily meets the 92% efficiency requirement the expected loads.

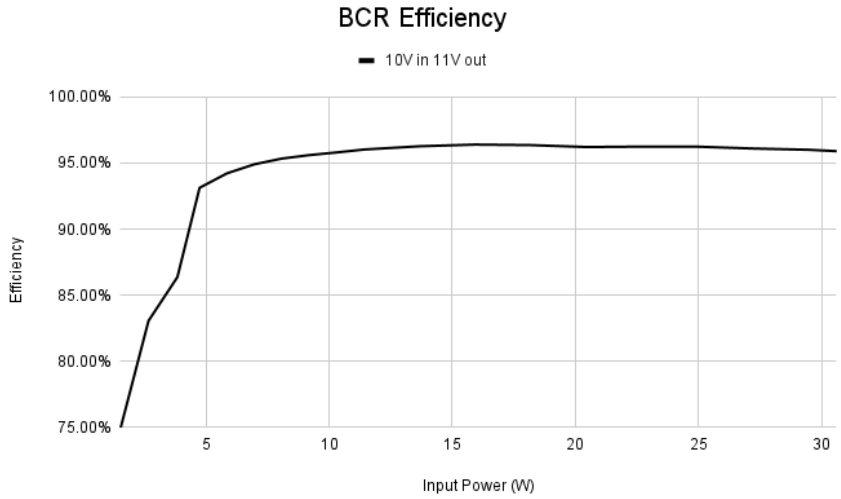

Figure 6.5: BCR Efficiency

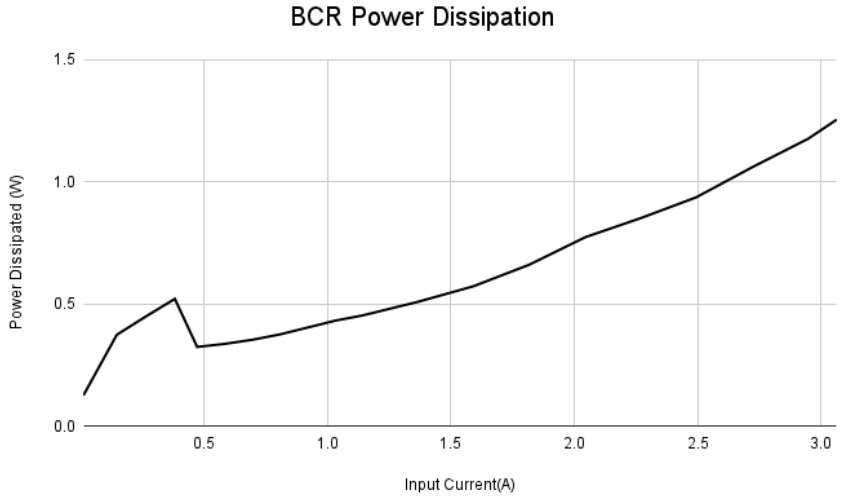

Figure 6.6: BCR Dissipated Power

PCD Results The PCD regulator efficiency was measured for both the pulse frequency modulation (PFM) and forced pulse width modulation (FPWM) modes, supported by the LM64460. FPWM forces the converter to always operate in CCM, reducing the ripple at low frequencies at the cost of reduced power consumption. The PFM adjusts the lowers the switching frequency under light loads to improve the light load efficiency at the cost of slightly higher ripple voltages at light loads. This matches the behavior observed in Figures 6.7-6.9. As the typical power draw from PCD regulators is less than 500 mA, PFM offers a significant increase in efficiency and should be used if possible, as the efficiency of PCD regulators is quite low under typical loads if the FPWM mode is used. As these regulators are highly integrated with fixed switching, there is limited room for further optimization of efficiency; however, they are able to meet the 90% efficiency target with PFM mode so no further optimization is required.

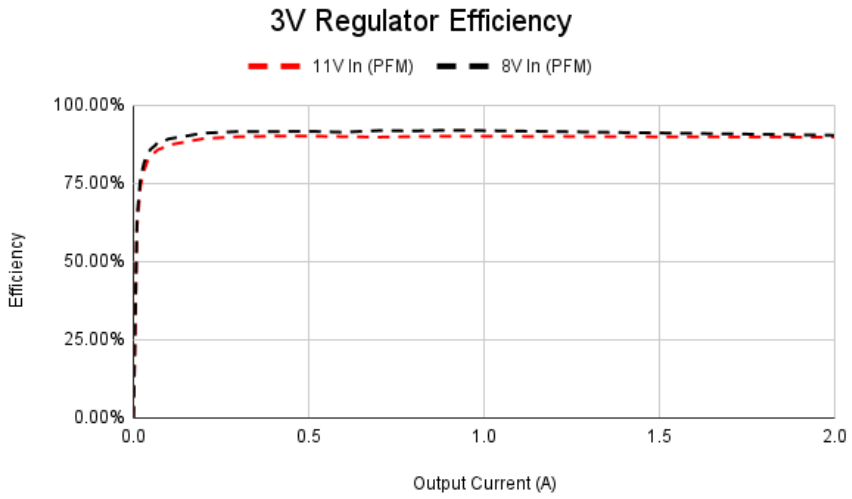

Figure 6.7: 3V3 Regulator Efficiency vs Output Current

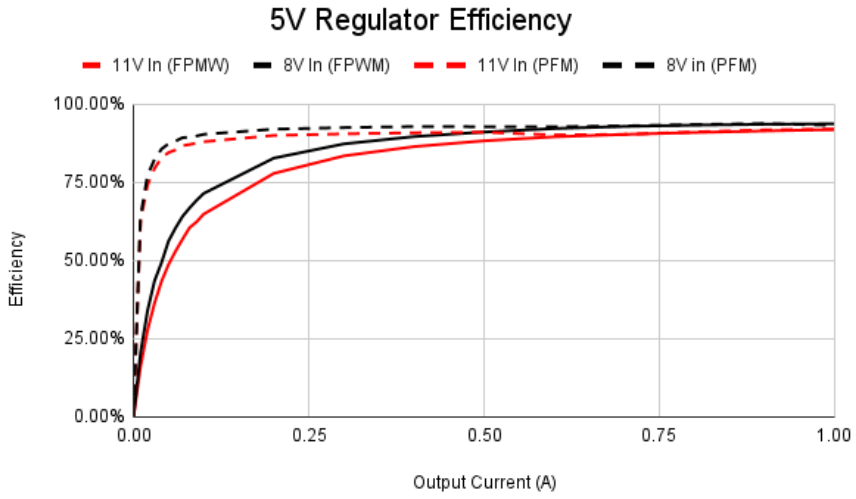

Figure 6.8: 5V Regulator Efficiency vs Output Current

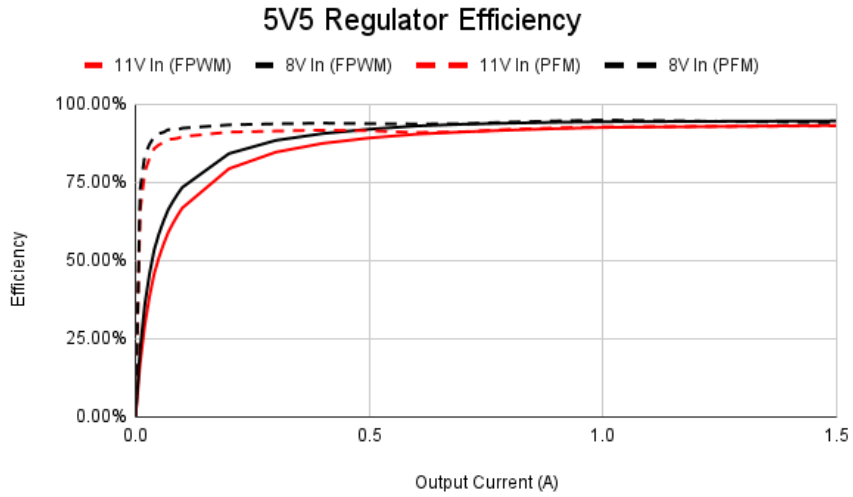

Figure 6.9: 5V5 Regulator Efficiency vs Output Current

6.4 SMPS Ripple

The ripple voltage test setup is shown in Figure 6.10, the key points to note are the use of power resistors as the load as opposed to a programmable DC load and the use of a 1x oscilloscope probe as opposed to the more common 10x probes. A power resistor was used as the control loop of a DC load can introduce additional noise into the ripple measurements, making the power supply ripple appear worse than it actually is. A high bandwidth 1x probe is needed as ripple voltages are relatively small and relatively close to the noise floor of inexpensive DSOs, so the 10x attenuation present on most probes will render the ripple measurements largely meaningless. Ripple measurements must be taken using the AC coupling mode of the DSO, as the used DSO does not support large enough offset voltages at the 2-5 mV/division scale required to measure the ripple voltage. Lastly, the bandwidth of the DSO was limited to 20 MHz to filter out higher frequency switching noise so that the ripple voltage can easily be isolated from other switching noise. Table 6.3 summarizes the results of this testing; note that most PCD regulators were tested in both forced pulse width modulation (FPWM) and pulse frequency modulation (PFM) modes.

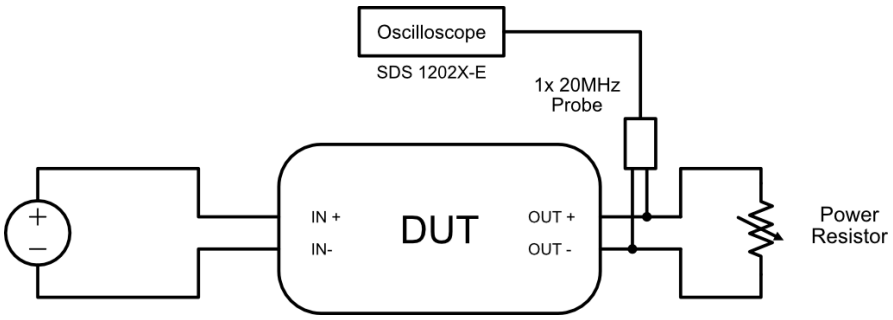

Figure 6.10: Regulator Ripple Test Setup

Regulator	Load	Peak to Peak Ripple	Ripple Frequency
BCR	Open	330mV	250Hz
BCR	100Ω	4mV	250kHz
BCR	10Ω	7mV	250kHz
3V3 (PFM)	Open	7mV	1kHz
3V3 (PFM)	330Ω	7mV	14kHz
3V3 (PFM)	3.3Ω	3mV	1.8MHz
5V5 (FPWM)	Open	2mV	2.1MHz
5V5 (FPWM)	560Ω	2mV	2.1MHz
5V5 (FPWM)	6Ω	3mV	2.1MHz
5V5 (PFM)	Open	6mV	1kHz
5V5 (PFM)	560Ω	9mV	10kHz
5V5 (PFM)	6Ω	2mV	2.1MHz
5V (FPWM)	Open	3mV	2.1MHz
5V (FPWM)	560Ω	3mV	2.1MHz
5V (FPWM)	6Ω	4mV	2.1MHz
5V (PFM)	Open	6mV	1kHz
5V (PFM)	560Ω	9mV	19kHz
5V (PFM)	6Ω	2mV	2.1MHz

Table 6.3: Ripple Voltage Test Summary

PCD Results As expected, the FPWM modes of the PCD regulators have the same switching frequency over all loads, and the PFM modes have lower switching frequencies at lower loads. Due to this, the ripple voltage is higher for PFM at light loads; however, the ripple voltages produced by PFM still easily meet our ripple requirements. Due to this, PFM is preferred because of its much higher efficiency at low loads.

BCR Results The ripple voltage on the BCR channel is very high when under no load; this is not an issue as the testing was performed without a battery present. The battery will always provide a light load to the BCR and reduce the ripple; even if this was not the case,

the high BCR ripple under no load is not problematic as it is never used directly and always run through an additional regulator either on the EPS or subsystem it is powering. We can also note that the switching frequency is reduced to 250 Hz under the no load conditions, so this high no load ripple appears to be caused by the LTC4020 reducing the switching frequency under no load conditions, and can likely not be reduced without using a different BCR IC. Under load, we note that the peak to peak ripple voltage is under 10 mV which is much less than the 100 mV requirement. This means that the switching frequency of the LTC4020 could be reduced to reduce switching losses and improve efficiency.

6.5 Maximum Power Point Control

The basic functionality of the maximum power point control circuit was tested using the test set-up shown in Figure 6.11. A DC 14 V power supply with a 300 mA current limit was used to supply the solar array voltage; the battery was then replaced with a DC load configured as 8 V constant voltage (CV) load. This simulates the high-impedance solar array along with a discharged battery. The CV load will draw current until the BCR lowers the output voltage to 8 V to maintain the minimum programmed input voltage. This will occur when the BCR input current reaches the output current limit of the power supply, causing the power supply to lower its output voltage to limit the current, causing the BCR IVR feedback loop to lower its output voltage to limit the output current. The voltage across the array input can be measured to determine what the input voltage regulation setpoint is. The theoretical and measured results for this system are shown in Figure 6.12. Note that the real system does not behave as predicted for the lower setpoints. This is due to the use of an op amp with a limited common mode range as a buffer for the DAC output. This can easily be fixed by selecting a different op amp with a larger common mode input range for the next revision.

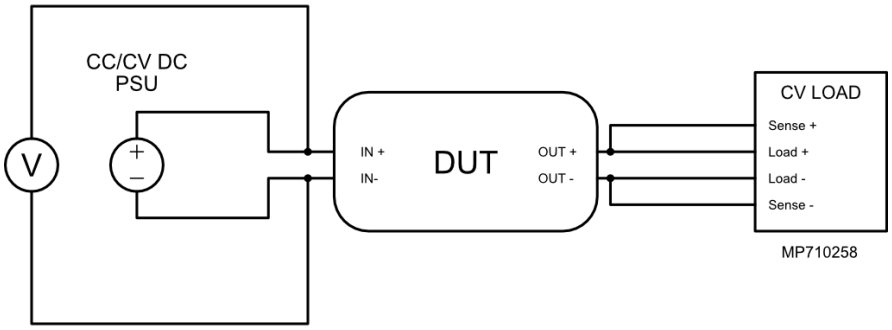

Figure 6.11: Maximum Power Point Control Test Setup

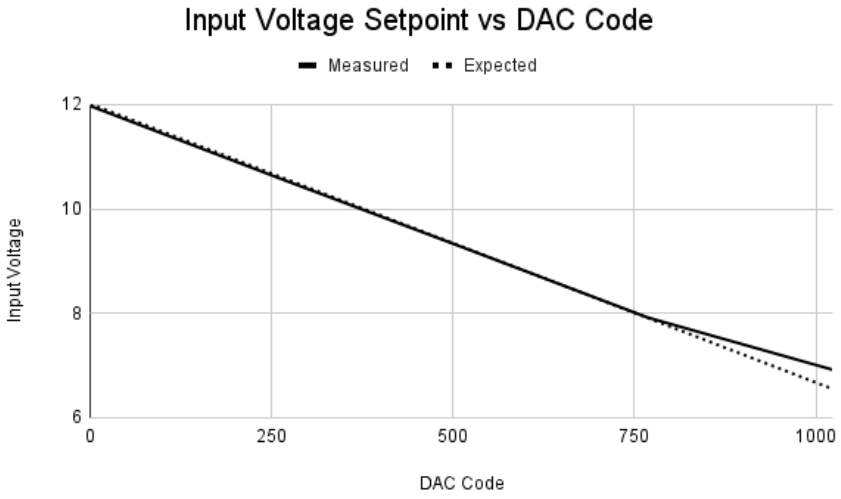

Figure 6.12: Maximum Power Point Tracking Adjustment vs DAC Code

7 Conclusions

This thesis presented the design, analysis, and implementation of the EPS for MARMOTSat, a 3U CubeSat developed at the University of Victoria under the Canadian Space Agency's CUBICS program. A comprehensive power budget analysis was conducted, incorporating spacecraft modes, orbit configuration, and deployable solar array configurations. This analysis informed the sizing of both energy generation and storage subsystems, ensuring power-positive operation across the full range of expected operating conditions. The spacecraft is expected to operate with a 30% power margin for nominal operation at the start of the mission; the margin will decrease towards the end of the mission due to solar cell degradation and attitude changes due to HF antenna drag. The rate of solar cell degradation is currently unknown as the selected cells have limited flight heritage; however, the spacecraft has several very low power modes of operation, so basic housekeeping and occasional payload operations will be possible even if the solar array degrades significantly. The data obtained from MARMOTSat on the degradation of the solar cells will be useful for informing future CubeSat missions on the viability of the alternative solar cells used.

In addition to the solar cells, the EPS uses lithium titanate (LTO) batteries to allow for subzero charging and remove the need for active thermal control, reducing system complexity and power consumption compared to traditional lithium-ion chemistries. These cells have flight heritage from ORCASat; however, the additional data provided by a longer duration mission will provide valuable information about their viability for larger and longer duration CubeSat missions.

The last major contribution of the thesis was the development of a new Power Conditioning and Distribution Module (PCDM) for MARMOTSat to allow for efficient power regulation, subsystem level protection, and extensive telemetry for system monitoring. This system features both a fixed hardware-based peak power point tracking and a software-controlled maximum power point tracking algorithm to harvest all available power from the solar array. Initial ground testing was performed to validate the design and characterize the performance of the PCDM. The array to load efficiency is approximately 85%, with the BCR having a peak efficiency of over 95% for most expected solar array input power levels

and the PCD regulators having around 90% efficiency for most expected load currents.

7.1 Future Work

While the MARMOTSat EPS is largely complete, several key items remain before it is flight-ready:

- Several minor design and footprint errors identified during testing of the current prototype must be resolved for the flight revision.
- The current prototype and flight revision must undergo additional qualification, environmental and integration testing, including thermal cycle testing, high and low temperature operation, basic testing in a thermal vacuum chamber and extensive integration testing with other MARMOTSat subsystems. Cobalt-60 or proton based radiation testing may also be conducted if facilities are available.
- The design of the battery pack must be updated to include the required balancing circuitry.
- The flight version of the EPS software must be developed, including the implementation of the software based MPPT algorithm.
- The assumptions made for the power budget must be verified once the orbital parameters for MARMOTSat are known.

References

[1] M. Swartwout, "The First One Hundred CubeSats: A Statistical Look," *Journal of Small Satellites*, vol. 2, no. 2, pp. 213–233, Dec. 2013. [Online]. Available: https://api.semanticscholar.org/CorpusID:220625425.

[2] ACC Clyde Space, *CubeSat EPS - STARBUCK-Nano*. [Online]. Available: https://www.aac-clyde.space/what-we-do/space-products-components/pcdu/cubesat-eps-starbuck-nano (visited on 07/16/2025).

[3] ORCASat Team, *ORCASat*. [Online]. Available: https://www.orcasat.ca (visited on 07/12/2025).

[4] A. Edpuganti, V. Khadkikar, M. S. E. Moursi, H. Zeineldin, N. Al-Sayari, and K. Al Hosani, "A Comprehensive Review on CubeSat Electrical Power System Architectures," *IEEE Transactions on Power Electronics*, vol. 37, no. 3, pp. 3161–3177, Mar. 2022, ISSN: 1941-0107. DOI: 10.1109/TPEL.2021.3110002. [Online]. Available: https://ieeexplore.ieee.org/document/9528921 (visited on 07/16/2025).

[5] EnduroSat, *EPS II*. [Online]. Available: https://www.endurosat.com/products/eps-ii-battery-pack/ (visited on 07/16/2025).

[6] Pumpkin Inc., *High-power Multi-channel Electrical Power System Module (EPSM1)*. [Online]. Available: http://www.pumpkinspace.com/store/p216/High-power_Multi-channel_Electrical_Power_System_Module_%28EPSM1%29.html (visited on 07/16/2025).

[7] NanoAvionics, *CubeSat Electrical Power System EPS*, en. [Online]. Available: https://nanoavionics.com/cubesat-components/electrical-power-system-eps-1-0-and-accessory-boards/ (visited on 07/16/2025).

[8] R. J. Boain, *A-B-Cs of sun-synchronous orbit mission design*, version V2, 2004. DOI: 2014/37900.

[9] H. D. Curtis, "Chapter 2 - The Two-Body Problem," in *Orbital Mechanics for Engineering Students (Third Edition)*, H. D. Curtis, Ed., Boston: Butterworth-Heinemann, Jan. 2014, pp. 59–144, ISBN: 978-0-08-097747-8. DOI: 10.1016/B978-0-08-097747-

8.00002-5. [Online]. Available: https://www.sciencedirect.com/science/article/pii/B9780080977478000025 (visited on 05/13/2025).

[10] J. Meeus, *Astronomical algorithms*, eng. Richmond, Va: Willmann-Bell, 1991, ISBN: 978-0-943396-35-4.

[11] S. V. Weston *et al.*, "State-of-the-Art of Small Spacecraft Technology - NASA," National Aeronautics and Space Administration, Tech. Rep., 2024. [Online]. Available: https://www.nasa.gov/smallsat-institute/sst-soa/ (visited on 04/28/2025).

[12] Spectrolab Inc., *Photovoltaics*. [Online]. Available: https://www.spectrolab.com/photovoltaics.html (visited on 06/22/2025).

[13] Azure Space, *SPACE Solar Cells*. [Online]. Available: https://www.azurspace.com/index.php/en/products/products-space/space-solar-cells (visited on 07/10/2025).

[14] A. Riverola, A. Vossier, and D. Chemisana, "Chapter 1 - Fundamentals of solar cells," in *Nanomaterials for Solar Cell Applications*, S. Thomas, E. H. M. Sakho, N. Kalarikkal, S. O. Oluwafemi, and J. Wu, Eds., Elsevier, Jan. 2019, pp. 3–33, ISBN: 978-0-12-813337-8. DOI: 10.1016/B978-0-12-813337-8.00001-1. [Online]. Available: https://www.sciencedirect.com/science/article/pii/B9780128133378000011 (visited on 07/10/2025).

[15] *Iv curve | pveducation*. [Online]. Available: https://www.pveducation.org/pvcdrom/solar-cell-operation/iv-curve (visited on 07/16/2025).

[16] G. Plett, *Battery Management Systems, Volume I: Battery Modeling*. Artech, 2015, ISBN: 9781630810245.

[17] M. Day, "Understanding Low Drop Out (LDO) Regulators," Texas Instruments, Tech. Rep., 2006. [Online]. Available: https://www.ti.com/lit/ml/slup239a/slup239a.pdf (visited on 07/10/2025).

[18] B. Hauke, "Basic Calculation of a Buck Converter's Power Stage," Texas Instruments, Tech. Rep., Aug. 2015. [Online]. Available: https://www.ti.com/lit/an/slva477b/slva477b.pdf (visited on 07/10/2025).

[19] B. Hauke, "Basic Calculation of a Boost Converter's Power Stage," Texas Instruments, Tech. Rep., Nov. 2022. [Online]. Available: https://www.ti.com/lit/an/slva372d/slva372d.pdf (visited on 07/10/2025).

[20] X. He, D. Li, and V. Zhang, "An Accurate Approach for Calculating the Efficiency of a Synchronous Buck Converter Using the MOSFET Plateau Voltage," Texas Instruments, Tech. Rep., Jul. 2020. [Online]. Available: https://www.tij.co.jp/jp/lit/an/slvaeq9/slvaeq9.pdf (visited on 07/10/2025).

[21] I. Jun, H. Garrett, W. Kim, *et al.*, "A review on radiation environment pathways to impacts: Radiation effects, relevant empirical environment models, and future needs," *Advances in Space Research*, Apr. 2024, ISSN: 0273-1177. DOI: 10.1016/j.asr.2024.03.079. [Online]. Available: https://www.sciencedirect.com/science/article/pii/S0273117724003296 (visited on 07/10/2025).

[22] Y. Kimoto, N. Nemoto, H. Matsumoto, K. Ueno, T. Goka, and T. Omodaka, "Space radiation environment and its effects on satellites: Analysis of the first data from TEDA on board ADEOS-II," *IEEE Transactions on Nuclear Science*, vol. 52, no. 5, pp. 1574–1578, Oct. 2005, ISSN: 1558-1578. DOI: 10.1109/TNS.2005.855822. [Online]. Available: https://ieeexplore.ieee.org/document/1546461 (visited on 07/10/2025).

[23] P. Blasi, "The origin of galactic cosmic rays," en, *The Astronomy and Astrophysics Review*, vol. 21, no. 1, p. 70, Nov. 2013, ISSN: 1432-0754. DOI: 10.1007/s00159-013-0070-7. [Online]. Available: https://doi.org/10.1007/s00159-013-0070-7 (visited on 07/10/2025).

[24] R. H. Maurer, M. E. Fraeman, M. N. Martin, and D. R. Roth, "Harsh Environments: Space Radiation Environment, Effects, and Mitigation," en, *Johns Hopkins APL Technical Digest*, vol. 28, no. 1, 2008.

[25] *Radiation Handbook for Electronics*, en-US. [Online]. Available: https://www.ti.com/applications/industrial/aerospace-defense/space/radiation-handbook-for-electronics.html (visited on 06/19/2025).

[26] D. Sinclair and J. Dyer, "Radiation effects and cots parts in smallsats," en, 2013. [Online]. Available: https://digitalcommons.usu.edu/cgi/viewcontent.cgi?article=2934&context=smallsat.

[27] R. F. Hodson, Y. Chen, J. E. Pandolf, *et al.*, "Recommendations on Use of Commercial-Off-The-Shelf (COTS) Electrical, Electronic, and Electromechanical (EEE) Parts for NASA Missions," en, National Aeronautics and Space Administration, Tech. Rep., 2020. [Online]. Available: https://ntrs.nasa.gov/citations/20205011579.

[28] F. Sexton, "Destructive single-event effects in semiconductor devices and ICs," *IEEE Transactions on Nuclear Science*, vol. 50, no. 3, pp. 603–621, Jun. 2003, ISSN: 1558-1578. DOI: 10.1109/TNS.2003.813137. [Online]. Available: https://ieeexplore.ieee.org/document/1208579 (visited on 07/10/2025).

[29] J. R. Schwank, M. R. Shaneyfelt, D. M. Fleetwood, *et al.*, "Radiation Effects in MOS Oxides," *IEEE Transactions on Nuclear Science*, vol. 55, no. 4, pp. 1833–1853, Aug. 2008, ISSN: 1558-1578. DOI: 10.1109/TNS.2008.2001040. [Online]. Available: https://ieeexplore.ieee.org/document/4636929 (visited on 07/10/2025).

[30] P. Dodd and L. Massengill, "Basic mechanisms and modeling of single-event upset in digital microelectronics," *IEEE Transactions on Nuclear Science*, vol. 50, no. 3, pp. 583–602, Jun. 2003, ISSN: 1558-1578. DOI: 10.1109/TNS.2003.813129. [Online]. Available: https://ieeexplore.ieee.org/document/1208578 (visited on 07/10/2025).

[31] Space Exploration Technologies Corp., "Rideshare Payload User's Guide," Space Exploration Technologies Corp., Tech. Rep., Sep. 2024. (visited on 07/11/2025).

[32] F. Louw and N. Roets, "CubeADCS ICD," CubeSpace Satellite Systems (Pty) Ltd, Tech. Rep., 2025. [Online]. Available: https://www.cubespace.co.za/uploads/a9331ba4-34e9-4d93-b486-45bf092d06ca.pdf (visited on 06/10/2025).

[33] Hexagon AB, *OEM719 Electrical and Environmental Specifications*. [Online]. Available: https://docs.novatel.com/OEM7/Content/Technical_Specs_Receiver/OEM719_Electric_Environment_Specs.htm (visited on 06/10/2025).

[34] J. Miller, *CubeWheel ICD*, 2025. [Online]. Available: https://www.cubespace.co.za/uploads/29197e76-cd6d-409e-8896-e29b4813ed2c.pdf (visited on 06/10/2025).

[35] scr00chy, *SpaceX Smallsat Rideshares*, en-GB, Jan. 2020. [Online]. Available: https://www.elonx.net/spacex-smallsat-rideshare-missions/ (visited on 07/07/2025).

[36] Science Applications International Corporation, Inc, *Space-Track.org*. [Online]. Available: https://www.space-track.org/auth/login (visited on 07/07/2025).

[37] J. Wertz and W. J. Larson, *Space Mission Analysis and Design*, en, 3rd ed. Microcosm Press, 1999, ISBN: 1-881883-10-8. [Online]. Available: https://link.springer.com/book/9780792359012 (visited on 07/11/2025).

[38] *2.4v 1300mah Ultra Low Temperature -40 Degree Super Long Cycle Life Lto 18650 Lithium Titanate Battery For Energy Storage*, en. [Online]. Available: https://www.alibaba.com/product-detail/2-4V-1300mAh-ultra-Low-Temperature_1600998043712.html (visited on 07/12/2025).

[39] MicroLink Devices, Inc., *Photovoltaics*, en-US. [Online]. Available: https://mldevices.com/photovoltaics-2/ (visited on 06/22/2025).

[40] NASA, *Long Duration Exposure Facility (LDEF)*. [Online]. Available: https://curator.jsc.nasa.gov/mic/ldef/index.cfm (visited on 06/22/2025).

[41] P. M. Stella, "LEO Effects On Candidate Solar Cell Cover Materials," en, Jet Propulsion Lab, Tech. Rep., 1992. [Online]. Available: https://ntrs.nasa.gov/api/citations/19930020498/downloads/19930020498.pdf (visited on 06/22/2025).

[42] E. Ortiz-Rivera and F. Peng, "Analytical Model for a Photovoltaic Module using the Electrical Characteristics provided by the Manufacturer Data Sheet," in *2005 IEEE 36th Power Electronics Specialists Conference*, ISSN: 2377-6617, Jun. 2005, pp. 2087–2091. DOI: 10.1109/PESC.2005.1581920. [Online]. Available: https://ieeexplore.ieee.org/document/1581920 (visited on 06/22/2025).

[43] M. Chegaar, A. Hamzaoui, A. Namoda, P. Petit, M. Aillerie, and A. Herguth, "Effect of Illumination Intensity on Solar Cells Parameters," *Energy Procedia*, TerraGreen 13 International Conference 2013 - Advancements in Renewable Energy and Clean Environment, vol. 36, pp. 722–729, Jan. 2013, ISSN: 1876-6102. DOI: 10.1016/j.egypro.2013.07.084. [Online]. Available: https://www.sciencedirect.com/science/article/pii/S1876610213011703 (visited on 06/22/2025).

[44] "NCR18650B Standard data," Panasonic, Tech. Rep., Mar. 2012. [Online]. Available: https://cdn.shopify.com/s/files/1/0481/9678/0183/files/panasonic_18650b_data_sheet.pdf.

[45] S. S. Choi and H. S. Lim, "Factors that affect cycle-life and possible degradation mechanisms of a Li-ion cell based on LiCoO2," *Journal of Power Sources*, vol. 111, no. 1, pp. 130–136, Sep. 2002, ISSN: 0378-7753. DOI: 10.1016/S0378-7753(02)00305-1. [Online]. Available: https://www.sciencedirect.com/science/article/pii/S0378775302003051 (visited on 06/23/2025).

[46] M. Rosu-Hamzescu and S. Oprea, "Practical Guide to Implementing Solar Panel MPPT Algorithms," en, Microchip Technology Inc., Tech. Rep., 2013. [Online]. Available: https://ww1.microchip.com/downloads/en/appnotes/00001521a.pdf (visited on 07/11/2025).

[47] G. L. Plett, *Battery Management Systems, Volume II: Equivalent-Circuit Methods*, en-US. Artech, 2015, ISBN: 978-1-63081-023-8. [Online]. Available: https://ieeexplore.ieee.org/document/9100098 (visited on 07/10/2025).

[48] NASA, *Earth Fact Sheet*. [Online]. Available: https://nssdc.gsfc.nasa.gov/planetary/factsheet/earthfact.html (visited on 07/11/2025).

[49] K. Emery and C. Osterwald, "AM0 efficiency measurements," NTRS Author Affiliations: Midwest Research Inst. NTRS Document ID: 19890015365 NTRS Research Center: Legacy CDMS (CDMS), Apr. 1989. [Online]. Available: https://ntrs.nasa.gov/citations/19890015365 (visited on 07/14/2025).

A Physical Constants

Parameter	Value	Notes
μ	$3.986 \times 10^5 \frac{\text{km}^3}{\text{s}^2}$	Earth's Standard Gravitational Parameter [48]
R_E	6378km	Earth's Radius [48]
J_2	1082.63×10^{-6}	Earth's zonal harmonic coefficient [48]
AM0	$1367 \frac{W}{m^2}$	Average Solar Irradiance in Space [49]

Table A.1: Physical Constants

B Interface Control Document

ICD begins on the next page

Power Conditioning and Distribution Module Interface Control Document

For

Electrical Power System

Prepared by Ben Kelman

University of Victoria Centre for Aerospace Research

2025-07-16

Table 1: Document Revision History

Name	Date	Revision Summary	Version
Ben Kellman	2025-03-18	First Draft	1.0
Ben Kellman	2025-07-16	Second Draft	2.0

Table of Contents

Mechanical Interfaces

Connector Positions

Refer to drawing 90017 Rev A for PC104 connector positions. Refer to drawing 90019 for other connectors.

Component Height

Top side: 10 mm maximum.
Bottom side: No components allowed, except battery connector.

Mounting Holes

Refer to drawing 90017 Rev A for mounting hole positions. All mounting holes must be plated, with a hole diameter of 3.3 mm and pad diameter of 6.5 mm. Three mounting holes must be floating, and one mounting hole must be connected to the PCDM ground through a removable jumper.

Thermal Interfaces

The primary thermal interface is between the bottom side of the PCDM and the battery pack, through a non-conductive thermal pad. The mounting holes act as a secondary thermal interface. The PCB layout should minimize the thermal resistance between the thermal interfaces and any components with high power dissipation.

Maximum Power Dissipation

The maximum power dissipated by the PCDM under full load (30 W) is less than 2W.

Electrical Interfaces

PC104 Interface

H2	2	4	6	8	10	12	14	16	18	20	22	24	26	28	30	32	34	36	38	40	42	44	46	48	50	52
	1	3	5	7	9	11	13	15	17	19	21	23	25	27	29	31	33	35	37	39	41	43	45	47	49	51
H1	2	4	6	8	10	12	14	16	18	20	22	24	26	28	30	32	34	36	38	40	42	44	46	48	50	52
	1	3	5	7	9	11	13	15	17	19	21	23	25	27	29	31	33	35	37	39	41	43	45	47	49	51

PC 104 Interface Description					
Connector Type		2x SSQ-126-21-G-D | Samtec			
Header		**Pin(s)**	**Name**	**Description**	**Range (V)**
Telemetry					
	H1	1	CAN_L	Telemetry CAN bus Low	0 to 5
	H1	3	CAN_H	Telemetry CAN bus High	0 to 5
	H1	25	VMON_PACK	Battery pack voltage scaled by 0.28	0 to 3.3
Control					
	H2	31	HEARTBEAT	Spacecraft heartbeat	0 to 3.3
	H2	35	EN_BURN	Enable control for burn wire channel	0 to 3.3
	H2	37	EN_PAY	Enable control for payload channel	0 to 3.3
	H2	39	EN_TTC	Enable control for TT&C channel	0 to 3.3
	H2	41	EN_ADCS	Enable control for ADCS channel	0 to 3.3
	H2	49	EN_GNSS	Enable control for GNSS channel	0 to 3.3
	H2	51	EN_PMU	Enable control for EPS PMU channel	0 to 3.3
Power					
	H1	7,8,9,10	VBAT_PAY	Unregulated payload supply	8 to 11
	H1	5,6,11,12	GND (PAY)	Payload dedicated GND	0
	H1	21,22	5V5_TTC	Regulated TT&C supply	5.4 to 5.6
	H1	19,20	GND (TTC)	TT&C dedicated GND	0
	H1	29,30	3V3_CDH	Regulated OBC supply	3.2 to 3.35
	H1	27,28	GND (CDH)	OBC dedicated GND	0
	H1	33,34	3V3_GNSS	Regulated OEM719 supply	3.2 to 3.35
	H1	31,32	GND (GNSS)	OEM719 dedicated GND	0

	H2	1,2	5V_BURN	Burn wire supply	5 to 5.15
	H2	3,4	GND (BURN)	Burn wire dedicated GND	0
	H2	25,26	5V_ADCS	ADCS 5V supply	5 to 5.15
	H2	27,28	3V3_ADCS	ADCS 3.3V supply	3.2 to 3.35
	H2	45,46	VBAT_ADCS	ADCS battery supply	8 to 11
	H2	29,30,32	GND (ADCS)	ADCS GND	0
	H2	23,24,33, 34,43,44, 47,48	GND (Extra)	Extra GND connections not dedicated to any subsystems. Most subsystems use all available GND pins.	0

Battery Interface

Battery Connector Interface Description				
Connector Type	SSQ-107-01-G-S			
Mating Connector	TSM-107-01-x-SH-A (x = S or L)			
Pin(s)	**Name**	**Description**	**Range (V)**	**Current (A)**
1,2,3	GND	Battery pack ground connection	0	3
5,6	VBAT	Battery pack positive voltage connection	8 to 11	3
4	TMON_SDQ	One wire temperature sensor interface	0 to 3.3	<10mA

Harnesses

Solar Array Harness

Solar Array Harness Interface Description	
Connector Type	PCB Headers and Receptacles Part 5055670981 | Molex

Mating Housing		Connector Housings Part 5055650901 | Molex		
Mating Terminals		Crimp Terminals Part 5054311300 | Molex		
Pin(s)	**Name**	**Description**	**Range (V)**	**Current (A)**
2,3,4,5	GND	Solar array ground connection	0	4
6,7,8,9	VARR	Solar array positive voltage connection	0 to 12	4
1	TMON_SDQ	One wire temperature sensor interface	0 to 3.3	<10mA

Deployment Switch Harnesses

The PCDM features two deployment switch connectors with identical interfaces as shown below.

Deployment Switch Harness Interface Description			
Connector Type		PCB Headers and Receptacles Part 5055670281 | Molex	
Mating Housing		Connector Housings Part 5055650201 | Molex	
Mating Terminals		Crimp Terminals Part 5054311300 | Molex	
Pin(s)	**Name**	**Description**	**Range (V)**
1	DSW_A_COM	Deployment switch common connection	0 to 11
2	DSW_A_NO	Deployment switch normally open connection	0 to 11

EGSE Harness

Deployment Switch Harness Interface Description			
Connector Type		PCB Headers and Receptacles Part 5055670881 | Molex	
Mating Housing		Connector Housings Part 5055650801 | Molex	
Mating Terminals		Crimp Terminals Part 5054311300 | Molex	
Pin(s)	**Name**	**Description**	**Range (V)**
1	PMU_SWDIO	The DIO pin for the telemetry MCU's serial wire	0 to 3.3

		debug programming interface	
2	PMU_RST	The reset pin for the telemetry MCU's serial wire debug programming interface	0 to 3.3
3	PMU_SWCLK	The clock pin for the telemetry MCU's serial wire debug programming interface	0 to 3.3
4	RBF	The RBF pin connector. Forces the spacecraft into the stowed state when pulled to GND & forces the spacecraft into the deployed state when pulled to 3V3.	0 to 3.3
5	OFF_HEART	Disables heartbeat resets when pulled to 3V3.	0 to 3.3
6	OFF_DEPLOY	Dispables the burnwire channel when pulled to GND	0 to 3.3
7	VADAPT	EGSE charging power supply input.	10 to 20
8	GND	Ground	0

Power Interfaces

Solar Array Interface

ALL VARR and GND connections are internally connected, blocking diodes must be added in series with each string of cells to the PCDM. The PCDM implements an input voltage regulation scheme that will ensure the voltage across the solar array does not drop below 9.3 V by default. If software MPPT is enabled, the solar array voltage minimum solar array voltage will be adjusted to between 7 and 12 V to maximize power generation.

The TMON_SDQ connection provides a one wire interface to communicate with up to 13 TMP1826 temperature sensors in a bus powered configuration. The TMP1826 address must be set to addresses between 0x03 and 0x0F using a resistor on the ADDR pin as described in section 8.3.8.3 of the datasheet. Addresses 0x02, 0x01 and 0x00 are reserved for internal use on the PCDM and battery pack.

Battery

The battery will be charged in a CC/CV scheme with the charge current limited to 2.5 A and the charge voltage regulated to 10.8 V. During discharge, up to 4 A may be drawn from the battery. When the battery drops below 6 V, the current draw from the battery will be reduced to below 10 mA to prevent over-discharging the battery pack.

The TMON_SDQ connection must be connected to a single TMP1826 temperature sensor in a bus powered configuration. The address of the TMP1826 must be set to 0x02 using the method described in section 8.3.8.3 of the datasheet.

Subsystem Channels

The supply voltage characteristics of each regulated and unregulated channel is given below. Voltage values are as measured at the PC104 connector.

Channel Name	Nominal Voltage	Minimum Voltage	Maximum Voltage	Ripple	OV Protection	Current Limit
5V5_TTC	5.5 V	5.4 V	5.6 V	< 50 mV	< 6 V	> 2 A
3V3_CDH	3.3 V	3.2 V	3.35 V	< 50 mV	< 3.4 V	> 0.5 A
3V3_GNSS	3.3 V	3.2 V	3.35 V	< 50 mV	< 3.4 V	> 3 A
3V3_ADCS	3.3 V	3.2 V	3.35 V	< 50 mV	< 3.4 V	> 2 A
5V_BURN	5.1 V	4.9 V	5.15 V	< 50 mV	N/A	> 3 A
5V_ADCS	5.1 V	5.0 V	5.15 V	< 50 mV	< 5.2 V	> 2 A
VBAT_ADCS	10 V	8 V	11 V	< 100 mV	< 12 V	> 2 A
VBAT_PAY	10 V	8 V	11 V	< 100 mV	< 12 V	> 3 A

Fault Handling

Each channel on the EPS implements 3 types of protection:

- Overcurrent
- Short Circuit
- Overvoltage

If a fault causes a channel to become disabled, it will remain disabled until the EN_<SUBSY> signal is deasserted and then reasserted.

Overcurrent

If a subsystem attempts to draw more current than the current limit described above, the voltage of the channel will be lowered to actively limit the current limit. If the overcurrent condition persists, the channel will be disabled. This cutoff is caused by an over-temperature condition within the e-fuse, see the figure below for a rough estimate of the maximum time until thermal

shutdown. The overcurrent limits are set well above the maximum current draw for subsystems and are primarily intended to protect the EPS during A&IT and prevent spacecraft wide brownouts in the case of an overcurrent event. **The overcurrent limit is unlikely to provide any meaningful protection for subsystems in the case of high current events (ex. latch-ups).**

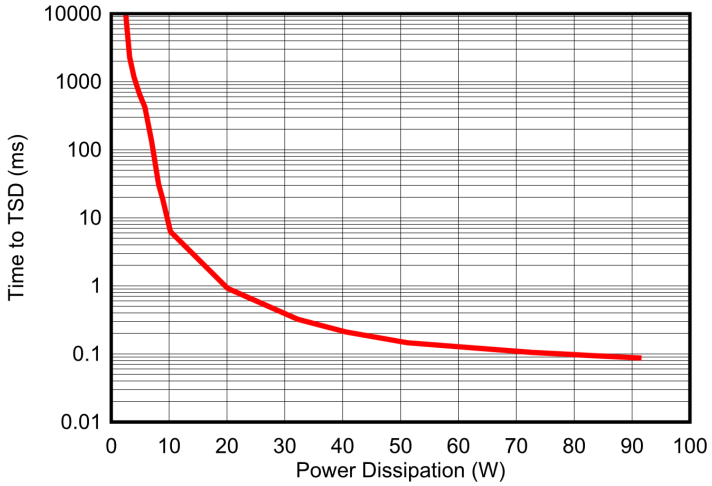

Thermal Shutdown Characteristics

Short Circuit
If a subsystem attempts to draw current well over the overcurrent limit, the channel will be disabled immediately (~10 us) and active current limiting will not occur.

Overvoltage
This protects subsystems from overvoltage transients or faults from within the EPS. Voltages will be clamped below the overvoltage limits shown above within 2 us of the event. If the overvoltage event persists the channel will be disabled.

Turn On Characteristics

The slew rate of the voltage is limited to 2V /ms to limit inrush current during turn on. Maximum capacitance should be limited to under 250 uF to limit maximum inrush current to 500 mA.

Turn Off Characteristics

When a channel is turned off the output of the channel will be tied to ground with a 100 Ohm impedance. This ensures the supply voltage quickly drops to 0 after the channel is turned off.

Communications & Control Interface

Control

Subsystem Channels

When the EN_<SUBSYS> control signal is raised above V_{IH} the channel will be enabled as described in Turn On Characteristics, when the control signal voltage is dropped below V_{IL} the channel will be disabled as described in Turn Off Characteristics. The channel state is undefined for voltage levels between V_{IL} and V_{IH}.

Note that EN_PMU controls the internal EPS power measurement unit and not a channel on the PC104 header.

Channel Enable Logic Levels	
V_{IL}	0.5 V
V_{IH}	2 V

Deployment Channel

The burn wire channel (E_BURN) behaves similarly to the channels described above; however, this channel can be disabled by tying the OFF_DEPLOY EGSE signal to GND. To detect if deployment has been disabled via EGSE, the BURN_DIS backplane signal indicates the true state of the burn wire channel. This is summarized in the truth table below (Note: Z indicates a High impedance state).

EN_BURN	OFF_DEPLOY	Burnwire Channel
H	Hi-Z	ON
L	Hi-Z	OFF
H	L	OFF
L	L	OFF

`

Heartbeat

A falling edge transition must occur on the HEARTBEAT control signal at least every 2s to reset the heartbeat watchdog timer. If the heartbeat timer expires, the voltage supplied to each subsystem will drop below 10 mV for at least 4 seconds. The timer will not start for 10s after startup or a reset event, giving a grace period for the OBC subsystem to boot and begin “petting” the heartbeat watchdog timer.

This signal serves several purpose:

- It allows for faults on the CDH channel to be recovered from
- It allows the OBC a method to power cycle the whole spacecraft

CAN Bus Interface

All telemetry will be available to the spacecraft via the CAN bus interface on the PC104 connector when EN_PMU is pulled high. Telemetry generation is disabled when EN_PMU is pulled low and the telemetry MCU along with all associated sensors will be fully powered off.

CAN Bus Parameters	
Bit Rate	1 Mbps
Supported CSP Packets	UDP Only
CSP Node ID	1

Telemetry Items

This section lists all telemetry items generated by the EPS.

Distributed Channels		
Telemetry Item	**Description**	**Data Type**
IMON_3V3_CDH_MAX	Maximum current seen on the 3.3V CDH channel	int16
IMON_3V3_CDH_AVG	Mean current seen on the 3.3V CDH channel	int16
IMON_5V5_TTC_MAX	Maximum current seen on the 5.5V TTC channel	int16

IMON_5V5_TTC_AVG	Mean current seen on the 5.5V TTC channel	int16
IMON_3V3_GNSS_MAX	Maximum current seen on the 3.3V GNSS channel	int16
IMON_3V3_GNSS_AVG	Mean current seen on the 3.3V GNSS channel	int16
IMON_3V3_ADCS_MAX	Maximum current seen on the 3.3V ADCS channel	int16
IMON_3V3_ADCS_AVG	Mean current seen on the 3.3V ADCS channel	int16
IMON_5V_ADCS_MAX	Maximum current seen on the 5V ADCS channel	int16
IMON_5V_ADCS_AVG	Mean current seen on the 5V ADCS channel	int16
IMON_VBAT_ADCS_MAX	Maximum current seen on the battery voltage ADCS channel	int16
IMON_VBAT_ADCS_AVG	Mean current seen on the battery voltage ADCS channel	int16
IMON_VBAT_PAY_MAX	Maximum current seen on the battery voltage Payload channel	int16
IMON_VBAT_PAY_AVG	Mean current seen on the battery voltage Payload channel	int16
IMON_3V3_PMU_MAX	Maximum current seen on the 3.3V PMU channel	int16
IMON_3V3_PMU_AVG	Mean current seen on the 3.3V PMU channel	int16

Solar Array		
Telemetry Item	**Description**	**Data Type**
Maximum Voltage	The maximum measured solar array voltage	int16
Minimum Voltage	The minimum measured solar array voltage	int16
Average Sunlight Voltage	The average solar array voltage while the spacecraft is in sunlight.	int16
Average Voltage	The average solar array voltage.	int16

Average Current	The average current out of the solar array.	int16
Maximum Current	The maximum current out of the solar array.	int16
Average Power	The average power generated by the solar array.	int16
Maximum Power	The maximum power generated by the solar array.	int16
Eclipse Time	The time that the spacecraft was in eclipse.	uint16
Sunlight Time	The time that the spacecraft was in sunlight.	uint16
Maximum MPP	The maximum measured maximum power point voltage of the solar array	int16
Minimum MPP	The minimum measured maximum power point voltage of the solar array	int16
MPP Time	The amount of time that the solar array was generating its full output power (i.e. how long the solar array voltage was tracked to the MMP).	uint16

Solar Array		
Telemetry Item	**Description**	**Data Type**
Minimum Voltage	The minimum battery pack voltage	int16_t
Maximum Voltage	The maximum battery pack voltage	int16_t
Average Voltage	The average battery pack voltage	int16_t
Minimum Current	The minimum battery pack current (maximum charge current)	int16_t
Maximum Current	The maximum battery pack current (maximum discharge current)	int16_t
Average Current	The average current into/out of the battery pack.	int16_t
Average Power	The average power into/out of the spacecraft should be ~0 for a healthy spacecraft.	int16_t
Average Charge Current	The average current into the battery pack while it is charging/charged.	int16_t
Average charge power	The average power into the battery pack while it is charging/charged.	int16_t
Average Discharge Current	The average current out of the battery pack while it is discharging.	int16_t

Average discharge power	The average power out of the battery pack while it is discharging.	int16_t
Charged Time	The time that the battery charged for	uint16_t
Discharging Time	The time that the battery discharged for	uint16_t
Charging Time	The time that the battery charging for	uint16_t

Temperature		
Telemetry Item	**Description**	**Data Type**
TMON_X_FIX	Temperature of the +X fixed panel (Fix)	uint8_t
TMON_NEGX_FIX	Temperature of the -X fixed panel (Fix)	uint8_t
TMON_Y_FIX	Temperature of the +Y fixed panel (Fix)	uint8_t
TMON_NEGY_FIX	Temperature of the -Y fixed panel (Fix)	uint8_t
TMON_Z_FIX	Temperature of the +Z fixed panel (Fix)	uint8_t
TMON_NEGZ_FIX	Temperature of the -Z fixed panel (Fix)	uint8_t
TMON_X_DEP	Temperature of the +X deployable panel (Dep)	uint8_t
TMON_NEGX_DEP	Temperature of the -X deployable panel (Dep)	uint8_t
TMON_Y_DEP	Temperature of the +Y deployable panel (Dep)	uint8_t
TMON_NEGY_DEP	Temperature of the -Y deployable panel (Dep)	uint8_t
TMON_PACK	Temperature of the battery pack (Pack)	uint8_t
TMON_PCDM	Temperature of the power control and distribution module (PCDM)	uint8_t

Deployment

Stowed State

When any of the deployment switches is depressed (open) the voltage supplied to all subsystems will be < 10 mV and the current into or out of the battery pack will be less than 100 uA.

Deployed State

When all of the deployment switches are not depressed (closed) the 3V3_CDH channel will be enabled if the battery voltage is greater than 8 V, from this point on the OBC controls the power state of all channels. If the battery voltage drops below 6 V, 3V3_CDH will be disabled until the battery voltage rises above 8 V.

RBF

The RBF mechanism must pull the ON_EPS EGSE signal to GND, this has the effect of forcing the spacecraft into the stowed state.

EGSE Interface

Programming

The EGSE connector exposes the SWD interface for the SAMC21 telemetry MCU. This is a 3.3V interface, it is recommended to reprogram the MCU using a SEGGER J-Link EDU Mini debug probe.

Heartbeat

Pulling the OFF_HEART signal high will prevent the EPS from resetting if the heartbeat timer expires. This is required for standalone EPS testing.

Deployment

Pulling the OFF_DEPLOY to GND will disable the burn wire channel, this allows for the assembled spacecraft to be powered on without attempting to deploy the antenna. See Deployment Channel for more details. **Note OFF_DEPLOY will enable the burn wire channel if it is pulled high.**

Charging

The VADPT connection allows for ground based charging of the spacecraft. This should be connected to a lab power supply with a voltage set to between 10 and 20 V, with a 1A current limit. Voltages down to 7 V may be used if the software based MPPT is enabled.

Telemetry

All generated telemetry is available via the spacecraft system CAN bus. This is accessible via the OBC's EGSE harness on the assembled spacecraft or via the PC104 connector on a standalone EPS.

End of Document

NOTES:

1. DIMENSIONS ARE IN MILLIMETERS.
2. NOMINAL PCB THICKNESS: 1.6 mm.
3. THIS DRAWING ONLY SPECIFIES PC104 CONNECTOR AND MOUNTING HOLE LOCATIONS. REFER TO SUBSYSTEM DRAWING FOR FURTHER DETAILS.

REVISION HISTORY				
ZONE	REV	DESCRIPTION	DATE	APPROVED
	A	INITIAL RELEASE	2024-08-01	TT

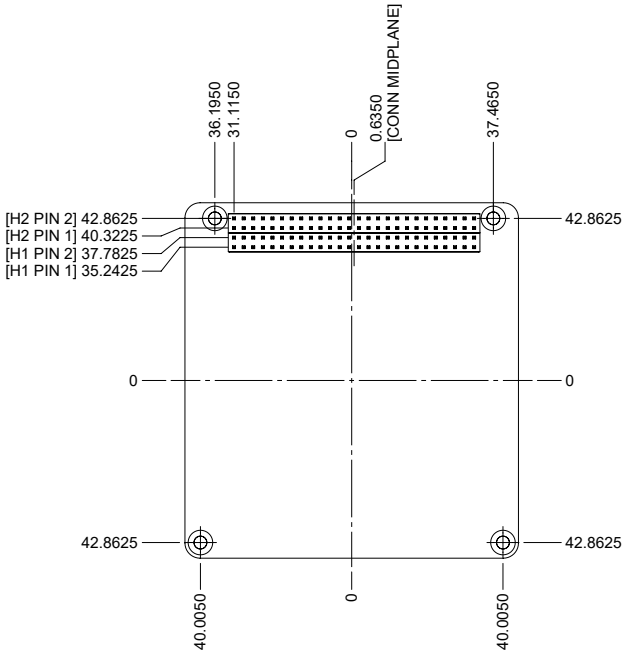

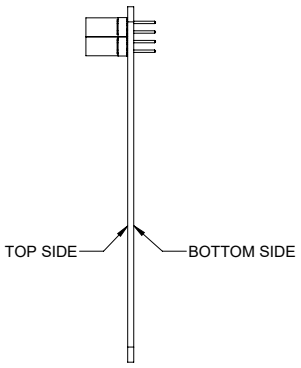

APPROVALS	DATE
DRAWN T TARNOWSKI	2024-08-01
CHECKED	
DESIGN	
ANALYSIS	

☐ FLIGHT
☐ NON-FLIGHT

THIRD ANGLE PROJECTION

University of Victoria | Centre for Aerospace Research
ENGINEERING OFFICE WING 148
3800 FINNERTY ROAD
VICTORIA BC, CANADA V8P 5C2

TITLE: PC104 TEMPLATE

SIZE	CAGE CODE	DWG NO	REV
B	L4320	90017	A

SCALE	1:1	WEIGHT	g	SHEET	1 OF 1

NOTES:

1. REFER TO DWG 90017 (LATEST REV) FOR PC104 CONNECTOR AND MOUNTING HOLE LOCATIONS.
2. BOARD OUTLINE CONTROLLED BY 3D MODEL. REFER TO MODEL FOR DIMENSIONS.
3. ALL COMPONENTS MUST REMAIN ENTIRELY INSIDE BOARD OUTLINE.
4. COMPONENT PART NUMBERS ARE FOR REFERENCE ONLY. IN CASE OF DISCREPANCY BETWEEN THIS DRAWING AND THE INTERFACE CONTROL DOCUMENT (ICD), ICD TAKES PRECEDENCE.

REVISION HISTORY				
ZONE	REV	DESCRIPTION	DATE	APPROVED
	A	INITIAL RELEASE	2024-09-12	TT
	B	MOVE CONNECTORS TO PMM	2024-11-01	TT
	C	UPDATE FOR REV 2	2025-04-02	TT

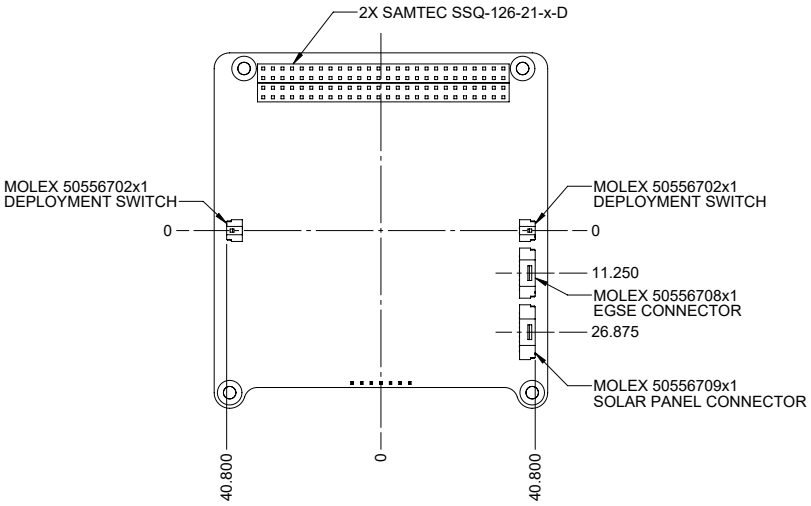

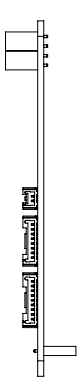

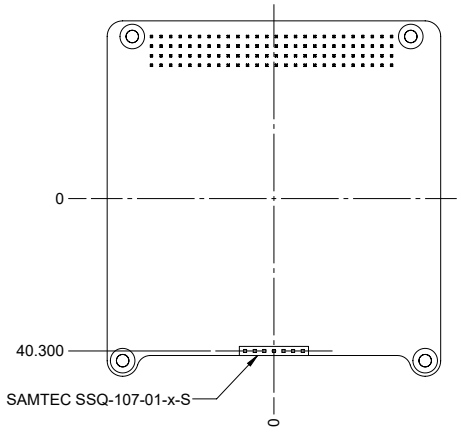

APPROVALS	DATE
DRAWN T TARNOWSKI	2024-09-12
CHECKED	
DESIGN	
ANALYSIS	

☐ FLIGHT
☐ NON-FLIGHT

THIRD ANGLE PROJECTION

University of Victoria | Centre for Aerospace Research
ENGINEERING OFFICE WING 148
3800 FINNERTY ROAD
VICTORIA BC, CANADA V8P 5C2

TITLE: PCDM MECHANICAL LAYOUT

SIZE	CAGE CODE	DWG NO	REV
B	L4320	90019	C

SCALE	1:1	WEIGHT	g	SHEET	1 OF 1